

2018-03-19

Tightly Coupled Integration of GNSS/INS/Stereo Vision/Map Matching System for Land Vehicle Navigation

Liu, Fei

Fei, L. (2018). Tightly Coupled Integration of GNSS/INS/Stereo Vision/Map Matching System for Land Vehicle Navigation (Doctoral thesis, University of Calgary, Calgary, Canada). Retrieved from <https://prism.ucalgary.ca>. doi:10.11575/PRISM/31740

<http://hdl.handle.net/1880/106447>

Downloaded from PRISM Repository, University of Calgary

UNIVERSITY OF CALGARY

Tightly Coupled Integration of GNSS/INS/Stereo Vision/Map Matching System for Land
Vehicle Navigation

by

Fei Liu

A THESIS

SUBMITTED TO THE FACULTY OF GRADUATE STUDIES
IN PARTIAL FULFILMENT OF THE REQUIREMENTS FOR THE
DEGREE OF DOCTOR OF PHILOSOPHY

GRADUATE PROGRAM IN GEOMATICS ENGINEERING

CALGARY, ALBERTA

MARCH, 2018

© Fei Liu 2018

Abstract

This thesis proposes a tight integration architecture with an Inertial Measurement Unit (IMU) as the core sensor for land vehicle navigation. Kalman filter is used to fuse different types of measurements. The IMU provides the dynamic information of the land vehicle and it is used to predict the measurements of other sensors. When the measurements become available, the differences between the predicted and actual measurements are applied to estimate the error states in the Kalman filter. There are four types of integration implemented in this thesis. First, the IMU is integrated with the Stereo Visual Odometry (VO). In this tight integration, the camera attitude and perspective center position can be predicted by the IMU mechanization and the 3-dimensional (3D) coordinates of the features can be obtained by the triangulation of the stereo images at the previous epoch. Therefore, the pixel coordinates of the features can be predicted based on the feature position, perspective center position and camera attitude. The difference between the predicted and actual pixel coordinates can be used to estimate the errors. In this way, the accumulated errors of inertial sensors can be largely reduced by the tightly coupled integration. The integration can reduce the accumulated errors of an individual system. Second, the integration system can be easily expanded with GNSS measurements when GNSS measurements are available. The state vector in the Kalman filter needs to be extended with the receiver clock error and the clock drift to adopt the GNSS code, carrier-phase and Doppler measurements. In this thesis, Precise Point Positioning (PPP) using one receiver is integrated with the Inertial Navigation System (INS) and Stereo VO. Third, fuzzy logic Map Matching (MM) is introduced to be integrated into the system. When there is GNSS outage, the INS/ Stereo VO solution can be projected on the digital map by fuzzy logic MM. The projected point provides the position information for the system, which effectively limits the drift of DR systems. Fourth, when the land

vehicle is moving in open sky environment, PPP dominates the system accuracy. A fast PPP ambiguity resolution (AR) method is proposed to fix the ambiguities in the kinematic mode with the aid of MM. Generally, the float PPP solution is projected on the digital map. The projected point and the road link azimuth is applied as additional measurements to accelerate the convergence of ambiguities which reduces the integer search space, resulting in fast ambiguity resolution. Filed test datasets collected by Karlsruhe Institute of Technology and Toyota Technological Institute (KITTI) and datasets collected in Calgary are used to verify the effectiveness of the proposed methods.

Preface

This thesis includes some materials (e.g. figures, tables, formulas) from four journal papers and three conference papers as follows:

1. Liu, Fei, and Yang Gao. "Triple-Frequency GPS Precise Point Positioning Ambiguity Resolution Using Dual-Frequency Based IGS Precise Clock Products." *International Journal of Aerospace Engineering* 2017 (2017).
2. Balazadegan Sarvrood, Yashar, Fei Liu, and Yang Gao. "Tight integration of kinematic precise point positioning and digital map for land vehicle localisation." *Survey Review* (2017): 1-9.
3. Liu, Fei, Yashar Balazadegan Sarvrood, and Yang Gao. "Tight Integration of INS/Stereo VO/Digital Map for Land Vehicle Navigation." *Photogrammetric Engineering & Remote Sensing* 84, no. 1 (2018): 15-23.
4. Liu, Fei, Yashar Balazadegan Sarvrood, and Yang Gao. "Implementation and Analysis of Tightly Integrated INS/Stereo VO for Land Vehicle Navigation." *The Journal of Navigation* 71, no. 1 (2018): 83-99.
5. Liu, Fei, "Kinematic PPP Ambiguity Resolution with Aid of Map Matching," *Proceedings of the 30th International Technical Meeting of The Satellite Division of the Institute of Navigation (ION GNSS+ 2017)*, Portland, Oregon, September 2017, pp. 4176-4183.
6. Liu, Fei, Yang, Hongzhou, Gao, Yang, "Tightly Coupled Kinematics Visual Odometry/PPP System for Land Vehicle Navigation," *Proceedings of the 29th International Technical Meeting of The Satellite Division of the Institute of Navigation (ION GNSS+ 2016)*, Portland, Oregon, September 2016, pp. 1330-1337.
7. Liu, Fei, Sarvrood, Yashar Balazadegan, Gao, Yang, "Tightly Coupled Stereo Vision Aided Inertial Navigation Using Continuously Tracked Features for Land Vehicles," *Proceedings of the*

28th International Technical Meeting of The Satellite Division of the Institute of Navigation (ION GNSS+ 2015), Tampa, Florida, September 2015, pp. 2127-2133.

Acknowledgements

I would like to express my deepest appreciation to my supervisor, Dr. Yang Gao, who has been providing his continuous support, valuable guidance during my study at the University of Calgary.

I am grateful for his advice on my research.

I would like to thank my committee members: Dr. Naser El-Sheimy and Dr. Ruisheng Wang from the Department of Geomatics Engineering, University of Calgary, Dr. Yufen (Frank) Cheng from the Department of Mechanical Engineering, University of Calgary and Dr. Jianguo Wang from York University. Also, Dr. Kyle O’Keeffe is acknowledged for his service during my defense exam.

The financial supports from Chinese Scholarship Council (CSC), University of Calgary and Alberta Innovates Technology Futures (AITF) are acknowledged. I acknowledge the public multi-sensor data provided by Karlsruhe Institute of Technology and Toyota Technological Institute (KITTI) on their website.

I would also like to thank my colleagues at University of Calgary for their support on my research and living these years. Special thanks to my fiancée Yue Liu for her great favor when I collected the filed test data for this thesis.

Finally, I want to thank my parents Zhibo Liu, Yongmei Zhang and families who have been always encouraging me to pursue the career I want and overcome the difficulties. Without their support, I cannot focus on the research these years.

Dedication

*To my parents
Zhibo Liu and Yongmei Zhang*

Table of Contents

Abstract	ii
Table of Contents	viii
List of Figures and Illustrations	xii
 CHAPTER ONE: INTRODUCTION	 1
1.1 Preamble	1
1.2 Background	7
1.2.1 Global Navigation Satellite System	7
1.2.2 Inertial Navigation System (INS) and Low-Cost MEMS IMU	11
1.2.3 Visual Odometry (VO) and Industrial Camera	13
1.3 Literature Review and Limitations	14
1.4 Research Objectives and Contributions	18
1.5 Thesis Outline	20
 CHAPTER TWO: FUNDAMENTALS OF NAVIGATION SYSTEMS USING GNSS PPP, INS AND STEREO VO	 21
2.1 Precise Point Positioning	21
2.1.1 GNSS Error Sources and Mitigation	21
2.1.1.1 Satellite orbit and clock	22
2.1.1.2 Relativistic Effect	23
2.1.1.3 Antenna Phase Center Offset and Variation	24
2.1.1.4 Phase Wind-up Effect	25
2.1.1.5 Troposphere Delay	26
2.1.1.6 Ionosphere Delay	27
2.1.1.7 Sagnac Effect	28
2.1.1.8 Site Displacements	29
2.1.1.9 Summary of Error Sources	30
2.1.2 PPP Float Solution	31
2.1.3 PPP Fixed Solution	33
2.2 Inertial Navigation System	36
2.2.1 Coordinate Frames and Transformation	37
2.2.2 INS Mechanization	39
2.2.3 INS Error Formulation	42
2.3 Stereo Visual Odometry	43
2.3.1 Coordinate Frames and Camera Modeling	44
2.3.2 Stereo VO Steps	46
2.3.2.1 Feature Detection and Tracking (Matching)	46
2.3.2.2 Motion Estimation	48
2.3.2.3 Local Optimization	53
 CHAPTER THREE: DEVELOPMENT OF A TIGHT INTEGRATION SYSTEM FOR LAND VEHICLE NAVIGATION USING IMU, STEREO VO AND GNSS PPP	 56
3.1 Multi-sensor Integration with IMU as the Core Sensor	56
3.1.1 Loose Integration	57

3.1.2 Tight Integration	59
3.2 Tight Integration of INS and Stereo VO	62
3.3 Tight Integration of GNSS PPP, INS and Stereo VO	69
3.4 Summary	73
CHAPTER FOUR: DEVELOPMENT OF MAP MATCHING AND INTEGRATED	
SYSTEM FOR LAND VEHICLE NAVIGATION	75
4.1 Fuzzy Logic Map Matching.....	75
4.1.1 Overview of Fuzzy Logic Theory	76
4.1.2 Fuzzy Logic Map Matching Procedures.....	81
4.1.2.1 Initial Map Matching Process.	82
4.1.2.2 Subsequent Map Matching Process	84
4.2 Tight Integration of INS, Stereo VO and Digital Map	89
4.3 Tight Integration of GNSS PPP and Map Matching.....	92
4.4 Summary	96
CHAPTER FIVE: RESULTS AND ANALYSIS.....	
5.1 Results and Analysis of KITTI Datasets.....	97
5.1.1 Data Description	97
5.1.2 Tight Integration of INS and Stereo VO	100
5.1.3 Tight Integration of INS, Stereo VO and Map Matching.....	114
5.2 Results and Analysis of Calgary Datasets	120
5.2.1 Test Preparation.....	122
5.2.1.1 System Synchronization	123
5.2.1.2 Camera Settings	127
5.2.1.3 Calibration and Rectification	128
5.2.2 Tight Integration of INS and Stereo VO	133
5.2.3 Tight Integration of INS, Stereo VO and Map Matching.....	145
5.2.4 Tight Integration of GPS, INS and Stereo VO	149
5.2.5 Kinematic PPP AR with the Aid of Map Matching	153
5.3 Summary	160
CHAPTER SIX: CONCLUSIONS AND FUTURE WORKS	
6.1 Conclusions.....	162
6.2 Future Work.....	164
REFERENCES	166
APPENDIX A.....	177

List of Tables

Table 1.1 GPS signals	8
Table 1.2 GLONASS Signals	9
Table 1.3 BDS Signals	10
Table 1.4 Different Grade IMUs.....	13
Table 2.1 Satellite Orbit and Clock Errors.....	22
Table 2.2 Summary of GNSS Errors	31
Table 2.3 Warp Functions between Consecutive Images	47
Table 5.1 Specifications of FL2-14S3M-C.....	99
Table 5.2 Position Error RMS in East, North and Height	103
Table 5.3 Position Error RMS in East, North and Height	109
Table 5.4 Position Error RMS in East, North and Height	113
Table 5.5 Relative Horizontal Position Errors of Each Method	114
Table 5.6 Positioning Error RMS for the First Dataset	116
Table 5.7 Positioning Error RMS for the Second Dataset	118
Table 5.8 Positioning Error RMS for the Thrid Dataset.....	120
Table 5.9 Relative Horizontal Positioning Errors of Different Methods.....	120
Table 5.10 PointGrey CM3-U3-13Y3M-CS Specifications	121
Table 5.11 Camera Settings for Field Tests.....	128
Table 5.12 RMS of Position Errors in East, North and Height.....	138
Table 5.13 RMS of Position Errors in East, North and Height.....	140
Table 5.14 RMS of Position Errors in East, North and Height.....	144
Table 5.15 Relative Horizontal Position Errors of Each Method	144
Table 5.16 Position RMS of Different Methods for the First Dataset	146
Table 5.17 Position RMS of Different Methods for the Second Dataset.....	147

Table 5.18 Relative Horizontal Position Errors of Each Method	148
Table 5.19 Positioning Errors with Different Sensors	151
Table 5.20 Position Error RMS in Each Direction	158

List of Figures and Illustrations

Figure 1.1.1 An illustration of terminologies used in INS and their interrelationship	12
Figure 1.2 Sensor Format, Focal Length and Field of View	14
Figure 2.1 Coordinate Systems	38
Figure 2.2 INS Mechanization	40
Figure 2.3 Camera Pin-hole Model	43
Figure 2.4 Projection of Stereo Cameras	45
Figure 2.5 Image Sequence	54
Figure 3.1 Scheme of Closed-Loop Loose Integration	58
Figure 3.2 Scheme of Closed-Loop Tight Integration	59
Figure 3.3 INS/Stereo VO Tight Integration Implementation Architecture	64
Figure 3.4 Feature Coordinates in the Current Camera Frame	67
Figure 3.5 Implementation Procedures	70
Figure 4.1 Membership Function Example	77
Figure 4.2 Membership Functions for HE	80
Figure 4.3 Membership Functions for PD	80
Figure 4.4 Membership Functions for Velocity	83
Figure 4.5 Membership Functions for HDOP	83
Figure 4.6 Parameters for Fuzzy Logic Map Matching	84
Figure 4.7 Membership Functions for α	86
Figure 4.8 Membership Functions for $\Delta\theta$	86
Figure 4.9 Membership Functions for Δd	87
Figure 4.10 Membership Functions for HI	87
Figure 4.11 Membership Functions for HI at U-Turns	88
Figure 4.12 Membership Functions for Distance Error	89

Figure 4.13 Tightly Coupled Integration of Digital Map and INS/Stereo VO.	90
Figure 4.14 Implementation Procedure of PPP AR with the Aid of Map Matching	95
Figure 5.1 KITTI Equipment Installation	98
Figure 5.2 Installation Details of Each Sensor.....	99
Figure 5.3 Test Environment of the First Dataset.....	101
Figure 5.4 Trajectories of the First Test.....	101
Figure 5.5 Position Error in East, North and Height.....	103
Figure 5.6 Forward Velocity Error	104
Figure 5.7 Azimuth Error.....	104
Figure 5.8 Test Environment of the Second Dataset	106
Figure 5.9 Trajectories of the Second Test	107
Figure 5.10 Position Error in East, North and Height.....	108
Figure 5.11 Forward Velocity Error	109
Figure 5.12 Azimuth Error.....	110
Figure 5.13 Test Environment of the Third Dataset	111
Figure 5.14 Trajectories of the Third Test	111
Figure 5.15 Position Error in East, North and Height.....	113
Figure 5.16 Trajectories of the First Dataset for Map Matching	116
Figure 5.17 Trajectories of the Second Dataset for Map Matching.....	118
Figure 5.18 Trajectories of the Third Dataset for Map Matching.....	119
Figure 5.19 Sensors in the Field Tests	121
Figure 5.20 Installation of Sensors	122
Figure 5.21 PointGrey Camera Trigger Mode.....	124
Figure 5.22 GPIO Port on PointGrey CM3-U3-13Y3M-CS	125
Figure 5.23 Functions of the 9-pin GPIO Port on PointGrey CM3-U3-13Y3M-CS.....	126

Figure 5.24 Field Test Setup	127
Figure 5.25 Radial Distortion	129
Figure 5.26 Tangential Distortion	130
Figure 5.27 Chessboard for Camera Calibration	131
Figure 5.28 Images for Camera Calibration	132
Figure 5.29 Stereo Images After Rectification	133
Figure 5.30 First Test Environment	134
Figure 5.31 Trajectory of the First Test	135
Figure 5.32 Position Errors in East, North and Height	138
Figure 5.33 Trajectory of the Second Test.....	139
Figure 5.34 Third Test Environment	140
Figure 5.35 Trajectory of the Third Test	141
Figure 5.36 Position Errors in East, North and Height	143
Figure 5.37 Test Trajectories for the First Dataset	146
Figure 5.38 Test Trajectories for the Second Dataset.....	148
Figure 5.39 Test Environment	150
Figure 5.40 The First Test Trajectory	151
Figure 5.41 Positioning Results in Each Direction.....	153
Figure 5.42 Test Environment	154
Figure 5.43 Test trajectory	155
Figure 5.44 Satellite Sky Plot	156
Figure 5.45 Positioning Errors of Each Method	158
Figure 5.46 Single Difference IF Ambiguities	159
Figure 5.47 Single Difference NL Ambiguities.....	160

List of Abbreviations

Abbreviation	Definition
3D	Three-Dimensional
AR	Ambiguity Resolution
ARP	Antenna Reference Point Visual Odometry
BDS	BeiDou satellite navigation system
CDMA	Code Division Multiple Access
CM	Center of Mass
CNES	Center National d'Etudes Spatiales
DCM	Direction Cosine Matrices
DOP	Dilution of precision
ECI	Earth-Centered Inertial
ENU	East, North and Up
ECEF	Earth Center Earth Fixed
FOC	Full Operational Capability
FPS	Frames Per Second
FDMA	Frequency Division Multiple Access
FCB	Fractional Cycle Bias
FIS	Fuzzy Inference System
FAST	Features from Accelerated Segment Test
GEO	geostationary orbit

GNSS	Global Navigation Satellite System
GPS	Global Positioning System
GPIO	General-Purpose Input/ Output
HE	Heading Error
HDOP	Horizontal DOP
IMU	Inertial Measurement Unit
IMP	Initial Map Matching Process
IGSO	inclined geosynchronous orbit
ISA	Inertial Sensor Assembly
IF	Ionosphere-Free
IGS	i
INS	Inertial Navigation System
KLT	Kanada-Lucas-Tomasi
KITTI	Karlsruhe Institute of Technology and Toyota Technological Institute
LAMBDA	Least-squares AMBIGUITY Decorrelation Adjustment
LOS	Line Of Sight
LLF	Local-level Frame
LBS	Location-Based Service
MEO	Medium Earth Orbit
MW	Melbourne-Wübbena
MEMS	microelectromechanical system
MM	Map Matching
NL	Narrow-lane

OSM	OpenStreetMap
PPP	Precise Point Positioning
P3P	Perspective 3-point Problem
PD	Perpendicular Distance
PCO	Phase Center Offset
PCV	Phase Center Variance
RDMS	Relational DataBase Management System
RANSAC	RANdom SAmple Consensus
RTK	Real-Time Kinematic
RMS	Root-Mean-Square
RTS	Real-time Service
RTCM	Radio Technical Commission for Maritime Services
SSR	State Space Representation
SIFT	Scale-Invariant Feature Transform
SURF	Speeded-Up Robust Feature
SMP	Subsequent Map Matching Process
TOA	Time Of Arrival
TOF	Time Of Flight
TOT	Time Of Transmission
UTC	Coordinated Universal Time
WL	Wide-lane
VO	Visual Odometry

List of Symbols

Symbols	Definition
A'_{IF}	The float ambiguities in meter
B	The baseline length between the two perspective centers
c	Light speed in vacuum
cdt^r	The receiver clock error
$cd\dot{t}$	The receiver clock drift
d_{sagnac}	The sagnac effect
d_{rel}	The relativity correction in meter
d_{Shap}	The Shapiro delay error in meter
d_{windLi}	The phase wind-up correction on L_i (m)
d_{trop}	The troposphere delay (m)
d_{ionoP}	The ionosphere effect on code
$d_{iono\Phi}$	The ionosphere effect on phase
f	Satellite clock frequency in the inertial system on the ground
f^r	Signal frequency on the satellite
f_x, f_y	The focal length of each image axis
F^l	The dynamic matrix of mechanization errors in local-level frame
G_{k-1}	The shaping matrix
GM_E	The earth gravitational constant
g^l	The normal gravity in local-level frame
H_k	The design matrix

I	Identity matrix
k_1, k_2, k_3	The radial distortion coefficients
K_k	The gain matrix
L_i	Carrier phase on L_i band
M_{wet}	Troposphere wet mapping function
M_{dry}	Troposphere dry mapping function
N_i	The integer ambiguities of L_i
P_k	The prior covariance of the state vector
P_{IF}	The ionosphere-free combination code measurement in meter
P_k	The posterior covariance of the state vector
P_f^w	The feature coordinates expressed in the world frame
P_{cam}^w	The perspective center coordinates expressed in the world frame
P_f^p	The feature coordinates obtained from the previous camera frame
p_1, p_2, p_3	The tangential distortion coefficients
R_m, R_n	The meridian radius of curvature, the radius of curvature of the prime vertical
R_i^j	The rotation matrix from frame i to frame j
r, p, y	Roll, Pitch, Yaw
S	The line of sight unit vector from the satellite to the receiver
T	The tropospheric delay
T_i^e	The perspective center at the epoch i expressed in the ECEF
ΔU	The difference of the earth's gravitational potential between the satellite and the geoid
u_0, v_0	The projection of perspective center on the image
u, v	The pixel coordinates of features on the image

$VTEC$	The vertical total electron content
v	Speed of moving object
v_{xr}, v_{yr}, v_{zr}	The land vehicle velocity in x , y and z direction in ECEF
v_{xs}, v_{ys}, v_{zs}	The satellite velocity in x , y and z direction in ECEF
w	The driving white noise
X_c, Y_c, Z_c	Feature coordinate in camera frame
\vec{X}^c	The vector from the perspective center of the features expressed in current camera frame
Z_{wet}	Troposphere zenith wet component
Z_{dry}	Troposphere zenith dry component
Z_k	The measurement vector
Φ_{IF}	The ionosphere-free combination phase measurement in meter
λ_{NL}	The narrow-lane wavelength of L1 and L2
λ_{WL}	The wide-lane wavelength of L1 and L2
φ, λ, h	Latitude, Longitude, Height
ω_{ab}^c	The angular rate vector of b with respect to a expressed in c
Ω_{ab}^c	The skew-symmetric matrix of ω_{ab}^c
$\delta f^a, \delta \omega^b$	The accelerometer bias, the gyro bias
α, β	The reciprocal of the correlation time of accelerometers and gyros
$\Phi_{k,k-1}$	The transition matrix
Ψ	The skew-symmetric matrix of the attitude errors
ρ	The distance between the satellite and receiver
$\Delta\theta$	The vertical gyro-rate reading

Chapter One: INTRODUCTION

1.1 Preamble

The land vehicle navigation system is becoming increasingly important in recent years since it is the foundation of other applications like the autonomous car, Location-Based Services (LBS) and fleet management. Lots of sensors and technologies (e.g. satellite navigation, inertial navigation, vision-based navigation, etc.) have been developed for land vehicle kinematic positioning and navigation. Different sensors and technologies have their own advantages and drawbacks, which inspire people to integrate different sensors to take full advantage of their benefits. Multi-sensor integrated navigation has become a hot topic in both academic and industrial areas.

One of the appealing positioning approaches is Global Navigation Satellite System (GNSS), which is capable of providing all-weather and worldwide positioning service. The GNSS receiver receives the messages containing the time of transmission (TOT) of the signals and the information about the satellite position. It also measures the time of arrival (TOA) of the signals of each satellite, according to its own clock. From the TOAs and the TOTs, the time of flight (TOF) values can be formed, which are (given the speed of light) approximately equivalent to the ranges between the satellites and receiver. With the known satellite position and ranges, the receiver position and clock errors can be estimated with at least four satellites.

However, the GNSS signals can be easily blocked or interfered, which limits its application in certain circumstances (Cannon, 2007). To enable seamless navigation, especially in GNSS challenging environments, alternative sensors and systems are needed to bridge the GNSS outage. Inertial Navigation System (INS), which contains Inertial Measurement Unit (IMU) as a main component, is a dead reckoning system, which integrates the rotation rates to obtain attitude

changes, and doubly integrates the accelerations to obtain velocity and position increments (Jekeli, 2001). INS is a self-contained navigation system but the errors of IMU output accumulate with time, resulting in degraded performance, especially for low-cost MEMS (Micro-Electro-Mechanical System) based IMUs (Petovello, 2003; Shin, 2005; Sukkarieh, 2000).

Vision-based navigation is another widely applied dead reckoning (DR) approach which utilizes continuously tracked features (landmarks) in consecutive frames to estimate the camera pose. With one image, based on the pin-hole model, the orientation information of features with respect to the optical center can be obtained. The features could lie in any position along the ray from the perspective center, resulting in unavailability of the depth information. The position of features can be obtained with a monocular camera by the intersection of rays from two perspective centers of two images with overlapped part during camera motion if camera motion is known (Ullman, 1979). This method has been explored by many researchers with different assumptions (D G Lowe, 1991; Poelman & Kanade, 1997; C. Tomasi & Kanade, 1993). Instead of using two overlapped images during camera motion, stereo cameras are capable of implementing intersection of rays from perspective centers simultaneously. The motion of perspective center can be obtained by resection with same features captured by consecutive images (Fraundorfer & Scaramuzza, 2012; Scaramuzza & Fraundorfer, 2011). Visual Odometry (VO) focuses on the estimation of the camera pose, which is a particular case of Structure from Motion (SFM). SFM tackles the problem of 3D reconstruction of both the structure and camera pose from image sets. It aims at the local consistency of the trajectory. In contrast to VO, simultaneous localization and mapping (SLAM) takes the feature coordinates into estimation as well, and it aims at the global consistency of the trajectory of the map (Bailey & Durrant-Whyte, 2006; Durrant-Whyte & Bailey, 2006). Stereo

VO, which consists of stereo cameras, is another self-contained system to estimate the motion of the platform. It can be applied in the land vehicle navigation as an alternative DR system. Similar to INS, Stereo VO suffers accumulated errors without external absolute positioning information. From the introduction of the three types of navigation systems above, it can be seen that each individual system has its own disadvantages. Multi-sensor integration is an effective way to take advantage of different systems and mitigate the disadvantages. Kalman filter has been widely used to optimally integrate different kinds of datasets and the integration can be conducted either in a 'loosely-coupled' or a 'tightly-coupled' mode. The loosely-coupled integration has a straightforward implementation scheme in which each individual system is working separately and the outputs from each system are fused by a Kalman filter. Unlike the loose integration, the tight integration utilizes only one single centralized Kalman filter where the raw measurements or the differences between predicted and actual measurements are directly used. Although the implementation of a tightly coupled integration is more complicated, the system can still work even when one individual system cannot output viable position solutions such as no position available with less than four visible GNSS satellites in certain harsh environments due to signal blockages (Moon, Hwang, Sung, & Lee, 2000).

The integration of GNSS and INS has been widely applied to increase the reliability and continuity of the system (Angrisano, 2010; Cannon, 2007; Petovello, 2003; Shin, 2005). In an integrated system, the inertial errors could be estimated with the GNSS measurements and therefore the accumulated error in INS can be avoided. On the other hand, the INS could help bridge the outage of GNSS when there are signal blockages to the navigation satellite signals. In addition to the position solution, an integrated system could also provide attitude solution which is important for

many applications. There are many other benefits of using an integrated system such as improved quality control of the positioning system (Du & Gao, 2012; Lee, Wang, & Rizos, 2003). Cameras are also increasingly integrated with GNSS to improve the overall performance and bridge GNSS outage due to cheaper price and capacity of proving system dynamics (Aumayer et al., 2014; Dusha & Mejias, 2012; Schleicher et al., 2009). GNSS denied environments, however, still exist where the GNSS signals could be blocked for a long time. An integrated system of IMU and cameras can provide navigation solutions over an extended time period with significant GNSS outages although INS and vision-based navigation both suffer error accumulation over time. With the integration of a monocular camera and IMU, the depth ambiguity of monocular camera can be solved by the dynamic information provided by the IMU (Kleinert & Schleith, 2010; Piniés, Lupton et al., 2007; Qian et al., 2001). As mentioned before, stereo cameras do not suffer the depth ambiguity since the feature coordinates can be obtained by triangulation of common features on the stereo images. Therefore, the integration of stereo cameras and IMU could be more flexible than the integration of IMU and monocular camera. For loose integration of INS/Stereo VO, one way is to apply the rotation and translation estimated by visual odometry to correct the corresponding initial states obtained by inertial datasets (Tardif, et al., 2010). Similarly, the inertial measurements of IMU could also be used to correct the ego-motion estimation by visual odometry (Konolige et al., 2007). Tight integration of Stereo VO and INS utilizes the raw measurements of each type of measurement to optimize the solution, which is expected to generate better estimation (Asadi & Bottasso, 2014; Carrillo et al., 2012; Liu et al., 2015, 2017; Usenko et al., 2016; Xian et al., 2015). Although the integration of INS and VO can reduce the accumulated errors in position solutions when there is GNSS outage, the system still suffers drift with time. To remove the accumulated

errors of a DR system, absolute positioning information is required. In GNSS denied environments, a digital map is another way to provide the absolute positioning information. Therefore, Map Matching can be further applied to a land vehicle navigation system using DR systems to improve the navigation accuracy (Balazadegan Sarvrood, 2016; Balazadegan Sarvrood & Amin, 2011; Brubaker et al., 2013; Floros et al., 2013). With Map Matching, the DR system solution can be projected on the digital map and the projected point position can be integrated to further improve the system accuracy. With the information provided by the projected point, the DR system errors can be largely reduced. To some extent, the accumulated errors can be avoided. When GNSS signal is available, the GNSS positioning dominates the system accuracy, especially when other low-cost navigation sensors are integrated. In an open sky environment, high-precision GNSS positioning is the key to improving the accuracy of land vehicle navigation. The GNSS positioning accuracy, however, is affected by many error sources (e.g. satellite orbit and clock, troposphere effects, sagnac effect, site displacements, antenna phase center correction, phase wind-up). In the past, the Real-Time Kinematics (RTK) technique is widely applied which can perform precise relative positioning of a rover receiver with respect to a base receiver whose position coordinates are known. In recent years, the Precise Point Positioning (PPP) method becomes popular which is able to perform precise positioning using a single receiver coupled with advanced GNSS error calibration methods and International GNSS Service (IGS) precise products (Abdel-salam, 2005; Bisnath & Gao, 2008; Gao Y, 2002; Kouba & Héroux, 2001; Rizos, Janssen, Roberts, & Grinter, 2012; M. Wang, 2014; Zumberge, Heflin, Jefferson, Watkins, & Webb, 1997). Usually, an ionosphere-free (IF) combination is applied in PPP to reduce the ionosphere delay. However, it usually takes tens of minutes before the position solution converges to a high precision in PPP,

which limits its applications. PPP ambiguity resolution (AR) has been proposed to fix the PPP ambiguities to accelerate the convergence (Collins, 2008; Ge, Gendt, Rothacher, Shi, & Liu, 2007; Laurichesse, D., Mercier, 2007). PPP AR aims to recover the integer property of the PPP ambiguities. An IF ambiguity can be decomposed as a wide-lane (WL) and a narrow-lane (NL) ambiguities. The WL ambiguities can be resolved by the Melbourne-Wübbena (MW) combination while the NL ambiguities can be fixed by the Least-squares AMBiguity Decorrelation Adjustment (LAMBDA) method. In most cases, PPP AR takes over ten minutes to fix the ambiguities due to a large search space for the NL ambiguities. It would be more challenging for PPP AR in kinematic mode due to lower quality of GNSS observations. Map Matching can be used to accelerate the PPP ambiguity resolution (Liu, 2017). With the aid of MM, the integer search space of ambiguities can be reduced so that fast PPP AR can be achieved.

In this thesis, a tightly coupled multi-sensor integration approach with IMU as the core sensor is proposed and implemented for land vehicle navigation. In the integrated system, the GNSS measurements and the visual measurements are applied to limit the accumulated errors in the inertial sensors. A tight integration of INS and Stereo VO using the feature pixel coordinates as raw measurement is used to output continuous navigation solutions in the GNSS-denied environment. The position, velocity and attitude errors together with the inertial sensor errors are estimated in a Kalman filter. To largely reduce the accumulated errors of the INS/Stereo VO integration system, Map Matching is also applied to provide the absolute positioning information independent of GNSS. In open sky environment, Map Matching is also used to accelerate PPP AR. The general aim of this thesis is to achieve center-meter level accuracy using PPP in open sky

environments and relative horizontal error within 1.2% with digital Map Matching for about 2 kilometers in GNSS-denied environment.

In the following part of this chapter, the backgrounds of GNSS, IMU and industrial camera are first introduced. A literature review is then provided with identified limitations, followed by the research objectives and contributions for this thesis. An outline of the thesis work is also given at the end.

1.2 Background

1.2.1 Global Navigation Satellite System

Currently, there are four GNSS systems in operation namely the United States' Global Positioning System (GPS), the Russian Federation's Global Orbiting Navigation Satellite System (GLONASS), Europe's Galileo system and China's BeiDou satellite navigation system (BDS). GPS is the first GNSS system to reach Full Operational Capability (FOC) in the world. The first launch was in 1978. All the GPS satellites are in medium earth orbit (MEO) with the altitude about 20,200 km. As of February 9, 2017, there are 12 Block IIF, 12 Block IIR and 7 Block IIR-M satellites are operational. All GPS satellites broadcast at the same two frequencies (L1 and L2), encoding signals using unique code division multiple access (CDMA). The 12 Block IIF satellites are broadcasting the additional third civilian L5 signal. The signals broadcasted by GPS satellites are summarized in Table 1.1.

The first launch of GLONASS was in 1982 and the system was completed in 1995. However, from the late 1990s, GLONASS was not in FOC until October 2011. The orbital height of GLONASS satellites is about 19,130 km. GLONASS broadcasts two types of signal (L1 and L2) as well. Different from other GNSS systems, GLONASS satellites transmit the same code as their

standard-precision signal on a different frequency using a 15-channel frequency division multiple access (FDMA) technique spanning either side from 1602.0 MHz ($1602+n*0.5625$ MHz, $n=-7\sim6$), known as the L1 band. The L2 signal adopts the similar FDMA strategy with center-frequencies $1246+n*0.4375$ MHz. At the moment (February 9, 2017), there are 24 GLONASS-M and 2 GLONASS-K1 satellites in operational. The GLONASS-K1 satellites contain CDMA signal L3OC. In the future, GLONASS-K2 and GLONASS-KM satellites broadcasting more CDMA signals will be launched. The details of GLONASS signals are summarized in Table 1.2.

Table 1.1 GPS signals

Signal	Block	Frequency (MHz)	PRN
L1	IIR, IIR-M, IIF	1575.42	IIR (G02, G11, G13, G14, G16, G18, G19, G20, G21, G22, G23, G28)
L2	IIR, IIR-M, IIF	1227.60	IIR-M (G05, G07, G12, G15, G17, G29, G31)
L5	IIF	1176.45	IIF (G01, G03, G06, G08, G09, G10, G24, G25, G26, G27, G30, G32)

All the Galileo satellites are running in MEO with the altitude about 23,222 km. There are 3 In-Orbit Validation (IOV) and 12 FOC Galileo satellites in service and 9 more satellites are to be launched to provide global service in near future. Galileo navigation signals are transmitted in four frequency bands as E1 (1575.42 MHz), E5a (1176.45 MHz), E5b (1207.14 MHz) and E6 (1278.75MHz) using CDMA.

Different from the other GNSS systems, BeiDou system consists of 6 geostationary orbit (GEO) satellites, 8 55-degree inclined geosynchronous orbit (IGSO) satellites and 6 medium earth orbit (MEO) satellites. BeiDou system began to provide services to customers in the Asia-Pacific region in December 2012 and the global service is planned in 2020. Triple-frequency signals are broadcasted by BeiDou system using CDMA, which are summarized in Table 1.3.

Table 1.2 GLONASS Signals

Satellite Block	L1, FDMA	L1, CDMA	L2, FDMA	L2, CDMA	L3, CDMA	L5, CDMA
GLONASS- M	L1OF, L1SF					
GLONASS- K1	L1OF, L1SF		L2OF, L2SF		L3OC	
GLONASS- K2	L1OF, L1SF	L1OC, L1SC	L2OF, L2SF	L2SC	L3OC	
GLONASS- KM	L1OF, L1SF	L1OC, L1OCM, L1SC	L2OF, L2SF	L2OC, L2SC	L3OC	L5OC
‘O’: open signal (standard precision), ‘S’: obfuscated signal (high precision); ‘F’: FDMA; ‘C’: CDMA						

Table 1.3 BDS Signals

Signal	Orbit	Frequency	Satellite PRN
B1	MEO, IGSO, GEO	1561.098	GEO (C01, C02, C03, C04, C05)
B2	MEO, IGSO, GEO	1207.140	IGSO (C06, C07, C08, C09, C10)
B3	MEO, IGSO, GEO	1268.520	MEO (C11, C12, C13, C14)

So far, the current GNSS constellations have been introduced. GNSS systems typically consist of three major parts, namely, the in-orbit satellites, the ground control and tracking stations, and the GNSS receivers. The ground control and tracking stations provide the satellites' position and clock information for users with corresponding GNSS receivers. GNSS positioning has been widely used in various applications with different accuracy requirements (e.g. automobile navigation, land surveying, deformation monitoring, etc.) (Sickle, 2008; Skog & Handel, 2009; M. Wang, 2008). Usually, low-cost consumer-grade GNSS receivers can only achieve meter level accuracy. For GNSS precise applications in which centimeter to decimeter level accuracy is required, survey grade GNSS receivers are needed.

To achieve high accuracy, Real-Time Kinematic (RTK) technique is widely applied. RTK requires a base station to broadcast its observations to the rover receivers through the communication link (e.g. radio). Then, the differential GNSS positioning algorithms can be adopted at the rover end with their own observations and the received messages. The differential algorithm is supposed to remove the satellite and receiver biases by double differencing the observations. Moreover, the distance between the base station and the rover station is usually within 10 km, the common atmosphere errors can be largely reduced as well, resulting in millimeter to centimeter level

solution. Besides, the high-accuracy solution can be achieved in short time using Least-squares AMBIGUITY Decorrelation Adjustment (LAMBDA) method proposed by Teunissen (1995). The main limitation of the conventional RTK is the short distance requirement because of the communication between the base and rover stations. To overcome this drawback, Network RTK is proposed with a network of evenly distributed base stations. The data from the base stations are processed in a control center. The sophisticated orbit, ionosphere and troposphere errors are estimated using the network, and virtual observations are formed and broadcasted to rover receivers through cellular communication to conduct RTK.

Apart from RTK, Precise Point Positioning (PPP) is another increasingly widely used positioning technique. Different from RTK, in which at least two receivers are required to implement differential positioning algorithms to achieve accurate solution, PPP is capable of providing worldwide accurate solution with just one receiver. Therefore, it saves the hardware costs and overcomes the distance limitation. The key to implementing PPP is the application of precise satellite orbit and clock products and the error source models, which are illustrated in Chapter 2.

1.2.2 Inertial Navigation System (INS) and Low-Cost MEMS IMU

Inertial Navigation System (INS) is a self-contained system capable of determining navigation states of moving objects (e.g. position, velocity and attitude) using triad accelerometers and gyroscopes to measure the acceleration and rotation respectively (Angrisano, 2010). With known previous states, measurements are integrated once for gyroscopes and twice for accelerometers to yield orientation and relative position respectively (Noureldin, Karamat, & Georgy, 2013). Inertial Measurement Unit (IMU) is a device which contains the Inertial Sensor Assembly (ISA) constituting of inertial sensors and related electronics in a unit. The interrelationship of ISA, IMU

and INS is summarized in Figure 1.1. Based on the performance, IMU could be categorized as navigation grade, tactical grade and consumer grade, which is illustrated in Table 1.4.

With the development of microelectromechanical system (MEMS) technology, the low-cost MEMS-based IMUs are widely used in various applications (e.g. land vehicle navigation, mobile mapping). Since the MEMS-based IMU outputs are corrupted with significant sensor errors, MEMS IMUs are often categorized as consumer grade. The performance of some more expensive MEMS IMU could reach close to tactical grade (e.g. Crossbow NAV 440). Currently, for land vehicle navigation, the state-of-art technology can achieve within 25 meters (RMS) using low-cost MEMS IMU (customer grade) after 5 minutes with relative horizontal error about 1%.

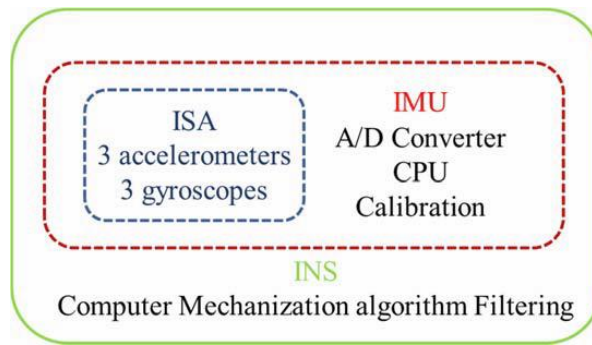


Figure 1.1. An illustration of terminologies used in INS and their interrelationship

(Noureldin et al., 2013)

Table 1.4 Different Grade IMUs (El-Sheimy, 2013)

Performance	Navigation Grade	Tactical Grade	Consumer Grade
Gyro drift rate (deg/hr)	≈ 0.015	0.1~10	100~3600
Accel bias (mg)	0.05~0.1	0.2~1	100~500
Price (USD)	150K~250K	100K~150K	10~100

1.2.3 Visual Odometry (VO) and Industrial Camera

Similar to INS, Visual Odometry (VO) is another self-contained navigation system using video cameras with detected and tracked (or matched) features. The pixel coordinate change of the tracked (or matched) features on consecutive images reflects the motion of the optical center. Industrial cameras are usually used in VO due to their light weight and good performance. The price of industrial cameras varies from several hundred to thousands of USD, based on their sensor format, resolution, frames-per-second (FPS), the capability of synchronization, etc.

Several specifications of cameras have to be taken into consideration when they are utilized in visual odometry. The first things to be considered are the sensor format (or sensor size) and the focal length. The sensor format is the shape and size of the image sensor, and the focal length of the lens is the distance between the lens and the image sensor. Based on the application scenario, the approximate object distance is known. The sensor format, focal length and the object distance determine the field of view. The relationship among the focal length, object distance, field of view and the object distance can be simplified as

$$focal_length \cong \frac{sensor_format \times object_dist}{field_of_view}$$

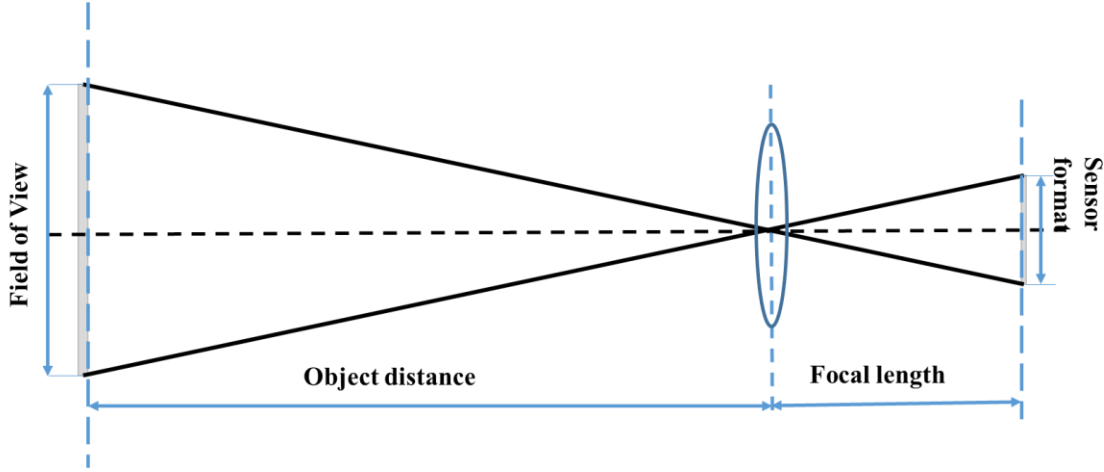


Figure 1.2 Sensor Format, Focal Length and Field of View

Camera resolution defines how many individual pixels are available to record the actual scene, which describes both pixel count and pixel density. It is usually measured in megapixels (meaning millions of pixels) with width by height. The larger the resolution is, the more details can be presented on images due to more information being recorded by more pixels. The sensor format divided by the number of pixels is the unit pixel size. Larger pixel size can gather more photons in certain time, which means better performance in insufficient illumination circumstances.

1.3 Literature Review and Limitations

For multi-sensor integration, Soloviev and Miller (2012) proposed the navigation mechanization with a self-contained IMU as the core sensor while externally-dependent sources of navigation information are treated as secondary sensors. Wang et al., (2015) developed the integration stragery without distinguishing the core sensor and secondary sensors. Most of the studies are based on the first architecture including this thesis. A considerable number of studies have

discussed the integration of INS and Stereo VO. Tardif et al., (2010) applied the rotation and translation estimated by visual odometry to correct the mechanization results obtained by inertial sensors in a loosely coupled integration. Carrillo et al., (2012) and Strelow (2004) used inertial and visual measurements to correct motion under certain assumptions. Bottasso et al. (2008) employed the inertial data to provide the information of the platform motion instead of assuming certain motion model. In this implementation, feature positions are also included in the filter state vector, which may increase the filter failure probability. Veth & Raquet, (2006) filtered out stale features whose tracking are lost for a given period to simplify the data association. Gopaul et al., utilized multiple over-lapping image frames with time-differencing measurements to reduce the number of unknowns in the filter and optimize the integration results. Asadi and Bottasso (2014) summarized and compared the methods of tight integration of INS and Stereo VO. Xian et al. (2015) analyzed the impact of feature distance in the integration. Kong et al., (2015) utilized line measurements in addition to the point features. Usenko et al. (2016) excluded the feature position in the state vector. Most of these works focus on implementation in a self-defined local frame. Conventional INS error model in the local-level frame is seldomly used in the previous implementations. Liu et al, (2015) and Liu et al, (2017) proposed the implementation architecture of tightly coupled integration of INS/Stereo VO formed in the local-level frame for land vehicle navigation.

However, few researcheres provide the implementation procedures of the tight integration of Stereo VO and INS, especially how the pixel coordinates of the features can be applied to estimate the errors in the state vector. Besides, most of the previous implementations are conducted in a self-defined local frame, which is not convenient for applications using geodetic coordinates. In

this thesis, how the pixel coordinates are used in the tight integration of INS and Stereo VO is derived and explained. In this implementation, 15 parameters are estimated in the Kalman filter including the errors in position, velocity, attitude and accelerometer, gyro biases. The difference between the predicted pixel coordinates based on the IMU and the actual measurements on the images is applied to estimate the errors. The IMU mechanization is conducted in the local-level frame and the matrices in the Kalman filter are illustrated in detail. The tight integration architecture is based on the IMU as the core sensor and it can be extended with GNSS by expanding the state vector with receiver clock error and receiver clock drift. In the integration of GNSS/INS/Stereo VO, the inertial measurements are applied all the time to provide the dynamic information of the land vehicle. When either GNSS or visual measurements are available, the measurements are applied in the Kalman filter to estimate the errors.

Map Matching is another appealing way to reduce the accumulated errors in DR systems. Floros et al. (2013) adopted chamfer matching and particle filter to integrate Stereo VO and digital map. Specifically, the particles representing the land vehicle position are generated based on the VO results. Chamfer matching is applied to find out the most matched road link according to the trajectory. Then particle filter is used to optimize the localization. Mismatching may happen if the vehicle is traveling in an area where the shapes of road links are very similar to those around (e.g. mesh-like road links). Brubaker et al. (2013) proposed using visual odometry and digital map to determine the probabilistic location on the digital map. In this method, sample training is needed. In this work, The method proposed in this work is based on the INS/VO solutions and fuzzy logic Map Matching. The tight integration solution is directly projected on the digital map based on the

fuzzy logic algorithms, which avoids the sample training. Besides, mismatching can be greatly reduced.

When the land vehicle is moving in open sky environment, GNSS dominates the system accuracy. High-precision GNSS positioning is the key to improving the accuracy of land vehicle navigation. PPP is an increasingly widely applied accurate method using just one receiver which saves the hardware cost and communications between the base and rover stations in RTK. PPP has been studied by many researchers in recent years (Abdel-salam, 2005; Bisnath & Gao, 2008; Gao Y, 2002; Kouba & Héroux, 2001; Rizos et al., 2012; M. Wang, 2014; Zumberge et al., 1997). The main disadvantage of PPP is that it needs significant time to reach convergence. Fast ambiguity resolution (AR) is requested to reduce the convergence time. To recover the integer property of PPP ambiguities, Collins (2008) proposed the decoupled clock concept, Ge et al. (2007) developed the fractional cycle biases (FCB) product, and Laurichesse (2007) proposed the integer clock method. However, it still takes a few tens of minutes to obtain reliable ambiguity resolution if only with dual-frequency observations. This is because the large noise of code measurements leads to a long time smoothing with Melbourne-Wübbena (MW) combination (W.G., 1985; Wübbena, 1985). Moreover, the narrow-lane (NL) ambiguities need more than ten minutes to be fixed due to short wavelength (Geng, Teferle, Meng, & Dodson, 2011). The current methods cannot fix the ambiguities in a short time. The method to accelerate the PPP ambiguity resolution still needs to be explored to make PPP suitable for applications. Balazadegan Sarvrood et al. (2017) adopted the Map Matching to project the PPP solution on an accurate digital map to accelerate the convergence. However, Map Matching to accelerate PPP AR is not discussed. In this thesis, PPP is tightly

integrated with Map Matching, which accelerates the PPP ambiguity resolution in kinematic mode. The implementation procedures are illustrated and field test results are presented and analyzed.

1.4 Research Objectives and Contributions

The main objectives of this thesis are to develop a tightly coupled GNSS/INS/Stereo VO integration system for land vehicle navigation with the IMU as the core sensor. When the GNSS signals are blocked, the tightly coupled INS/ Stereo VO method can still provide continuous solutions. The implementation details are presented and how the pixel coordinates of tracked features can be used in the estimation is illustrated. The system is also extended with GNSS when GNSS is available. Map Matching as another way of providing external position information for INS/ Stereo VO in GNSS denied environment is integrated to largely reduce the system drift. In addition, when the land vehicle is moving in open sky environment, the method of applying MM to aid PPP AR in kinematic mode is investigated. To fulfill the goals, the specific objectives are as follows:

1. To derive and develop the method of tightly coupled integration of Stereo VO and INS.

The tight integration utilizes the pixel coordinates on the images to limit the quick drift of INS. The method and the matrices in the Kalman filter need to be explored and illustrated. Field tests are needed to evaluate the system performance.

2. To expand the tightly coupled Stereo VO and INS system with PPP. The integrated system will employ IMU as the core sensor for the Kalman filter. When either GNSS or visual measurements are available, the errors in the state vector can be estimated to improve the system accuracy. The system architecture needs to be explored.

3. To develop the integrated Stereo VO, INS and Map Matching system in GNSS denied environment. Map Matching is used to project the Stereo VO and INS solutions on the digital map and the projected points are used to largely reduce the accumulated errors. Field tests are needed to verify the effectiveness.
4. To develop the fast PPP ambiguity resolution method in kinematic mode with the aid of Map Matching. Map Matching provides external position information by projecting the PPP solution on the digital map, which reduces the integer search space for PPP ambiguities.

The major contributions of this thesis include:

1. Development of a tightly integrated system for INS and VO to improve the system accuracy in GNSS denied environments. The implementation procedures of using pixel coordinates of tracked features on the images are presented in detail.
2. Development of a tightly coupled integration scheme for GNSS PPP, INS and VO with IMU as the core sensor. The IMU acts as the core sensor to provide dynamic information of the navigation system while the GNSS pseudorange, carrier-phase and Doppler measurements together with the pixel coordinates of features captured by cameras are utilized to optimize the solution.
3. Development of Map Matching (MM) integration with INS/Stereo VO system to provide absolute positioning information to further improve the navigation system accuracy without GNSS.

4. Implementation and analysis of fast PPP AR in kinematic mode with the aid of Map Matching. The MM has reduced the integer ambiguity search space, and the PPP ambiguities can be fixed in a short time after MM is conducted.

1.5 Thesis Outline

Chapter 2 introduces the fundamentals of different positioning systems used in this thesis including PPP, INS and VO. The error sources, float and fixed solution of PPP are introduced. The mechanization and error models of INS are reviewed. For Stereo VO, the used coordinate frames and the implementation procedures are illustrated.

In Chapter 3, the integration scheme with IMU as the core sensor in this thesis is illustrated. The tightly coupled integration of INS and Stereo VO is illustrated in detail. The integration is also extended with GNSS, and the matrices are introduced.

The fuzzy logic Map Matching is introduced in Chapter 4. The application of Map Matching with Stereo VO and INS integration system is presented, which effectively reduces the accumulated errors. The fast PPP AR method with the aid of MM is also investigated in this chapter.

Chapter 5 provides the field test results. Datasets collected by KITTI are applied to verify parts of the proposed methods. Field tests in Calgary also proved the effectiveness of the methods proposed. Test settings in Calgary are explained in detail including the synchronization, calibration, etc. Analysis of the tests results using both datasets is provided.

Chapter 6 summarizes the conclusions and provides the suggestions for the future work.

Chapter Two: FUNDAMENTALS OF NAVIGATION SYSTEMS USING GNSS PPP, INS AND STEREO VO

The fundamentals of GNSS PPP, INS and Stereo VO are introduced in this chapter, including the GNSS error sources, PPP float and fixed solution, coordinate frames used in INS, INS mechanization and error models in the local-level frame, Stereo VO coordinate frames and implementation procedures.

2.1 Precise Point Positioning

Precise Point Positioning can achieve centimeter to decimeter level positioning accuracy using one single GNSS receiver with precise satellite orbit, clock products and advanced GNSS error calibration models (Navipedia, 2011; Zumberge et al., 1997). Compared with RTK, there is no spatial limit for PPP since it does not need to communicate with the base station. However, error source modeling for PPP is much more complex than the one for RTK. The error sources for PPP are illustrated in Section 2.1.1. After having applied of the error source models and IGS precise products, one can achieve centimeter-level float solution after convergence. Usually, it takes tens of minutes for PPP to reach convergence. PPP Ambiguity resolution (AR) can potentially reduce the convergence time and improve the positioning accuracy.

2.1.1 GNSS Error Sources and Mitigation

There are multiple error sources for GNSS positioning including the satellite orbit and clock errors, Sagnac effect due to earth rotation, relativistic effect with high satellite speed, atmosphere delay when passing through the atmosphere and site displacements on the ground.

2.1.1.1 Satellite orbit and clock

International GNSS Service (IGS) provides different types of satellite orbit and clock products with different accuracies and latencies for GPS and GLONASS, which are summarized in Table 2.1.

Table 2.1 Satellite Orbit and Clock Errors (IGS 2017)

Type		Accuracy	Latency	Updates	Sample Interval
Broadcast	orbits	~100 cm	real time	--	daily
	Sat. clocks	~5 ns RMS ~2.5 ns SDev			
Ultra-Rapid (predicted half)	orbits	~5 cm	real time	at 03, 09, 15, 21 UTC	15 min
	Sat. clocks	~3 ns RMS ~1.5 ns SDev			
Ultra-Rapid (observed half)	orbits	~3 cm	3 - 9 hours	at 03, 09, 15, 21 UTC	15 min
	Sat. clocks	~150 ps RMS ~50 ps SDev			
Rapid	orbits	~2.5 cm	17 - 41 hours	at 17 UTC daily	15 min
	Sat. & Stn. clocks	~75 ps RMS ~25 ps SDev			5 min
Final	orbits	~2.5 cm	12 - 18 days	every Thursday	15 min
	Sat. & Stn. clocks	~75 ps RMS ~20 ps SDev			Sat.: 30s Stn.: 5 min

It can be seen from Table 2.1 that the accuracy of the widely used real-time broadcast ephemeris is about 1 meter, which cannot satisfy the requirement of PPP applications. The rapid and final products are accurate enough to be applied in post-mission PPP. The ultra-rapid (predicted half)

product is available in real time with orbit accuracy about 5 centimeters. However, the inaccurate satellite clock (45 cm) prevents the application in real-time PPP. To satisfy the increasing demands in real-time PPP, IGS announced the launch of Real-Time Service (RTS) (Inside GNSS, 2013), which provides the satellite orbit and clock corrections to the broadcast ephemeris as Radio Technical Commission for Maritime Services (RTCM) v3 State Space Representation (SSR) standard (IGS, 2010). The RTS accuracy was claimed as about 3 cm RMS for orbit and about 4.5 cm STD for clock (IGS RTS Monitor, 2013). Apart from this, the Multi-GNSS EXperiment (MGEX) project can provide final precise ephemeris products for BeiDou, Galileo and QZSS systems (Montenbruck & Et.al, 2014; Rizos et al., 2013).

2.1.1.2 Relativistic Effect

Due to the high speed (about 4 km/s) of satellites at the altitude of about 20200 km with respect to the user receiver located on earth surface, the relativistic effect has to be taken into consideration for PPP (Xu, 2003), which is given as

$$\frac{f - f'}{f'} = -\frac{1}{2} \left(\frac{v}{c} \right)^2 - \frac{\Delta U}{c^2} \quad (2.1)$$

where f is the satellite clock frequency in the inertial system on the ground; f' is the signal frequency on the satellite; v is the speed of moving system; c is the light speed in the vacuum; ΔU is the earth's gravitational potential difference between the satellite and the geoid.

Since the fundamental frequency of satellite clock of GPS is $f=10.23$ MHz, according to Eq (2.1) and the assumption of a circular GPS orbit, the constant offset would be $f - f' = -0.00457$ Hz, which has to be tuned before the satellite launch. However, the satellite orbit is eccentric, which is

not the same as the assumption. The gravitational potential and velocity of the satellite varies, which leads to an additional correction for the relativity correction as (Parkinson & Enge, 1996)

$$d_{rel} = \frac{-2\vec{r}_s \cdot \vec{v}_s}{c} \quad (2.2)$$

where d_{rel} is the relativity correction in meter; \vec{r}_s and \vec{v}_s are the satellite position (m) and velocity (m/s) in the inertial system. The vector dot product could be evaluated in Earth-Centered, Earth-Fixed (ECEF).

Apart from this, the relativistic effect also has an impact on the signal propagation namely Shapiro delay. When GNSS signal passes through the Earth's gravity field, the corresponding error generated can be given as (Xu, 2003)

$$dShap = \frac{2GM_E}{c^2} \ln \left(\frac{R_r + R_s + \rho}{R_r + R_s - \rho} \right) \quad (2.3)$$

where $dShap$ is the Shapiro delay error in meter; GM_E is the earth gravitational constant; R_r is the geocentric distance of receiver (m); R_s is the geocentric distance of satellite (m); ρ is the geometric distance between the satellite and receiver (m). The combination of Eq (2.2) and Eq (2.3) would be the error corrected for relativistic effect on GNSS signals.

2.1.1.3 Antenna Phase Center Offset and Variation

Antenna Phase Center (APC) is the point where the GNSS signal is emitted or received. It varies with the orientation of the signal emitted or received. Antenna Reference Point (ARP) is usually used to represent the position. For example, the satellite antenna ARP is selected as the satellite Center of Mass (CM) and the receiver antenna ARP is usually selected as the center of the bottom surface of the receiver antenna. The offset between the APC and ARP is constituted of a mean

offset part and a variation depending on the signal orientation. The mean offset is called antenna Phase Center Offset (PCO) while the variation part is named Phase Center Variation (PCV). To achieve centimeter-level accuracy positioning, PCO and PCV have to be taken into consideration. Satellite and receiver PCO and PCV values are provided in an IGS atx file which can be downloaded from <ftp://www.igs.org/pub/station/general>.

2.1.1.4 Phase Wind-up Effect

Phase wind-up error exists in the phase measurements associated with the satellite and receiver antenna orientation due to the nature of circularly polarised waves intrinsic in the GNSS signals. For a static receiver, the phase wind-up error is generated due to the motion of satellites. This effect is generally neglected in differential positioning. However, it is significant for undifferenced point positioning. The phase wind-up for satellite can be modeled as (Wu, et al., 1992)

$$\begin{aligned}
 d_{wind_{Li}} &= \lambda_{Li} \left(N + \frac{\delta\phi}{2\pi} \right) \\
 N &= \frac{d_{previous}}{\lambda_{Li}} - \frac{\delta\phi}{2\pi} \\
 \delta\phi &= \text{sign}[\vec{k} \cdot (\vec{D}' \times \vec{D})] \cos \left(\frac{\vec{D}' \cdot \vec{D}}{|\vec{D}'| \cdot |\vec{D}|} \right) \\
 \vec{D}' &= \vec{\hat{x}}' - \vec{k} \cdot (\vec{k} \cdot \vec{\hat{x}}') - \vec{k} \times \vec{\hat{y}}' \\
 \vec{D} &= \vec{\hat{x}} - \vec{k} \cdot (\vec{k} \cdot \vec{\hat{x}}) + \vec{k} \times \vec{\hat{y}}
 \end{aligned} \tag{2.4}$$

where $d_{wind_{Li}}$ is the phase wind-up correction on L_i (in unit of meter); λ_{Li} is the wave length; $d_{previous}$ is the phase wind-up effect at the previous epoch; the initial phase wind up can be set as 0; \vec{k} is the satellite to receiver unit vector; $\vec{\hat{x}}'$ and $\vec{\hat{y}}'$ are the first two components of the satellite body unit

vector $(\vec{\hat{x}}', \vec{\hat{y}}', \vec{\hat{z}}')$ expressed in ECEF; $\vec{\hat{x}}$ and $\vec{\hat{y}}$ are the first two components of the receiver unit vector $(\vec{\hat{x}}, \vec{\hat{y}}, \vec{\hat{z}})$ in east, north and up directions.

2.1.1.5 Troposphere Delay

When GNSS signal passes through the troposphere (0 to ~40 km above ground), it suffers non-dispersive delay caused by the water vapor and gases. The troposphere delay can be divided into two main parts namely the wet and dry components. The wet component is caused by the lower part of troposphere which mainly consists of water vapor. Since the water vapor density in this part varies with position and time, the wet component is difficult to model. The dry component is caused by gases in both the lower part and higher part, which can be easily modeled (Ahmed El-Rabbany, 2002). The wet and dry components of troposphere delay are usually modeled at zenith and then mapped to Line of Sight (LOS) direction by mapping functions, which can be given as

$$d_{trop} = M_{wet} Z_{wet} + M_{dry} Z_{dry} \quad (2.5)$$

where d_{trop} is the troposphere delay (m); M_{wet} and M_{dry} are the wet and dry mapping functions respectively; Z_{wet} and Z_{dry} are the zenith wet and dry components (m) respectively.

Different zenith models (e.g. Saastamoinen, Hopfield, Black-Eisner, etc.) and mapping functions (Davis, Chao, Marini, Niell, Global Mapping Function, etc.) have been widely used. One widely applied zenith model is Saastamoinen, which is given as

$$Z_{dry} = \frac{(0.0022768 \pm 0.0000005)P_0}{1 - 0.00266 \cos(2\varphi) - 0.00028H}$$

$$Z_{wet} = \frac{0.002277 \left(\frac{1255}{T_0} + 0.05 \right) e_0}{1 - 0.00266 \cos(2\varphi) - 0.00028H} \quad (2.6)$$

where P_0 is the total surface pressure (mbar) at the receiver location; φ is the latitude of the receiver; H is the orthometric height of the receiver (km); T_0 is the temperature in Kelvin and e_0 is the water vapor pressure observed at the receiver location. With real pressure P_0 , the accuracy of modeled dry component can be at millimeter-level while the wet component cannot reach such a high accuracy. Therefore, the uncalibrated wet component is usually estimated in PPP together with other unknowns. One example for troposphere mapping function is Neill, given as

$$M = \frac{1 + \frac{a}{1 + \frac{b}{1 + c}}}{\sin(ele) + \frac{a}{\sin(ele) + \frac{b}{\sin(ele) + c}}} \quad (2.7)$$

where ele is the satellite elevation; a , b and c are the empirical coefficients, which can be looked up in the table provided by Niell (1996).

2.1.1.6 Ionosphere Delay

The ionosphere is the higher part of the atmosphere (above 85 km from the ground). The ionized particles in the ionosphere would cause a dispersive-dependent effect on GNSS signals. Ionosphere advances the carrier-phase but delays the code measurements at the same frequency with the same magnitude. The ionosphere zenith error on code and phase measurements can be modeled as

$$\begin{aligned} d_{ionoP} &= \frac{40.3}{f^2} VTEC + \frac{s_2}{f^3} + \frac{s_3}{f^4} \\ d_{iono\Phi} &= -\frac{40.3}{f^2} VTEC - \frac{s_2}{f^3} - \frac{s_3}{f^4} \end{aligned} \quad (2.8)$$

where d_{ionoP} and $d_{iono\Phi}$ (m) are the ionosphere effect on code and phase respectively; the three items on the right side of equations are first-, second- and third-order ionospheric errors; $VTEC$ is the

vertical total electron content; f is the signal frequency; s_2 and s_3 are scalars related to the second- and third-order ionospheric errors.

The first-order ionospheric error accounts for about 99.9% of the total ionosphere effect while the second- and third-order accounts for about 0.1% which can be neglected in PPP. When dual-frequency observations can be received, based on Eq (2.9), the majority of ionospheric error can be removed by the combination of two different frequencies, given as

$$\begin{aligned} P_{IF} &= \frac{f_1^2}{f_1^2 - f_2^2} P_1 - \frac{f_2^2}{f_1^2 - f_2^2} P_2 \\ \Phi_{IF} &= \frac{f_1^2}{f_1^2 - f_2^2} \Phi_1 - \frac{f_2^2}{f_1^2 - f_2^2} \Phi_2 \end{aligned} \quad (2.9)$$

where P_{IF} and Φ_{IF} are the ionosphere-free code and phase measurements (in unit of meter). The first-order ionospheric error is eliminated in the combination.

2.1.1.7 Sagnac Effect

The time calculation in GNSS are performed assuming in an inertial system (Ashby, 2003). However, traveling from the transmitter to receiver, the signal obtained at the receiver location suffers a shift due to the movement of the receiver on earth surface with earth rotation, which needs to be carefully accounted for (Caligiuri & Sorli, 2014).

The sagnac effect for GNSS signals can be written as (Parkinson & Enge, 1996)

$$d_{sagnac} = \frac{(\vec{r}_r - \vec{r}_s) \cdot \vec{v}_r}{c} \quad (2.10)$$

where d_{sagnac} is the sagnac effect (m); \vec{r}_r is the geocentric vector of the receiver while \vec{r}_s is the geocentric vector of the satellite; \vec{v}_r is the velocity vector of the receiver; c is the light speed in the vacuum.

2.1.1.8 Site Displacements

Site displacement is referred to effects of earth elastic deformation due to time-varying surface loads. To be consistent with the commonly used reference frames such as ITRF2008, some periodic receiver site displacements have to be taken into consideration, including solid earth tides, the polar tides and the ocean loading.

According to Kouba (2009), the solid earth tide can be expressed as

$$\begin{aligned}
 d_{se\vec{t}} &= \sum_{j=2}^3 \frac{GM_j R_E^4}{GM_E R_j^3} \left\{ h_2 \hat{r}_r \left[1.5 (\hat{R}_j \cdot \hat{r}_r)^2 - 0.5 \right] + 3l_2 (\hat{R}_j \cdot \hat{r}_r) \left[\hat{R}_j - (\hat{R}_j \cdot \hat{r}_r) \hat{r}_r \right] \right\} \\
 &+ \left[-0.025m \cdot \sin \varphi \cos \varphi \sin(\theta_g + \lambda) \right] \hat{r}_r \\
 h_2 &= 0.6078 - 0.0006 \left[(3 \sin^2 \varphi - 1) / 2 \right] \\
 l_2 &= 0.0847 + 0.0002 \left[(3 \sin^2 \varphi - 1) / 2 \right]
 \end{aligned} \tag{2.11}$$

where $d_{se\vec{t}}$ is the solid earth tide displacement vector; GM_E is the gravitation parameter of the earth; GM_j is the gravitation parameter of moon ($j=2$) and sun ($j=3$); \hat{R}_j and R_j are the geocentric unit vector of the moon ($j=2$) or the sun ($j=3$) and the magnitude of the geocentric vector; l_2 and h_2 are the nominal second degree Love and Sheba dimensionless numbers; \hat{r}_r is the geocentric unit vector of the receiver; m is the order of the spherical harmonics; φ , λ and θ_g are the site latitude, longitude and the Greenwich Mean Sidereal Time.

The ocean loading site displacement is caused by ocean tides on the underlying crust. Usually, 11 tidal waves (e.g. the semi-diurnal waves M_2 , S_2 , K_2 and N_2 ; the diurnal waves O_1 , K_1 , P_1 and Q_1 ; the long-period waves M_f , M_m and M_{sa}) are taken into account. The ocean loading displacement can be expressed as (Gérard & Luzum, 2010)

$$d_{ol\vec{t}} = \sum_{i=1}^{11} f_i A_{ci} \cos(\omega_i t + \chi_i + u_i - \Phi_{ci}) \tag{2.12}$$

where d_{oi} is the site displacement vector due to ocean loading in radial, west and south directions respectively; i represents the tidal waves introduced above; A_{ci} and Φ_{ci} are the amplitude and phase of the i^{th} wave at a station; t is the computing time, ω_i is the angular velocity of the i^{th} wave; χ_i is the astronomical argument at time of 0 hour; f_i and u_i depend on the longitude of the lunar node. For polar tides, using the second degree Love and Shida numbers mentioned above, the model for latitude and longitude and height can be illustrated as (Kouba, 2009)

$$d_{pi} = \begin{Bmatrix} -9 \cos(2\varphi) [(x_p - \bar{x}_p) \cos \lambda - (y_p - \bar{y}_p) \sin \lambda] \\ -9 \sin \varphi [(x_p - \bar{x}_p) \sin \lambda + (y_p - \bar{y}_p) \cos \lambda] \\ -32 \sin(2\varphi) [(x_p - \bar{x}_p) \cos \lambda + (y_p - \bar{y}_p) \sin \lambda] \end{Bmatrix} \quad (2.13)$$

where d_{pi} is the pole tide displacement in north, east and up directions; $(x_p - \bar{x}_p)$ and $(y_p - \bar{y}_p)$ are the pole coordinate variations from the mean polar (\bar{x}_p, \bar{y}_p) in arcseconds. The mean polar calculation can be found at IERS Conventions (Gérard & Luzum, 2010).

2.1.1.9 Summary of Error Sources

The magnitudes of the errors for GNSS signals and the corresponding mitigation techniques are summarized in Table 2.2. Generally, the satellite orbit and clock can be compensated by using IGS precise products. The ionosphere delay can be largely reduced by forming ionosphere-free combination measurements. The troposphere delay can be first corrected by mathematical model. Then the residual wet delay at zenith can be estimated. The satellite and receiver antenna PCOs and PCVs can be compensated by applying the IGS atx file. The other types of error can be corrected by applying corresponding mathematical models illustrated in Section 2.1.1.

Table 2.2 Summary of GNSS Errors

GNSS error sources	Error impact	Compensation approaches
Orbit error of broadcast ephemeris	~1 m	Use precise orbit product
Clock error of broadcast ephemeris	~5 ns	Use precise clock product
Sagnac effect	> 250 ns	Eq (2.10)
Relativistic effect on satellite clock	~2 m	Eq (2.2)
Relativistic effect on signal propagation	~1-2 cm	Eq (2.3)
Ionosphere	4~30 m	Eq (2.9)
Troposphere	3~15 m	Eq (2.5)
Satellite antenna PCO	Up to 3 m	IGS atx file
Satellite antenna PCV	1~2 cm	IGS atx file
Receiver antenna PCO	Up to 20 cm	IGS atx file
Receiver antenna PCV	~1 cm	IGS atx file
Phase wind-up	> 0.1 cycles	Eq (2.4)
Solid earth tide	~ 30 cm	Eq (2.11)
Ocean tide	<5 cm	Eq (2.12)
Pole tide	<2.5 cm	Eq (2.13)

2.1.2 PPP Float Solution

With the IGS precise products and error models introduced in the previous section, Precise Point Positioning (PPP) using ionosphere-free (IF) code and carrier-phase observations can achieve centimeter-level accuracy after convergence (Navipedia, 2011; Zumberge et al., 1997). The

obtained PPP solution is called float solution since the estimated ambiguities are real numbers and cannot be decomposed as integers. The PPP float ambiguities take tens of minutes to reach convergence and the biases are absorbed into the ambiguities. The details are introduced as follows. After applying the error source models in Section 2.1.1, the undifferenced ionosphere-free code and carrier-phase observation model can be formed as

$$\begin{aligned}
P_{IF} &= \frac{f_1^2}{f_1^2 - f_2^2} P_1 - \frac{f_2^2}{f_1^2 - f_2^2} P_2 \\
&= \rho + (cdt^r + b_{P_{IF}}^r) - (cdt^s + b_{P_{IF}}^s) + T + \varepsilon(P_{IF}) \\
&= \rho + cdt_{P_{IF}}^r - cdt_{P_{IF}}^s + T + \varepsilon(P_{IF}) \\
\Phi_{IF} &= \frac{f_1^2}{f_1^2 - f_2^2} \Phi_1 - \frac{f_2^2}{f_1^2 - f_2^2} \Phi_2 \\
&= \rho + (cdt^r + b_{\Phi_{IF}}^r) - (cdt^s + b_{\Phi_{IF}}^s) + T + \lambda_{IF} N_{IF} + \varepsilon(\Phi_{IF}) \\
&= \rho + cdt_{\Phi_{IF}}^r - cdt_{\Phi_{IF}}^s + T + A_{IF} + \varepsilon(\Phi_{IF})
\end{aligned} \tag{2.14}$$

where P_{IF} and Φ_{IF} represent the undifferenced dual-frequency ionosphere-free (IF) code and carrier-phase measurements (m), f_1 and f_2 represent the L1 and L2 frequencies, P_1 , P_2 and Φ_1 , Φ_2 are L1 and L2 code and phase measurements (in unit of meter) respectively, ρ is the geometric range between the receiver and satellite, c is the speed of light in the vacuum, $cdt_{P_{IF}}^s$ (satellite code clock error), $cdt_{\Phi_{IF}}^s$ (satellite phase clock error), $cdt_{P_{IF}}^r$ (receiver code clock error), and $cdt_{\Phi_{IF}}^r$ (receiver phase clock error) are functions of the actual satellite clock error dt^s , receiver clock error dt^r , satellite dual-frequency IF code and phase biases $b_{P_{IF}}^s$, $b_{\Phi_{IF}}^s$ and receiver dual-frequency IF code and phase biases $b_{P_{IF}}^r$, $b_{\Phi_{IF}}^r$. T is the tropospheric delay, $\varepsilon(P_{IF})$ and $\varepsilon(\Phi_{IF})$ are the noise including multipath of dual-frequency IF code and carrier-phase measurements, A_{IF} represents the dual-frequency IF ambiguities (in the unit of meter), which can be given as

$$A_{IF} = \frac{f_1^2 \lambda_1 N_1 - f_2^2 \lambda_2 N_2}{f_1^2 - f_2^2} = \lambda_{NL} N_1 + \frac{f_2}{f_1 + f_2} \lambda_{WL} N_{WL} \quad (2.15)$$

where N_1 and N_2 are the integer ambiguities of L1 and L2 frequencies, N_{WL} is the wide-lane integer ambiguity formed by N_1 and N_2 , λ_{NL} and λ_{WL} represent the narrow-lane (NL) and wide-lane (WL) wavelength formed by L1 and L2.

In PPP float solution estimation, the satellite code clock error ($cdt_{P_{IF}}^s$) is provided by IGS precise clock products, and the receiver position, tropospheric delay, receiver code clock $cdt_{P_{IF}}^r$, together with the float ambiguities are estimated. The precise satellite phase clock ($cdt_{\Phi_{IF}}^s$) is not used in float PPP. If only one receiver clock is estimated, the differences between the receiver code and phase biases, together with the satellite code and phase bias difference are absorbed into float ambiguities,

The carrier-phase observation can be rewritten as

$$\begin{aligned} \Phi_{IF} &= \rho + (cdt^r + b_{\Phi_{IF}}^r) - (cdt^s + b_{\Phi_{IF}}^s) + T + \lambda_{IF} N_{IF} + \varepsilon(\Phi_{IF}) \\ &= \rho + (cdt^r + b_{P_{IF}}^r - b_{P_{IF}}^r + b_{\Phi_{IF}}^r) - (cdt^s + b_{P_{IF}}^s - b_{P_{IF}}^s + b_{\Phi_{IF}}^s) \\ &\quad + T + A_{IF} + \varepsilon(\Phi_{IF}) \\ &= \rho + cdt_{P_{IF}}^r - cdt_{P_{IF}}^s + T + A'_{IF} + \varepsilon(\Phi_{IF}) \\ A'_{IF} &= \lambda_{IF} N_{IF} + (b_{\Phi_{IF}}^r - b_{P_{IF}}^r) - (b_{\Phi_{IF}}^s - b_{P_{IF}}^s) \end{aligned} \quad (2.16)$$

where A'_{IF} is the float ambiguities (in unit of meter). It can be seen that the IF float ambiguities cannot be decomposed as the combination of wide-lane and N_1 ambiguities as in Eq (2.15), due to the absorbed biases namely $(b_{\Phi_{IF}}^r - b_{P_{IF}}^r) - (b_{\Phi_{IF}}^s - b_{P_{IF}}^s)$.

2.1.3 PPP Fixed Solution

The main disadvantage of PPP float solution is that it needs significant time to reach convergence. If the PPP ambiguities can be fixed, the solution could get converged immediately after ambiguity resolution. PPP ambiguity resolution (AR) can also potentially improve the positioning accuracy

and the system reliability. Since the biases of satellites and receivers are absorbed into the float ambiguities, the PPP ambiguities are no longer integers anymore. PPP AR has to recover the integer property of the ambiguities to achieve the PPP fixed solution. Currently, there are three widely applied methods to obtain integer PPP ambiguities, namely uncalibrated phase delay method (Ge et al., 2007), the integer phase clock method (Laurichesse, D., Mercier, 2007) and decoupled clock model (Collins, 2008). All the methods aim to recover the integer property of ambiguities since the biases cannot be eliminated without double differencing in PPP.

It can be seen from Eq (2.15) and Eq (2.16) that the IF ambiguities can be decomposed as wide-lane ambiguities and N_I if the biases absorbed in the IF float ambiguities can be eliminated. To eliminate the biases absorbed into the IF ambiguities, Ge et al. (2008) proposed the single-difference between-satellite method in which the receiver biases are eliminated by single-difference while the satellite biases are estimated by a network. The estimated biases are then broadcasted to users to correct the raw measurements. In this way, the IF ambiguities contain no biases anymore. Besides, Collins (2008) and Laurichesse et al. (2009) also proposed decoupled clock and integer phase clock model respectively. In both methods, the precise satellite phase clock ($cdt_{\Phi_{IF}}^s$) is estimated using different methods through a global network. With the provided the precise satellite phase clock ($cdt_{\Phi_{IF}}^s$), the biases in the float IF ambiguities can be removed. Shi and Gao (2014) compared these three main PPP ambiguity resolution methods and concluded the mathematical equivalence of them. This thesis does not aim to generate the precise products at the server end. Therefore, only the implementation of PPP ambiguity resolution at the user end is presented. As an analysis center of IGS, Center National d'Etudes Spatiales (CNES) provides

regular precise phase clock products for users worldwide. In this thesis, the PPP AR method using the integer clock product by CNES is implemented.

With the integer clock product provided by CNES, the satellite phase clock error is available, which means that the IF code and phase observation model in Eq (2.16) can be formed and the IF ambiguities can be resolved by N_I and N_{WL} as shown in Eq (2.15). N_I can be called as NL ambiguities as well since the coefficient for N_I is the NL wavelength. In order to avoid setting two receiver clocks (code and phase) in implementation as indicated in Eq (2.14), single-difference between-satellite operator (Δ) can be applied to eliminate the receiver-related errors, given as

$$\begin{aligned}
\Delta P_{IF} &= \frac{f_1^2}{f_1^2 - f_2^2} \Delta P_1 - \frac{f_2^2}{f_1^2 - f_2^2} \Delta P_2 \\
&= \Delta \rho - \Delta c dt_{P_{IF}}^s + \Delta T + \varepsilon(P_{IF}) \\
\Delta \Phi_{IF} &= \frac{f_1^2}{f_1^2 - f_2^2} \Delta \Phi_1 - \frac{f_2^2}{f_1^2 - f_2^2} \Delta \Phi_2 \\
&= \Delta \rho - \Delta c dt_{\Phi_{IF}}^s + \Delta T + \Delta A_{IF} + \varepsilon(\Phi_{IF})
\end{aligned} \tag{2.17}$$

The wide-lane ambiguity in Eq (2.15) can be obtained by forming the Melbourne-Wübbena (MW) combination, the corresponding single-difference between-satellite wide-lane ambiguity can be achieved as follows.

$$\begin{aligned}
\Delta A_{MW} &= \Delta \Phi_{WL} - \Delta P_{NL} \\
&= -\lambda_{WL} \Delta N_{WL} - \Delta b_{MW}^s + \varepsilon(\Delta A_{MW}) \\
\Delta N_{WL} &= -(\Delta A_{MW} + \Delta b_{MW}^s) / \lambda_{WL} \\
\Delta b_{MW}^s &= (\alpha_{WL} \Delta b_{\Phi_1}^s + \beta_{WL} \Delta b_{\Phi_2}^s) - (\alpha_{NL} \Delta b_{P_1}^s + \beta_{NL} \Delta b_{P_2}^s) \\
\alpha_{WL} &= \frac{f_1}{f_1 - f_2} \quad \beta_{WL} = -\frac{f_2}{f_1 - f_2} \\
\alpha_{NL} &= \frac{f_1}{f_1 + f_2} \quad \beta_{NL} = \frac{f_2}{f_1 + f_2}
\end{aligned} \tag{2.18}$$

It can be seen that if the wide-lane bias Δb_{MW}^s is available, the wide-lane integer ambiguity can be calculated. The wide-lane biases are also included in the precise satellite phase clock product provided by CNES. After solving the wide-lane ambiguities in Eq (2.18), with the IF ambiguities obtained by Eq (2.17), N_I can be fixed using Least-squares AMBIGUITY Decorrelation Adjustment (LAMBDA) method. According to Eq (2.15), the N_I ambiguities can be calculated as

$$\Delta \hat{N}_I = (\Delta \hat{A}_{IF} - \frac{f_2}{f_1 + f_2} \lambda_{WL} \Delta \tilde{N}_{WL}) / \lambda_{NL} \quad (2.19)$$

where $\Delta \hat{A}_{IF}$ is the IF ambiguities obtained by Eq (2.17) with covariance matrix $Q_{\hat{A}_I}$, \tilde{N}_{WL} is the fixed wide-lane ambiguities by Eq (2.18). Therefore, the variance-covariance matrix for N_I ambiguities can be given as

$$Q_{\hat{N}_I} = \frac{1}{\lambda_{NL}^2} Q_{\hat{A}_{IF}} \quad (2.20)$$

The N_I ambiguities by Eq (2.19) and their variance-covariance matrix by Eq (2.20) are the input of LAMBDA method. According to Teunissen (1997) and Geng & Bock (2013), the ambiguity search space would approximately be inverse to the carrier-phase wavelength, which means that the search space for N_I is relatively large and it takes time to fix the N_I in PPP AR.

2.2 Inertial Navigation System

INS is a dead-reckoning navigation system providing the current state (position, velocity and attitude) based on the previous states and current inertial measurements. IMU is the core component of INS consisting of three gyros and three accelerometers. The attitude of the system can be determined by the gyro measurements. The accelerometers can measure the acceleration in the body frame, which can be transformed to a specific frame based on the current attitude. With

the previous state and the acceleration, the velocity and translation within a specific frame can be generated. The mechanization is implemented in the local-level frame in this thesis. The mechanization involves multiple coordinate frames which are introduced first in Section 2.2.1. When INS is integrated with other systems, the INS error formulation needs to be derived, which is presented in Section 2.2.3.

2.2.1 Coordinate Frames and Transformation

The coordinate frames involve in the INS mechanization are Earth-Centered Inertial (ECI) frame, Earth-Centered Earth-Fixed frame (ECEF), local-level frame (LLF) and body frame.

Earth-Centered inertial frame (ECI or i-frame): the origin is the earth's center of mass. The X axis is pointing towards the mean vernal equinox, the Z axis is aligned with the earth's spin axis, and the Y axis is orthogonal to X and Z axes completing the right-handed coordinate system. ECI is not exactly inertial since the earth center of mass itself is accelerating as it travels in its orbit. ECI is assumed inertial without rotating and accelerating.

Earth-Centered Earth-Fixed frame (ECEF or e-frame): the origin is the earth's mass center with X axis pointing to the mean meridian of Greenwich, Z axis parallel to the mean spin axis of the earth, Y axis completing the right-handed coordinate system.

Local-Level frame (LLF or l-frame): it is a local geodetic frame with origin coinciding with the sensor center, X, Y and Z axes pointing towards the geodetic east, north and up respectively.

Body frame (b-frame): the origin is the center of IMU, X axis points towards the right of the carrier in which the IMU is installed, Y axis points towards the forward direction of the carrier and Z axis completes the right-handed coordinate system.

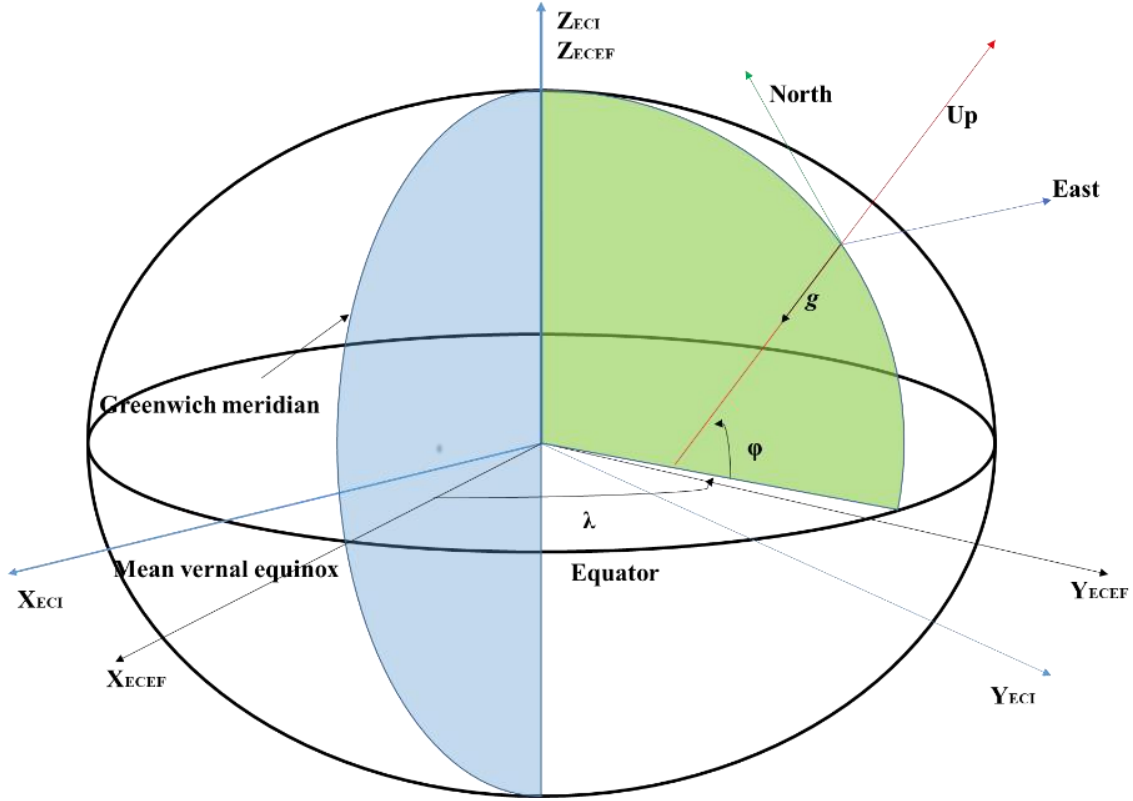


Figure 2.1 Coordinate Systems

The transformations between the body frame and the LLF are frequently used in the IMU mechanization, which is explained as follows.

With Euler angles describing the attitude, the transformation direction cosine matrices (DCM) transforming the vector in body frame to local-level frame can be denoted as

$$\begin{aligned}
 R_b^l &= (R_3(y))^T (R_1(p))^T (R_2(r))^T = \begin{bmatrix} \cos y & -\sin y & 0 \\ \sin y & \cos y & 0 \\ 0 & 0 & 1 \end{bmatrix} \begin{bmatrix} 1 & 0 & 0 \\ 0 & \cos p & -\sin p \\ 0 & \sin p & \cos p \end{bmatrix} \begin{bmatrix} \cos r & 0 & \sin r \\ 0 & 1 & 0 \\ -\sin r & 0 & \cos r \end{bmatrix} \\
 &= \begin{bmatrix} \cos y \cos r - \sin y \sin p \sin r & -\sin y \cos p & \cos y \sin r + \sin y \sin p \cos r \\ \sin y \cos r + \cos y \sin p \sin r & \cos y \cos p & \sin y \sin r - \cos y \sin p \cos r \\ -\cos p \sin r & \sin p & \cos p \cos r \end{bmatrix}
 \end{aligned} \tag{2.21}$$

where R_i ($i=1, 2, 3$) are elementary rotational matrices with respect to X, Y and Z axes respectively; b, l represent the body frame and LLF; r, p and y represent the roll, pitch and yaw respectively.

2.2.2 INS Mechanization

INS Mechanization is the process of converting the rotation rates and specific forces measured by the IMU into position, velocity and attitude. INS mechanization can be conducted in i-frame, e-frame or l-frame. In this study, the INS mechanization is carried out in l-frame.

The geodetic coordinates of the moving object are used to express the position, given as

$$r^l = [\varphi \quad \lambda \quad h]^T \quad (2.22)$$

where φ, λ, h are the latitude, longitude and ellipsoidal height respectively. The velocity is denoted in east, north and up as

$$V^l = [v_e \quad v_n \quad v_u]^T \quad (2.23)$$

The change rate of latitude, longitude and height can be denoted as

$$\begin{aligned} \dot{\varphi} &= \frac{v_n}{R_m + h} \\ \dot{\lambda} &= \frac{v_e}{(R_n + h)\cos\varphi} \\ \dot{h} &= v_u \end{aligned} \quad (2.24)$$

where R_m and R_n represent the meridian radius of curvature and the radius of curvature of the prime vertical respectively.

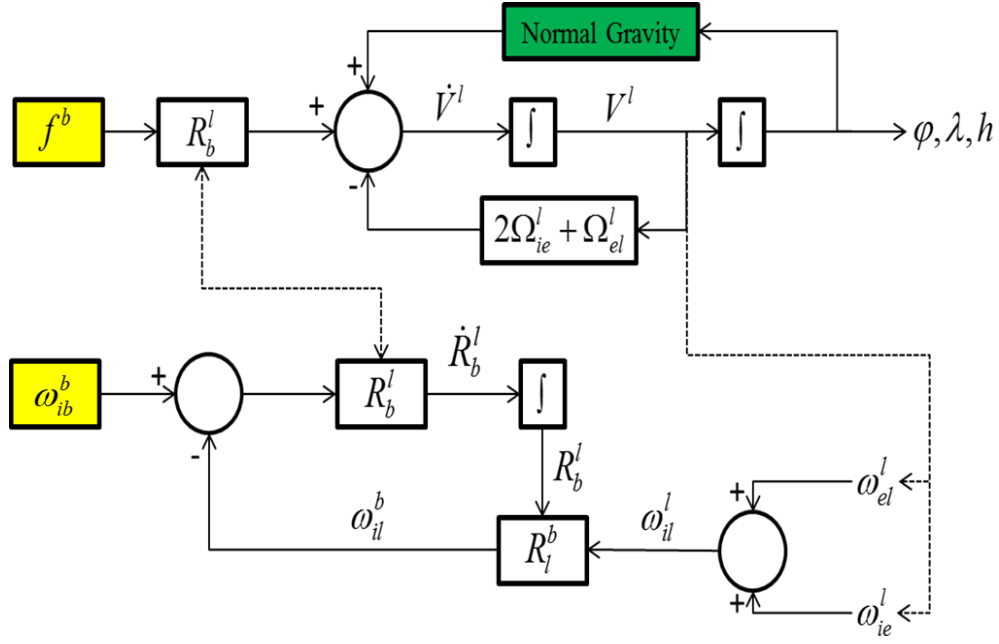


Figure 2.2 INS Mechanization (El-Sheimy, 2013)

The general procedure is shown in Figure 2.2. In the figure, Ω_{ib}^b is the skew-symmetric matrix of ω_{ib}^b namely the angular rate vector sensed by the gyroscope triad, ω_{ie}^l and ω_{el}^l are the earth rotation rate projected in the local-level frame and the transport rate caused by the orientation change of the local-level frame respectively, ω_{il}^l is the sum of the ω_{ie}^l and ω_{el}^l . It can be seen that to update the velocity and position, the specific forces measured by the accelerometers in the IMU body frame have to be first transformed to the local-level frame. The update of the rotation matrix from body frame to local-level frame can be given as

$$\dot{R}_b^l = R_b^l \Omega_{ib}^b = R_b^l (\Omega_{ib}^b - \Omega_{il}^b) \quad (2.25)$$

where dot represents the time derivatives, and the superscripts 'l' and 'b' represent the local-level frame and IMU body frame, R_b^l is the rotation matrix from body frame to the local-level frame matrix in Eq (2.21), Ω_{ab}^c is the skew-symmetric matrix of the rotation rate ω_{ab}^c , which represents the

rotation rate of frame ‘ b ’ relative to frame ‘ a ’ expressed in frame ‘ c ’. The Ω_{ib}^b is the gyro output of IMU while Ω_{il}^b can be given as

$$\Omega_{il}^b = (R_b^l)^T \Omega_{il}^l R_b^l = (R_b^l)^T (\Omega_{ie}^l + \Omega_{el}^l) R_b^l \quad (2.26)$$

It can be seen from Figure 2.2, Ω_{ie}^l and Ω_{el}^l can be obtained from the current position and velocity, given as

$$\begin{aligned} \omega_{ie}^l &= \begin{bmatrix} 0 \\ \omega^e \cos \varphi \\ \omega^e \sin \varphi \end{bmatrix} \rightarrow \Omega_{ie}^l = \begin{bmatrix} 0 & -\omega^e \sin \varphi & \omega^e \cos \varphi \\ \omega^e \sin \varphi & 0 & 0 \\ -\omega^e \cos \varphi & 0 & 0 \end{bmatrix} \\ \omega_{el}^l &= \begin{bmatrix} -\frac{v_n}{R_m + h} \\ \frac{v_e}{R_n + h} \\ \frac{v_e \tan \varphi}{R_n + h} \end{bmatrix} \rightarrow \Omega_{el}^l = \begin{bmatrix} 0 & -\frac{v_e \tan \varphi}{R_n + h} & \frac{v_e}{R_n + h} \\ -\frac{v_e \tan \varphi}{R_n + h} & 0 & \frac{v_n}{R_m + h} \\ -\frac{v_e}{R_n + h} & -\frac{v_n}{R_m + h} & 0 \end{bmatrix} \end{aligned} \quad (2.27)$$

where ω^e is the earth rotation rate. After updating the rotation matrix, the specific forces can be transformed into the local-level frame. However, the transformed specific forces cannot be applied directly to calculate the acceleration. The Coriolis force of earth rotation ($2\Omega_{ie}^e V^l$) and the influence caused by the orientation change of the local-level frame ($\Omega_{el}^e V^l$) need to be removed from the transformed specific forces. Besides, the normal gravity has to be taken into consideration as well. Therefore, the acceleration in local-level frame can be given as

$$\dot{V}^l = R_b^l f^b - (2\Omega_{ie}^l + \Omega_{el}^l) V^l + g^l \quad (2.28)$$

where f^b is the specific forces measured by IMU in its body frame, g^l is the normal gravity in the local-level frame. Combining Eq (2.22) ~ (2.28), the mechanization process can be summarized as

$$\begin{bmatrix} \dot{r}^l \\ \dot{V}^l \\ \dot{R}_b^l \end{bmatrix} = \begin{bmatrix} D^{-1}V^l \\ R_b^l f^b - (2\Omega_{ie}^l + \Omega_{el}^l)V^l + g^l \\ R_b^l(\Omega_{ib}^b - \Omega_{il}^b) \end{bmatrix} \quad (2.29)$$

where D^{-1} is the relationship between the position rate and the velocity in LLF, which is shown in the Appendix A.

2.2.3 INS Error Formulation

It is necessary to know the error accumulation with time in INS. Error-state Kalman filter is widely applied to mitigate the quick drift of INS when integrated with other systems. The INS errors need to be estimated in the integration with other systems to improve the overall performance. The INS errors can be derived from the mechanization process in Eq (2.29).

Eq (2.29) can be linearized to achieve the dynamic information of the system errors (Noureldin et al., 2013), given as

$$\begin{bmatrix} \delta \dot{r}^l \\ \delta \dot{V}^l \\ \dot{\varepsilon}^l \\ \delta \dot{f}^b \\ \delta \dot{\omega}^b \end{bmatrix} = F^l \begin{bmatrix} \delta r^l \\ \delta V^l \\ \varepsilon^l \\ \delta f^b \\ \delta \omega^b \end{bmatrix} + G \cdot w = \begin{bmatrix} F_{rr} & F_{rV} & 0_{3 \times 3} & 0_{3 \times 3} & 0_{3 \times 3} \\ F_{Vr} & F_{VV} & F_{V\varepsilon} & R_b^l & 0_{3 \times 3} \\ F_{\varepsilon r} & F_{\varepsilon V} & F_{\varepsilon\varepsilon} & 0_{3 \times 3} & R_b^l \\ 0_{3 \times 3} & 0_{3 \times 3} & 0_{3 \times 3} & -\alpha & 0_{3 \times 3} \\ 0_{3 \times 3} & 0_{3 \times 3} & 0_{3 \times 3} & 0_{3 \times 3} & -\beta \end{bmatrix} \cdot \begin{bmatrix} \delta r^l \\ \delta V^l \\ \varepsilon^l \\ \delta f^b \\ \delta \omega^b \end{bmatrix} + G \cdot w \quad (2.30)$$

where δ represents the error of corresponding parameters; ε^l represents the attitude error in the local-level frame, namely pitch, roll and yaw errors; δf^b and $\delta \omega^b$ are the accelerometer and gyro biases. After removing the deterministic parts of the inertial sensor biases, it is common to model the residual stochastic part as a first-order Gauss-Markov process. In the above equation, α and β are 3×3 matrices representing the reciprocal of the correlation time of the accelerometer and gyro biases respectively, G is the shaping matrix and w represents the driving white noise for the state

vector. The submatrices in Eq (2.30) are presented in Appendix A. In this thesis, the scale factors are not estimated in the state vector since it would not improve the accuracy too much with MEMS IMU applied.

2.3 Stereo Visual Odometry

VO is another widely applied dead-reckoning system using the continuously tracked (or matched) features on consecutive images with cameras. Based on the geometry change of static objects and perspective center, the motion of the optical center between two epochs can be calculated by the feature pixel coordinate variation on consecutive images. The accumulation of the motion between consecutive epochs generates the motion with respect to the beginning. In this thesis, pin-hole camera model is adopted, which is illustrated in the figure below. The projection of object P is the intersection of the beam from P to the optical center and the image plane.

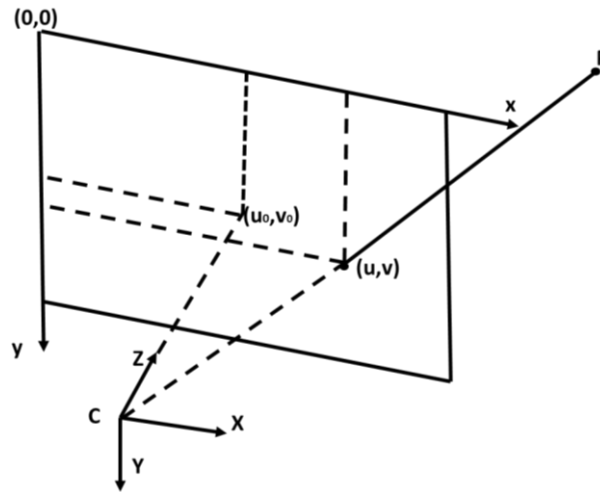


Figure 2.3 Camera Pin-hole Model

Similar to INS, the Stereo VO implementation involves transformation between different coordinate frames, which is introduced in section 2.3.1. Then, the implementation procedures are illustrated in section 2.3.2

2.3.1 Coordinate Frames and Camera Modeling

Image frame: the origin of the image frame is defined as the left-up corner of the image. The X axis and Y axis point to the right and down directions of the image respectively.

Camera frame: the origin of camera frame is the perspective center C of the camera, as in the figure above. The X and Y axes are parallel to the X and Y axes of image frame. The Z axis points to the forward direction of the camera to complet the right-handed coordinate system. The projection of perspective center on the image is called the principal point.

World frame: it is defined as the camera frame at the first epoch in this thesis.

The pixel coordinate (u, v) of a point (X_c, Y_c, Z_c) in camera frame can be given as

$$\begin{bmatrix} x \\ y \\ z \end{bmatrix} = \begin{bmatrix} f_x & 0 & u_0 \\ 0 & f_y & v_0 \\ 0 & 0 & 1 \end{bmatrix} \begin{bmatrix} X_c \\ Y_c \\ Z_c \end{bmatrix} \quad \begin{bmatrix} u \\ v \end{bmatrix} = \begin{bmatrix} x / z \\ y / z \end{bmatrix} \quad (2.31)$$

f_x, f_y are the focal length of each image axis, (u_0, v_0) is the coordinate of the principal point on the image, (u, v) is the pixel coordinate of a feature projected on the image.

For a point denoted in the world frame, it needs to be first transformed to the current camera frame in order to form the Eq (2.31). The transformation of the coordinates in the world frame to the current camera frame can be expressed as

$$\begin{bmatrix} X_c & Y_c & Z_c \end{bmatrix}^T = \begin{bmatrix} R_{3 \times 3} & t_{3 \times 1} \end{bmatrix} \begin{bmatrix} X_w & Y_w & Z_w & 1 \end{bmatrix}^T \quad (2.32)$$

where (X_w, Y_w, Z_w) is the point coordinate in the world frame, $R_{3 \times 3}$ and $t_{3 \times 1}$ are the rotation matrix and translation matrix which transform the coordinate in the world frame to the current camera frame. $R_{3 \times 3}$ and $t_{3 \times 1}$ can be obtained by accumulation of the estimated rotation and translation between consecutive epochs in VO.

As shown in Figure 2.3, with the image coordinates on one image, it is impossible to determine the object position in the camera frame. Only the orientation information is known with a monocular camera because the object could lie on any positioning along the ray. However, if stereo cameras are applied, the object coordinates in camera frame can be determined by triangulation of two rays, as shown in Figure 2.4.

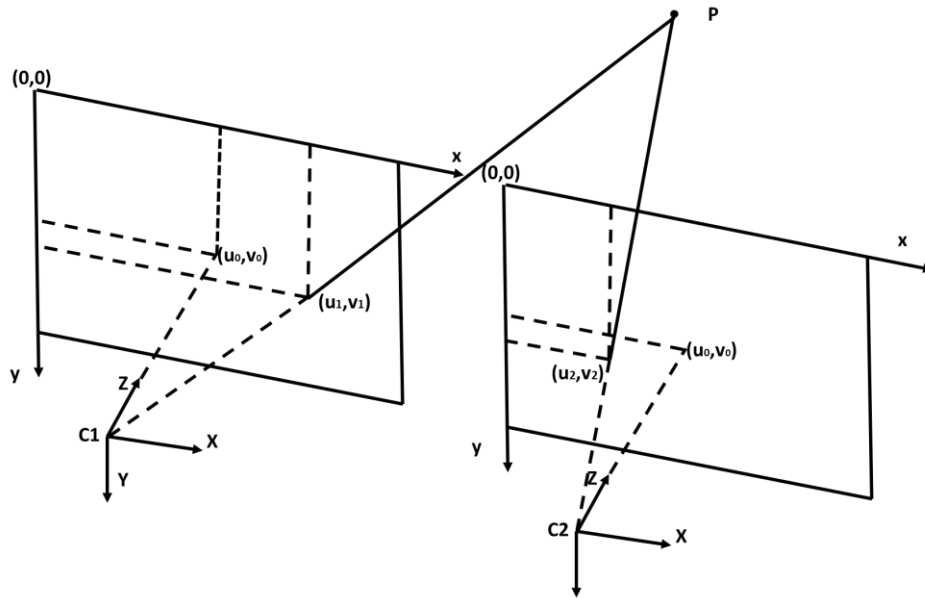


Figure 2.4 Projection of Stereo Cameras

The depth ambiguity can be eliminated by the intersection of two rays from the left and right perspective centers. As shown in Figure 2.4, the line C1-C2 is parallel with the X axis and two image plane coincides when two images are rectified. The projection on the left and right image can be rewritten as

$$\begin{aligned}
\begin{bmatrix} x_1 \\ y_1 \\ z_1 \end{bmatrix} &= \begin{bmatrix} f_x & 0 & u_0 & 0 \\ 0 & f_y & v_0 & 0 \\ 0 & 0 & 1 & 0 \end{bmatrix} \begin{bmatrix} X_c \\ Y_c \\ Z_c \end{bmatrix} \rightarrow \begin{bmatrix} u_1 \\ v_1 \end{bmatrix} = \begin{bmatrix} x_1 / z_1 \\ y_1 / z_1 \end{bmatrix} \\
\begin{bmatrix} x_2 \\ y_2 \\ z_2 \end{bmatrix} &= \begin{bmatrix} f_x & 0 & u_0 & -Bf_x \\ 0 & f_y & v_0 & 0 \\ 0 & 0 & 1 & 0 \end{bmatrix} \begin{bmatrix} X_c \\ Y_c \\ Z_c \\ 1 \end{bmatrix} \rightarrow \begin{bmatrix} u_2 \\ v_2 \end{bmatrix} = \begin{bmatrix} x_2 / z_2 \\ y_2 / z_2 \end{bmatrix}
\end{aligned} \tag{2.33}$$

where (X_c, Y_c, Z_c) is the point coordinate in the left camera frame; B is the baseline length between the two perspective centers C1 and C2.

2.3.2 Stereo VO Steps

When stereo cameras are rigidly mounted on a platform, the coordinates of the platform in the world frame can be calculated using Stereo VO algorithms. After having captured the image sequences, the Stereo VO implementation procedures can be divided into three main steps namely feature detection and tracking (or matching), motion estimation and local optimization.

2.3.2.1 Feature Detection and Tracking (Matching)

Feature detection and tracking (or matching) methods have been proposed by many researchers (Bay, Tuytelaars, & Van Gool, 2006; David G Lowe, 2004; Lucas & Kanade, 1981; Rosten & Drummond, 2006; Jianbo Shi, 1994; Carlo Tomasi & Kanade, 1991). Generally, the methods can be divided into two main categories. In the first category, optical flow algorithm is applied to track the features without descriptors. For example, Harris corner (Harris & Stephens, 1988) can be used to detect the corners or edges, and Kanada-Lucas-Tomasi (KLT) tracker (Lucas & Kanade, 1981; Shi, 1994; Tomasi & Kanade, 1991) can track the detected features based on optical-flow algorithms. The other category assigns a descriptor for each detected feature, based on which the features can be matched in subsequent images. Scale-Invariant Feature Transform (SIFT) (Lowe,

2004), Speeded-Up Robust Feature (SURF) (Bay et al., 2006) and Features from Accelerated Segment Test (FAST) (Rosten & Drummond, 2006) are widely used methods with a descriptor. Different methods have their own advantages and disadvantages. For instance, SIFT is accurate, stable and robust to scale and rotational variance. However, the processing speed of SIFT is too slow for visual odometry. Since feature detection and tracking (or matching) is not the focus of this thesis, only the KLT tracking method is introduced here.

According to Baker & Matthews (2004), the goal of the KLT algorithm is to minimize the sum of squared errors between two images, given as

$$\min_x \sum [I(W(x; p)) - T(x)]^2 \quad (2.34)$$

where x represents the image coordinates of features (u, v) ; $I(x)$ is the input image namely the image at current epoch; $T(x)$ is the template image namely the image at the previous epoch; $W(x; p)$ denotes the parameterized set of allowed warps where $p=(p_1, \dots, p_n)^T$ is the parameter vector. $W(x; p)$ varies with different displacement models. Some examples are given in Table 2.2.

Table 2.3 Warp Functions between Consecutive Images

Translation	Rigid	Affine
$x' = x + b_1$ $y' = y + b_2$ $W(x; p) = (x + b_1, y + b_2)$	$x' = x \cos \theta - y \sin \theta + b_1$ $y' = x \sin \theta + y \cos \theta + b_2$ $W(x; p) = (x \cos \theta - y \sin \theta + b_1, x \sin \theta + y \cos \theta + b_2)$	$x' = a_1 x + a_2 y + b_1$ $y' = a_3 x + a_4 y + b_2$ $W(x; p) = (a_1 x + a_2 y + b_1, a_3 x + a_4 y + b_2)$
$W(x; p) = \begin{bmatrix} 1 & 0 & b_1 \\ 0 & 1 & b_2 \end{bmatrix} \begin{bmatrix} x \\ y \\ 1 \end{bmatrix}$	$W(x; p) = \begin{bmatrix} \cos \theta & -\sin \theta & b_1 \\ \sin \theta & \cos \theta & b_2 \end{bmatrix} \begin{bmatrix} x \\ y \\ 1 \end{bmatrix}$	$W(x; p) = \begin{bmatrix} a_1 & a_2 & b_1 \\ a_3 & a_4 & b_2 \end{bmatrix} \begin{bmatrix} x \\ y \\ 1 \end{bmatrix}$

Eq (2.34) needs be linearized at an initially estimated p_0 , and the correction for p_0 can be iteratively solved using the equation below

$$\min \sum_x [I(W(x; p_0 + dp)) - T(x)]^2 = \min \sum_x \left[I(W(x; p_0)) + \nabla I \frac{\partial W}{\partial p} dp - T(x) \right]^2 \quad (2.35)$$

where ∇I is the gradient of the image I evaluated at $W(x; p_0)$; $\partial W / \partial p$ is the Jacobian of the warp, which can be achieved by calculating the derivatives of the $W(x; p)$ with respect to the parameters in Table 2.2. Eq (2.35) means to seek for a Least-Square solution of dp , which can be given as

$$dp = H^{-1} \sum_x \left[\nabla I \frac{\partial W}{\partial p} \right]^T [T(x) - I(W(x; p_0))] \quad (2.36)$$

where H is the Hessian matrix, which can be given as

$$H = \sum_x \left[\nabla I \frac{\partial W}{\partial p} \right]^T \left[\nabla I \frac{\partial W}{\partial p} \right] \quad (2.37)$$

Eq (2.34) ~ (2.37) can be repeated using the latest estimated p for better linearization until the dp is less than a threshold. Then p can be updated based on the previous p_0 and the estimated dp as $p = p_0 + dp$.

2.3.2.2 Motion Estimation

After having found correspondences in consecutive epochs, the optimal ego-motion estimation can be achieved by minimizing the re-projection errors of the tracked features. The procedure is introduced in the following. Since stereo cameras are used, as illustrated before, with correspondences in stereo images, the feature coordinates in camera frame can be obtained by triangulation, which can be simplified as

$$\begin{bmatrix} X_c \\ Y_c \\ Z_c \end{bmatrix} = \begin{bmatrix} (u_1 - u_0)B / (u_1 - u_2) \\ (v_1 - v_0)B / (u_1 - u_2) \\ fB / (u_1 - u_2) \end{bmatrix} \quad (2.38)$$

where the parameters are the same as in Eq (2.33). Using Eq (2.38), the feature coordinates in the previous camera frame can be obtained. The ego-motion of the cameras can be estimated based on the 3D feature coordinates in the previous camera frame and the tracked feature pixel coordinates in the current image frame, which is called resectioning in Stereo VO. In resectioning, the rotation and translation of the camera need to be estimated. With the rotation and translation, the 3D feature coordinates in the previous camera frame can be transformed to the current camera frame, and the features can be re-projected on the current image frame. The three Euler angles and the translation vector to be estimated are set as α , β , γ and t_x , t_y , t_z . By combining Eq (2.31) ~ (2.38), the re-projection of the tracked (or matched) features on the current image can be given as

$$\begin{aligned} u &= f_x \frac{X_{current}}{Z_{current}} + u_0 \\ v &= f_y \frac{Y_{current}}{Z_{current}} + v_0 \end{aligned} \quad (2.39)$$

$$\begin{bmatrix} X_{current} \\ Y_{current} \\ Z_{current} \end{bmatrix} = R(\alpha, \beta, \gamma) \begin{bmatrix} X_{previous} \\ Y_{previous} \\ Z_{previous} \end{bmatrix} + \begin{bmatrix} t_x \\ t_y \\ t_z \end{bmatrix}$$

where $[X_{previous}, Y_{previous}, Z_{previous}]^T$ is the feature coordinate vector in the previous camera frame obtained by triangulation; $[X_{current}, Y_{current}, Z_{current}]^T$ is the transformed feature coordinate in the current camera frame $R(\alpha, \beta, \gamma)$ is the rotation matrix from the previous camera frame to the current camera frame formed by three Euler angles, which can be given as

$$R(\alpha, \beta, \gamma) = \begin{bmatrix} \cos \beta \cos \gamma & -\cos \beta \sin \gamma & \sin \beta \\ \sin \alpha \sin \beta \cos \gamma + \cos \alpha \sin \gamma & -\sin \alpha \sin \beta \sin \gamma + \cos \alpha \cos \gamma & -\sin \alpha \cos \beta \\ -\cos \alpha \sin \beta \cos \gamma + \sin \alpha \sin \gamma & \cos \alpha \sin \beta \sin \gamma + \sin \alpha \cos \gamma & \cos \alpha \cos \beta \end{bmatrix} \quad (2.40)$$

When the current image pixel coordinates of the features are available, the rotation and translation can be estimated using least square by minimizing the re-projection errors of the features

$$\delta x = (H^T P H)^{-1} H^T P l \quad (2.41)$$

where δx is the correction vector estimated for the Euler angles and the translation vector, namely, $\delta x = [d\alpha \ d\beta \ d\gamma \ dt_x \ dt_y \ dt_z]^T$; P is the weight matrix of the measurements which can be set as identity matrix in this case; l is the misclosure vector and H is the design matrix, which can be expressed as

$$l = \begin{bmatrix} u_{m1} - u'_1 \\ v_{m1} - v'_1 \\ \vdots \\ u_{mn} - u'_n \\ v_{mn} - v'_n \end{bmatrix} \quad H = \begin{bmatrix} h_{u1} \\ h_{v1} \\ \vdots \\ h_{un} \\ h_{vn} \end{bmatrix} = \begin{bmatrix} h_{u\alpha 1} & h_{u\beta 1} & h_{u\gamma 1} & h_{utx1} & h_{uty1} & h_{utz1} \\ h_{v\alpha 1} & h_{v\beta 1} & h_{v\gamma 1} & h_{vtx1} & h_{vty1} & h_{vtz1} \\ \vdots & \vdots & \vdots & \vdots & \vdots & \vdots \\ h_{u\alpha n} & h_{u\beta n} & h_{u\gamma n} & h_{utxn} & h_{uty n} & h_{utzn} \\ h_{v\alpha n} & h_{v\beta n} & h_{v\gamma n} & h_{vtx n} & h_{vty n} & h_{vtzn} \end{bmatrix} \quad (2.42)$$

where (u_{mi}, v_{mi}) ($i=1, 2, \dots, n$) is the i^{th} measured pixel coordinate in current epoch; (u'_i, v'_i) ($i=1, 2, \dots, n$) is the i^{th} re-projection pixel coordinate based on the rotation and translation; $h_{u\alpha i}, h_{u\beta i}, h_{u\gamma i}, h_{utxi}, h_{utyi}, h_{utzi}$ are the elements of the design matrix of the i^{th} u_m with respect to the six unknowns respectively; $h_{v\alpha i}, h_{v\beta i}, h_{v\gamma i}, h_{vtxi}, h_{vtyi}, h_{vtzi}$ are the design matrix elements of the i^{th} v_m with respect to the six unknowns respectively. The design matrix elements h_{upi} ($p=\alpha, \beta, \gamma, t_x, t_y, t_z; i=1, 2, \dots, n$) can be derived as follows

$$\begin{aligned}
h_{uci} &= \frac{\partial u}{\partial X_{current}^i} \frac{\partial X_{current}^i}{\partial \alpha} + \frac{\partial u}{\partial Z_{current}^i} \frac{\partial Z_{current}^i}{\partial \alpha}; \\
h_{u\beta i} &= \frac{\partial u}{\partial X_{current}^i} \frac{\partial X_{current}^i}{\partial \beta} + \frac{\partial u}{\partial Z_{current}^i} \frac{\partial Z_{current}^i}{\partial \beta}; \\
h_{u\gamma i} &= \frac{\partial u}{\partial X_{current}^i} \frac{\partial X_{current}^i}{\partial \gamma} + \frac{\partial u}{\partial Z_{current}^i} \frac{\partial Z_{current}^i}{\partial \gamma}; \\
h_{utxi} &= \frac{\partial u}{\partial X_{current}^i} \frac{\partial X_{current}^i}{\partial t_x} + \frac{\partial u}{\partial Z_{current}^i} \frac{\partial Z_{current}^i}{\partial t_x}; \\
h_{utyi} &= \frac{\partial u}{\partial X_{current}^i} \frac{\partial X_{current}^i}{\partial t_y} + \frac{\partial u}{\partial Z_{current}^i} \frac{\partial Z_{current}^i}{\partial t_y}; \\
h_{utzi} &= \frac{\partial u}{\partial X_{current}^i} \frac{\partial X_{current}^i}{\partial t_z} + \frac{\partial u}{\partial Z_{current}^i} \frac{\partial Z_{current}^i}{\partial t_z};
\end{aligned} \tag{2.43}$$

where $X_{current}^i$ and $Z_{current}^i$ ($i=1, 2, \dots, n$) stand for the coordinates of the i^{th} transformed feature in X and Z components in the current camera frame using the initial values $\alpha_0, \beta_0, \gamma_0, t_{x0}, t_{y0}$ and t_{z0} ; the partial derivatives of u with respect to $X_{current}^i$ and $Z_{current}^i$ can be given as

$$\frac{\partial u}{\partial X_{current}^i} = \frac{f_x}{Z_{current}^i} \quad \frac{\partial u}{\partial Z_{current}^i} = -\frac{X_{current}^i f_x}{(Z_{current}^i)^2} \tag{2.44}$$

and the partial derivatives of $X_{current}^i$ and $Z_{current}^i$ with respect to $\alpha, \beta, \gamma, t_x, t_y, t_z$ can be given as

$$\begin{aligned}
\frac{\partial X_{current}^i}{\partial \alpha} &= 0; \\
\frac{\partial Z_{current}^i}{\partial \alpha} &= (\sin \alpha_0 \sin \beta_0 \cos \gamma_0 + \cos \alpha_0 \sin \gamma_0) X_{previous}^i + (-\sin \alpha_0 \sin \beta_0 \sin \gamma_0 + \cos \alpha_0 \cos \gamma_0) Y_{previous}^i \\
&\quad + (-\sin \alpha_0 \cos \beta_0) Z_{previous}^i \\
\frac{\partial X_{current}^i}{\partial \beta} &= (-\sin \beta_0 \cos \gamma_0) X_{previous}^i + (\sin \beta_0 \sin \gamma_0) Y_{previous}^i + \cos \beta_0 Z_{previous}^i \\
\frac{\partial Z_{current}^i}{\partial \beta} &= (-\cos \alpha_0 \cos \beta_0 \cos \gamma_0) X_{previous}^i + (\cos \alpha_0 \cos \beta_0 \sin \gamma_0) Y_{previous}^i + (-\cos \alpha_0 \sin \beta_0) Z_{previous}^i
\end{aligned}$$

$$\begin{aligned}
\frac{\partial X_{current}^i}{\partial \gamma} &= (-\cos \beta_0 \sin \gamma_0) X_{previous}^i + (-\cos \beta_0 \cos \gamma_0) Y_{previous}^i \\
\frac{\partial Z_{current}^i}{\partial \gamma} &= (\cos \alpha_0 \cos \beta_0 \sin \gamma_0 + \sin \alpha_0 \cos \gamma_0) X_{previous}^i + (\cos \alpha_0 \sin \beta_0 \cos \gamma_0 - \sin \alpha_0 \sin \gamma_0) Y_{previous}^i \\
\frac{\partial X_{current}^i}{\partial t_x} &= 1; \frac{\partial X_{current}^i}{\partial t_y} = 0; \frac{\partial X_{current}^i}{\partial t_z} = 0; \\
\frac{\partial Z_{current}^i}{\partial t_x} &= 0; \frac{\partial Z_{current}^i}{\partial t_y} = 0; \frac{\partial Z_{current}^i}{\partial t_z} = 1;
\end{aligned} \tag{2.45}$$

where α_0, β_0 and γ_0 are the initial values of α, β and γ ; $X_{previous}^i, Y_{previous}^i$ and $Z_{previous}^i$ ($i=1, 2, \dots, n$) are the i^{th} feature coordinates in the previous camera frame obtained by triangulation. Similarly, the design matrix elements h_{vpi} ($p=\alpha, \beta, \gamma, t_x, t_y, t_z; i=1, 2, \dots, n$) in Eq (2.42) can be derived as follows

$$\begin{aligned}
h_{vai} &= \frac{\partial v}{\partial Y_{current}^i} \frac{\partial Y_{current}^i}{\partial \alpha} + \frac{\partial v}{\partial Z_{current}^i} \frac{\partial Z_{current}^i}{\partial \alpha}; \\
h_{v\beta i} &= \frac{\partial v}{\partial Y_{current}^i} \frac{\partial Y_{current}^i}{\partial \beta} + \frac{\partial v}{\partial Z_{current}^i} \frac{\partial Z_{current}^i}{\partial \beta}; \\
h_{v\gamma i} &= \frac{\partial v}{\partial Y_{current}^i} \frac{\partial Y_{current}^i}{\partial \gamma} + \frac{\partial v}{\partial Z_{current}^i} \frac{\partial Z_{current}^i}{\partial \gamma}; \\
h_{vtxi} &= \frac{\partial v}{\partial Y_{current}^i} \frac{\partial Y_{current}^i}{\partial t_x} + \frac{\partial v}{\partial Z_{current}^i} \frac{\partial Z_{current}^i}{\partial t_x}; \\
h_{vtyi} &= \frac{\partial v}{\partial Y_{current}^i} \frac{\partial Y_{current}^i}{\partial t_y} + \frac{\partial v}{\partial Z_{current}^i} \frac{\partial Z_{current}^i}{\partial t_y}; \\
h_{vtzi} &= \frac{\partial v}{\partial Y_{current}^i} \frac{\partial Y_{current}^i}{\partial t_z} + \frac{\partial v}{\partial Z_{current}^i} \frac{\partial Z_{current}^i}{\partial t_z};
\end{aligned} \tag{2.46}$$

where $Y_{current}^i$ and $Z_{current}^i$ ($i=1, 2, \dots, n$) stand for the i^{th} transformed feature coordinates in Y and Z components in the current camera frame; the partial derivatives of v with respect to $Y_{current}^i$ and $Z_{current}^i$ can be given as

$$\frac{\partial v}{\partial Y_{current}^i} = \frac{f_y}{Z_{current}^i} \quad \frac{\partial v}{\partial Z_{current}^i} = -\frac{X_{current}^i f_y}{(Z_{current}^i)^2} \quad (2.47)$$

and then the partial derivatives of $Y_{current}^i$ with respect to $\alpha, \beta, \gamma, t_x, t_y, t_z$ can be given as

$$\begin{aligned} \frac{\partial Y_{current}^i}{\partial \alpha} &= (\cos \alpha_0 \sin \beta_0 \cos \gamma_0 - \sin \alpha_0 \sin \gamma_0) X_{previous}^i + (-\cos \alpha_0 \sin \beta_0 \sin \gamma_0 - \sin \alpha_0 \cos \beta_0) Y_{previous}^i \\ &\quad + (-\cos \alpha_0 \cos \beta_0) Z_{previous}^i; \\ \frac{\partial Y_{current}^i}{\partial \beta} &= (\sin \alpha_0 \cos \beta_0 \cos \gamma_0) X_{previous}^i + (-\sin \alpha_0 \cos \beta_0 \sin \gamma_0) Y_{previous}^i + (\sin \alpha_0 \sin \beta_0) Z_{previous}^i; \\ \frac{\partial Y_{current}^i}{\partial \gamma} &= (-\sin \alpha_0 \sin \beta_0 \sin \gamma_0 + \cos \alpha_0 \cos \gamma_0) X_{previous}^i + (-\sin \alpha_0 \sin \beta_0 \cos \gamma_0 - \cos \alpha_0 \sin \gamma_0) Y_{previous}^i; \\ \frac{\partial Y_{current}^i}{\partial t_x} &= 0; \frac{\partial Y_{current}^i}{\partial t_y} = 1; \frac{\partial Z_{current}^i}{\partial t_z} = 0; \end{aligned} \quad (2.48)$$

The corrections of the rotation and translation parameters $d\alpha, d\beta, d\gamma, dt_x, dt_y$ and dt_z to the initial values $(\alpha_0, \beta_0, \gamma_0, t_{x0}, t_{y0}$ and $t_{z0})$ can be obtained using the Eq (2.38) ~ (2.48) iteratively until the corrections become less than a threshold. The final rotation and translation parameters can be achieved by adding their initial values and the corresponding corrections. The motion of the stereo cameras can be achieved by accumulating the rotation and translation obtained between consecutive epochs introduced above.

2.3.2.3 Local Optimization

It is inevitable that some features are incorrectly tracked (or matched) using the method introduced in Section 2.3.2.1, which would lead to inaccurate motion estimation. To remove the outliers, the RANdom SAMple Consensus (RANSAC) algorithm is usually used. The RANSAC implementation steps can be summarized as follows. Firstly, a certain number of the tracked (or matched) features are randomly selected to perform the resectioning illustrated in Section 2.3.2.2

to calculate the rotation and translation. Secondly, all the tracked (or matched) features are re-projected on the current image using the calculated rotation and translation in the first step. Thirdly, the number of inliers with the calculated rotation and translation is recorded. The re-projection error of a tracked point needs to be within a threshold. Fourthly, the above procedures with randomly selected features are repeated many times (e.g. 200 times) and the one with the maximum number of inliers is treated as the correction rotation and translation. Meanwhile, the outliers are filtered out. Finally, the rotation and translation are recalculated based on the inliers obtained.

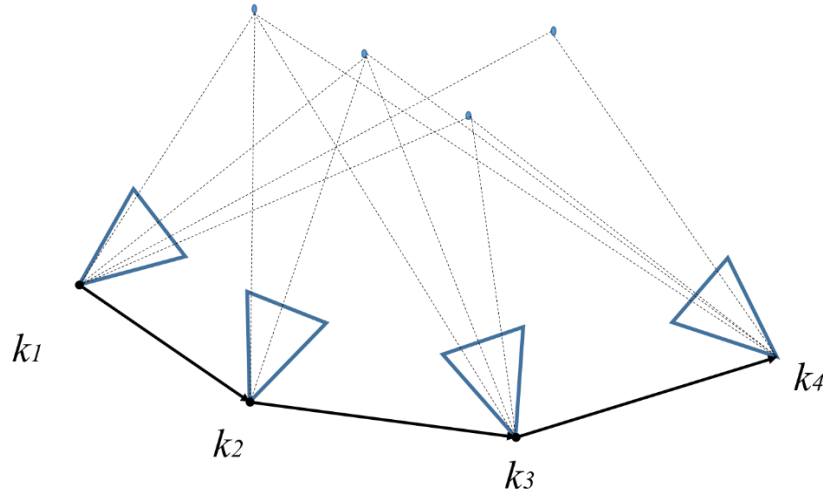


Figure 2.5 Image Sequence

After the application of RANSAC, relatively reliable rotation and translation from the previous camera frame to current camera frame can be achieved. The rotation and translation with respect to the first epoch can be obtained by the accumulation of the rotations and translations between two consecutive epochs. However, in this way, the solution drifts quickly because the ego-motion estimation between two consecutive epochs is independent of each other and there is no constraints among them. To solve this problem, many researchers apply windowed bundle adjustment to optimize the solution within several epochs.

As illustrated in Figure 2.5, the bundle adjustment is performed using multiple images with commonly tracked (or matched) features. Usually, the 3D coordinates of the used features are the triangulation results when the features are first detected and matched in stereo images because solution drifts with time and earlier obtained 3D coordinates are more reliable.

Chapter Three: DEVELOPMENT OF A TIGHT INTEGRATION SYSTEM FOR LAND VEHICLE NAVIGATION USING IMU, STEREO VO AND GNSS PPP

The fundamentals of PPP, INS and Stereo VO have been illustrated in the previous chapter. In this chapter, the multi-sensor integration strategy with IMU as the core sensor is introduced. Kalman filter is applied to fuse the inertial measurements with other types of aiding measurements. In general, the INS provides the dynamic information of the platform while the other systems are applied to correct the errors and optimize the solution.

3.1 Multi-sensor Integration with IMU as the Core Sensor

IMU is a self-contained sensor that can work in most circumstances, which makes it suitable to be applied as a core sensor in an integrated navigation system. When other types of measurements can be received, all the data are fused in an Extended Kalman filter (EKF). The Kalman filter deals with the linear system, which means that the non-linear integrated system model needs to be linearized. If the linearization is based on the states from the previous epoch, the filter is referred as an Extended Kalman filter (EKF). The EKF procedures after linearization can be summarized as

$$\begin{aligned} X_k^- &= \Phi_{k,k-1} X_{k-1} + w_{k-1} \\ P_k^- &= \Phi_{k,k-1} P_{k-1} \Phi_{k,k-1}^T + Q_{k-1} \\ K_k &= P_k^- H_k^T (H_k P_k^- H_k^T + R_k)^{-1} \\ X_k &= X_k^- + K_k (Z_k - H_k X_{k-1}^-) \\ P_k &= (I - K_k H_k) P_k^- \end{aligned} \tag{3.1}$$

where the subscripts k and $k-1$ represent the current epoch and the previous epoch; X_k is the prior state vector; w_{k-1} is the process noise vector; P_k is the predicted matrix of the estimation covariance of the state vector; $\Phi_{k,k-1}$ is the transition matrix; Q_{k-1} is the covariance matrix of the process noise; K_k is the gain matrix; H_k is the design matrix; R_k is the covariance matrix of the measurements;

Z_k is the measurement vector; I is the identity matrix; X_k is the posterior state vector; P_k is the corrected matrix of the estimation covariance of the state vector;.

In this thesis, the errors of the current kinematic states are estimated in the state vector, given as

$$X_{INS} = [\delta r^l \quad \delta V^l \quad \varepsilon^l \quad \delta f^b \quad \delta \omega^b]^T \quad (3.2)$$

where X_{INS} is the state vector related to the INS mechanization errors, δr^l is error of geodetic coordinates, δV^l , ε^l are the velocity and attitude errors in LLF, δf^b and $\delta \omega^b$ are the accelerometer and gyro biases in the body frame.

Generally, there are three main integration strategies namely loose integration, tight integration and deep integration. The integration level of three methods is updated from loose integration to deep integration. Loose integration is the easiest to be implemented since it requires each system can work independently and only the outputs of each system are fused to achieve the optimal results. The tight integration is conducted at measurement level while the deep integration is at the hardware level. The deep integration is normally implemented by the equipment manufacturers (e.g. receiver for signal tracking), which is not discussed in this thesis.

3.1.1 Loose Integration

In loose integration, each system operates independently to estimate the position, velocity or attitude. The position, velocity or attitude solutions estimated from INS and other systems (e.g. GNSS, VO) are fused in a filter to output the integration solution and correct the inertial errors. The general processing procedures are illustrated in Figure 3.1. It can be seen in the figure that the estimated errors using the filter are used to compensate for the INS mechanization results, which is referred as closed-loop approach. The closed-loop approach is usually adopted for low-cost

MEMS IMU, of which the mechanization errors accumulate rapidly. In contrast to the closed-loop approach, in open loop approach, the INS mechanization operates without any feedback from the integration filter. Applications using navigation grade IMUs can adopt the open-loop approach because of small error propagation.

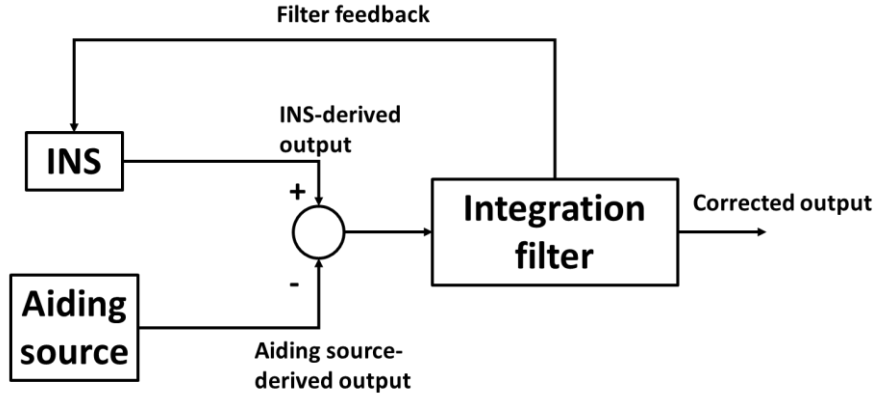


Figure 3.1 Scheme of Closed-Loop Loose Integration

According to the loose integration scheme, the dynamic matrix in the filter keeps the same as shown in Eq (3.2) while the measurements are the differences between the INS solution and the aiding source derived solution. With small time interval between two consecutive epochs, the transition matrix can be approximated as

$$\Phi_{k,k-1} = e^{F\Delta t} \approx I + F\Delta t \quad (3.3)$$

where I is the identity matrix; F is the dynamic matrix; Δt is the time interval between two consecutive epochs.

The loosely coupled integration is easier to be implemented because of smaller dimension of the state vector and simpler scheme, compared to tightly coupled integration. However, it requires independent operation of each individual system. If the aiding sources fail to provide the

continuous solution in harsh environments, the performance of the integrated system degrades greatly.

3.1.2 Tight Integration

The difference between the loosely coupled and the tightly coupled integration is that the solutions of different systems are fused in the loose integration while the raw measurements are applied in the tight integration directly. The tight integration is achieved at a deeper level and more complicated using a centralized integration filter. However, the tight integration has its own advantages. All the information can be fully applied in the tight integration, and better outlier detection is possible in the tight integration.

Within the tight integration architecture, the raw measurements from the aiding sources (e.g. code, carrier-phase and Doppler measurements from GNSS) are directly processed in an integration filter, as shown in Figure 3.2. Different from the loose integration, the inputs of the integration filter are the INS-derived aiding source measurements and the raw measurements of the aiding source instead of the direct navigation solutions.

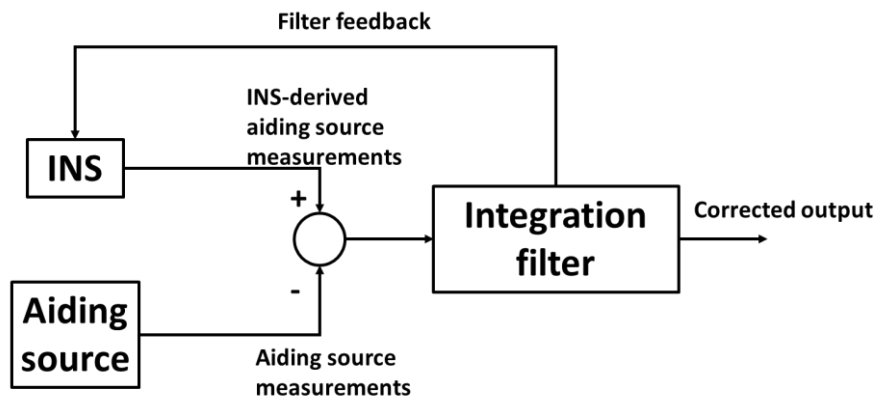


Figure 3.2 Scheme of Closed-Loop Tight Integration

The integration filter directly processes the measurement differences of different sensors and outputs the estimated errors. Similar to the loosely coupled integration, the tightly coupled integration can be implemented in both open-loop and closed-loop approaches as well. The corrected solution can be obtained by correcting the initial INS mechanization results with the estimated errors in closed-loop approach.

When integrated with external sensors, external measurement related unknowns have to be included in the state vector if necessary. For instance, the receiver clock error or clock drift has to be estimated if GNSS raw measurements are used. If PPP algorithm is used, the phase ambiguities and troposphere delay need to be included as well. The extended state vector can be denoted as

$$X_k = [X_{INS} \quad X_{external}]^T \quad (3.4)$$

where X_k is the state vector in Eq (3.1); $X_{external}$ is the augmented parameters for the measurements from the aiding sources. The dynamic matrix of the INS mechanization is provided in Eq (2.29). The extension of the dynamic matrix with external sensor related elements in state vector can be given as

$$F = \begin{bmatrix} F^I & 0 \\ 0 & F_{external} \end{bmatrix} \quad (3.5)$$

where F^I is the dynamic matrix in Eq (2.30); $F_{external}$ is the dynamic matrix for the augmented parameters. As shown in Figure 3.2, the measurements of Kalman filter are the differences between the external measurements and the INS-derived measurements. Therefore, the measurements Z_k is

$$Z_k = [Z_{derived} - Z_{measured}] \quad (3.6)$$

where $Z_{derived}$ is the INS-derived measurement vector while $Z_{measured}$ is the external measurement vector. The INS-derived measurement vector is calculated based on the kinematic state (e.g.

position, velocity and attitude) obtained from the mechanization results in current epoch using Eq (2.29). $F_{external}$, H_k , and R matrices are based on the external measurements applied, which will be specified in the following part of this chapter.

In this thesis, the tight integration with IMU as the core sensor while GNSS and Stereo VO as aiding sources is investigated. Kalman filter is adopted as the integration filter to fuse different types of datasets. The core sensor IMU provides the dynamic information of the platform. When either GNSS or visual measurements are available, different types of measurements are fused in the Kalman filter to obtain the optimized solution. For GNSS, the pseudorange, carrier-phase and Doppler measurements are applied, and for Stereo VO, the pixel coordinates on the stereo images are utilized in a centralized Kalman filter. The derivation of how pixel coordinates can be used to integrate with INS using Kalman filter is illustrated in this chapter. If GNSS is not available, the tight integration of INS and Stereo VO utilizes both the INS and Stereo VO information, which limits the quick drift of stand-alone IMU and outperforms the stand-alone VO. The tightly coupled integration INS/ Stereo VO and GNSS/INS/Stereo VO are introduced in Section 3.2 and Section 3.3 respectively.

In this work, multi-sensor tight integration is implemented. Since the IMU data is available in most circumstances, IMU could be applied as the core sensor in the integration with other types of sensors. The other types of measurements are applied to update the filter when available. Corresponding elements in the state vector and dynamic matrix have to be extended if necessary when new types of measurements are used. In this work, error-state and error-measurement Kalman filter is applied to estimate the errors. IMU could provide not only position and velocity but also the attitude. Therefore, almost all the other types of measurements from other sensors can

be predicted based on the mechanization of the IMU. Then the difference between the predicted and measured measurements can be used to estimate the errors in the state vector in Kalman filter. In this way, the IMU can output solution all the time and other sensors are used to correct the accumulated errors when available.

3.2 Tight Integration of INS and Stereo VO

GNSS signals can be easily blocked or interfered, which limits the application of GNSS in certain circumstances. As mentioned in Chapter 2, the INS and VO are both self-contained dead-reckoning systems, which can be applied to bridge the GNSS outage. However, dead-reckoning systems suffer inevitable drift over time because of error accumulation without absolute positioning information. The integration of INS and VO still cannot avoid error accumulation, but it can greatly improve the results by restricting the quick drift of each individual system. In this section, the tight integration of INS and Stereo VO is illustrated.

In our implementation, IMU is used as the core sensor, and the pixel measurements obtained by cameras are treated as external aiding measurements for the Kalman filter. The core sensor IMU provides the dynamic information of the platform and the state errors are estimated with the pixel coordinates obtained by the stereo cameras. To tightly integrate INS and Stereo VO, the measurement of the Kalman filter are supposed to be the difference between the Stereo VO measurements and INS-derived corresponding measurements. Since the measurements of stereo images are the feature pixel coordinates, corresponding feature pixel coordinates need to be derived based on the INS mechanization results. In other words, the feature pixel coordinates need to be predicted based on the position and attitude resulted from INS mechanization results. Specifically, to predict the feature pixel coordinates on the image, the 3D feature coordinates in

the current camera frame have to be known, according to Eq (2.31). The 3D feature coordinates in the previous camera frame can be obtained by triangulation based on Eq (2.38). The rotation and translation of the camera can be calculated using the mechanization results and the feature coordinates can be transformed to the current camera frame. Therefore, the feature pixel coordinates can be predicted by re-projecting the features on the image plane based on the current camera position, attitude and the 3D feature coordinates. When the actual pixel coordinates of the tracked (or matched) features on the images are available, the mechanization errors can be estimated in the Kalman filter. In this way, the drift of IMU can be limited by visual information. In our implementation, the state vector in the Kalman filter includes the position errors, velocity errors, attitude errors in the LLF and the gyro, accelerometer biases in the IMU body frame. All the elements in the state vector are INS related parameters introduced in Section 2.2.3. There are no additional unknowns needs to be added in the state vector. The measurement update in EKF are the differences between the predicted feature pixel coordinates by re-projection and the measured pixel coordinates on images as shown in Eq (3.7)

$$Z_k = [\mathbf{u} \quad \mathbf{v}]_{derived}^T - [\mathbf{u} \quad \mathbf{v}]_{measured}^T \quad (3.7)$$

where $[\mathbf{u} \quad \mathbf{v}]_{derived}^T$ is the INS-derived feature pixel coordinate vector; $[\mathbf{u} \quad \mathbf{v}]_{measured}^T$ is the measured feature pixel coordinate vector.

The mechanization and its linear error-state system models are formed in the LLF defined as ENU (East-North-Up), which is widely applied in GNSS/INS and other fields. The INS mechanization procedures and the dynamic matrix of the INS errors in the LLF have been introduced in Section 2.2.3. The general implementation procedure of the integration is shown in Figure 3.3. The advantage of such a system architecture is that continuous navigation solution is always available

from the core sensor IMU, and the system can be easily augmented to include additional aiding sources such as GNSS.

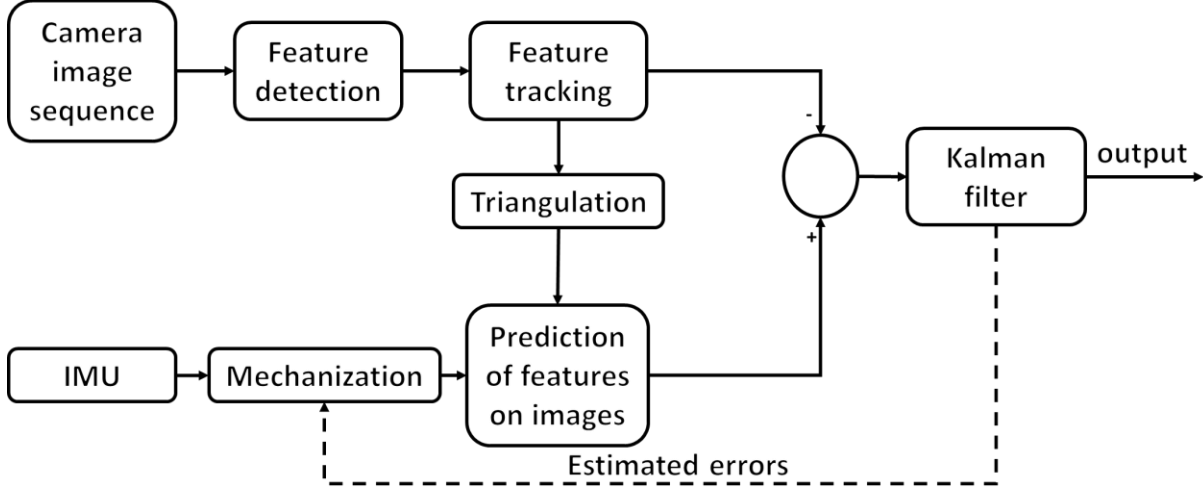


Figure 3.3 INS/Stereo VO Tight Integration Implementation Architecture

Since all the elements in the state vector are the INS related errors, the transition matrix $\Phi_{k,k-1}$, shaping matrix G and process noise covariance matrix Q do not need to be changed. The key to implementing the tight integration of INS and Stereo VO is the formulation of the design matrix H . The full derivation of the design matrix is presented in the following part.

In Stereo VO, the camera motion is usually denoted in a self-defined world frame (e.g. the camera frame in the first epoch). The triangulated feature coordinates expressed in the previous camera frame need to be transformed in the world frame, which can be done based on Eq (3.8).

$$P_f^w = R_b^c R_{l_0}^b R_{l_{k-1}}^{l_0} R_b^{l_{k-1}} R_c^b P_f^p + R_b^c R_{l_0}^b R_e^{l_0} (T_{k-1}^e - T_0^e) \quad (3.8)$$

where P_f^w is the 3D feature coordinates expressed in the world frame, R_i^j represents rotation matrix from frame i to frame j , c is left camera frame, b is IMU body frame, l_{k-1} is the local-level frame at the previous epoch, l_0 is the local-level at the first epoch, w is the world frame namely the left

camera frame at the first epoch, e is ECEF, P_f^p is the 3D feature coordinates obtained by triangulation of stereo images in the previous epoch. It can be seen from Eq (3.8) that the 3D feature coordinates in the world frame P_f^w can be decomposed as the vector from the perspective center to the feature and the vector from the beginning point to the perspective center. T_{k-1}^e is the perspective center at the previous epoch expressed in ECEF, subscript $k-1$ represents the previous epoch. T_0^e is the perspective center at the first epoch in ECEF. The rotation matrix R_b^e is available by the pre-measured misalignment, $R_b^{l_{k-1}}$ is the rotation obtained from the solution at the previous solution.

With the 3D feature coordinates in the world frame obtained from Eq (3.8), the feature coordinates expressed in the current camera frame can be given as

$$\vec{X}^c = R_w^c \vec{X}^w = R_b^c R_l^b R_{l_0}^l R_w^{l_0} (P_f^w - P_{cam}^w) \quad (3.9)$$

where \vec{X}^c is the vector from the perspective center to the features expressed in the current camera frame namely the feature coordinates in the current camera frame that need to be calculated; \vec{X}^w is the vector expressed in the world frame. P_{cam}^w is the perspective center position at the current epoch expressed in the world frame, which can be obtained by the position solution of IMU mechanization. The rotation matrix R_b^e is available by the pre-measured misalignment; R_l^b is the rotation matrix from LLF to body frame that can be obtained by the attitude solution of IMU mechanization. $R_w^{l_0}$ is known by initialization while the rotation matrix $R_{l_0}^l$ can be neglected if the translation from the beginning is not too far (within tens of kilometers). Otherwise, the rotation can be achieved as

$$R_l^{l_0} = R_e^{l_0} R_l^e \quad (3.10)$$

The rotation from LLF to ECEF is shown in Eq (3.11).

$$R_l^e = \begin{bmatrix} -\sin \lambda & -\sin \varphi \cos \lambda & \cos \varphi \cos \lambda \\ \cos \lambda & -\sin \varphi \sin \lambda & \cos \varphi \sin \lambda \\ 0 & \cos \varphi & \sin \varphi \end{bmatrix} \quad (3.11)$$

According to the feature coordinates in Eq (3.8), Eq (3.9) can be further derived as

$$\begin{aligned} \vec{X}^c &= R_w^c \vec{X}^w = R_b^c R_l^b R_{l_0}^l R_w^{l_0} (P_f^w - P_{cam}^w) = R_b^c R_l^b R_{l_0}^l R_w^{l_0} P_f^w - R_b^c R_l^b R_{l_0}^l R_w^{l_0} P_{cam}^w \\ &= R_b^c R_l^b R_{l_0}^l R_b^{l_0} R_c^b R_b^{l_0} R_{l_{k-1}}^{l_0} R_b^{l_{k-1}} R_c^b P_f^p + R_b^c R_l^b R_{l_0}^l R_e^{l_0} (T_{k-1}^e - T_0^e) - R_b^c R_l^b R_{l_0}^l R_w^{l_0} P_{cam}^w \end{aligned} \quad (3.12)$$

The above equation can be simplified as

$$\begin{aligned} \vec{X}^c &= R_b^c R_l^b R_{l_{k-1}}^{l_0} R_b^{l_{k-1}} R_c^b P_f^p + R_b^c R_l^b R_{l_0}^l R_e^{l_0} (T_{k-1}^e - T_0^e) - R_b^c R_l^b R_{l_0}^l R_e^{l_0} (T_k^e - T_0^e) \\ &= R_b^c R_l^b R_{l_{k-1}}^{l_0} R_b^{l_{k-1}} R_c^b P_f^p + R_b^c R_l^b R_{l_0}^l R_e^{l_0} (T_{k-1}^e - T_k^e) \end{aligned} \quad (3.13)$$

where T_k^e is the perspective center position at the current epoch expressed in ECEF, which is obtained from IMU mechanization.

According to Eq (3.13), the predicted feature coordinates in the camera frame depends on the relative rotation and translation from the previous epoch to the current epoch. This can be explained by Figure 3.4. The reprojection on the current image is based on the 3D coordinates obtained in the previous epoch, and the camera translation and rotation between consecutive epochs. The vector \vec{X}^c can be achieved by adding the vector from T_k^e to T_{k-1}^e and the vector P_f^p which are the first and second items in Eq (3.13). Before adding two vectors together, they should be transformed to the current camera frame.

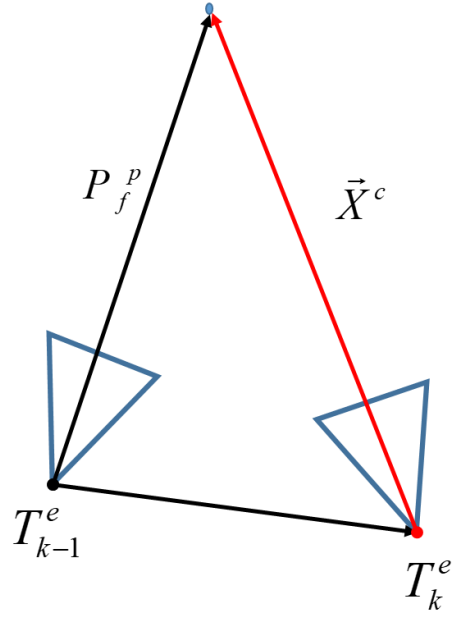


Figure 3.4 Feature Coordinates in the Current Camera Frame

The position and attitude solutions at the previous epoch are available, and the unknowns to be estimated in Eq (3.13) are the current position in ECEF and the current attitude. According to Eq (2.31), Eq (3.7) and Eq (3.13), the measurement vector is related to the position and the attitude errors, given as

$$\begin{aligned}
 H &= [H_r \quad 0_{2 \times 3} \quad H_\varepsilon \quad 0_{2 \times 3} \quad 0_{2 \times 3}] \\
 H_r &= \frac{\partial z}{\partial \vec{X}^c} \frac{\partial \vec{X}^c}{\partial r^i} \\
 H_\varepsilon &= \frac{\partial z}{\partial \vec{X}^c} \frac{\partial \vec{X}^c}{\partial \varepsilon}
 \end{aligned} \tag{3.14}$$

where H_r and H_ε represent the design matrix elements related to position error and attitude error.

The partial derivatives with respect to \vec{X}^c can be obtained easily by Eq (2.31), given as

$$\frac{\partial \vec{Z}_k}{\partial \vec{X}^c} = C = \begin{bmatrix} \frac{f_x}{z} & 0 & \frac{u_0}{z} - \frac{x}{z^2} \\ 0 & \frac{f_y}{z} & \frac{v_0}{z} - \frac{y}{z^2} \end{bmatrix} \quad (3.15)$$

where x, y, z, f_x, f_y, u_0 and v_0 are the same in Eq (2.31). The differential equation of Eq (3.13) can be given as

$$\delta \vec{X}^c = -R_b^c R_l^b \Psi R_b^{l_{k-1}} R_c^b P_f^p - R_b^c R_l^b \Psi R_e^l (T_{k-1}^e - T_k^e) - R_b^c R_l^b R_{l_0}^l R_e^{l_0} \delta T_k^e \quad (3.16)$$

where Ψ represents the skew-symmetric matrix of the attitude errors namely pitch, roll and yaw errors $(\delta p, \delta r, \delta y)$, given by

$$\Psi = \begin{bmatrix} 0 & -\delta y & \delta r \\ \delta y & 0 & -\delta p \\ -\delta r & \delta p & 0 \end{bmatrix} \quad (3.17)$$

In addition, with known latitude, longitude and height, the ECEF coordinates can be obtained by

$$\begin{bmatrix} x \\ y \\ z \end{bmatrix}_{ECEF} = \begin{bmatrix} (R_n + h) \cos \phi \cos \lambda \\ (R_n + h) \cos \phi \sin \lambda \\ [R_n(1 - e^2) + h] \sin \phi \end{bmatrix} \quad (3.18)$$

According to Eq (3.18), δT_k^e in Eq (3.17) can be further denoted in the local level frame as

$$\delta T_k^e = M \delta r^l$$

$$M = \begin{bmatrix} -(R_n + h) \sin \varphi \cos \lambda & -(R_n + h) \cos \varphi \sin \lambda & \cos \varphi \cos \lambda \\ -(R_n + h) \sin \varphi \sin \lambda & (R_n + h) \cos \varphi \cos \lambda & \cos \varphi \sin \lambda \\ [R_n(1 - e^2) + h] \cos \varphi & 0 & \sin \varphi \end{bmatrix} \quad (3.19)$$

Based on Eq (3.16) ~ Eq (3.19), the below equation can be derived

$$\begin{aligned}
\delta \vec{X}^c &= -R_b^c R_l^b \Psi R_b^{l_{k-1}} R_c^b P_f^p - R_b^c R_l^b \Psi R_e^l (T_{k-1}^e - T_k^e) - R_b^c R_l^b R_{l_0}^l R_e^{l_0} \delta T^e \\
&= -R_l^c \Psi R_p^l P_f^p - R_l^c \Psi R_e^l (T_{k-1}^e - T_k^e) - R_e^c M \delta T^l \\
&= R_l^c \Omega_f^l \varepsilon^l + R_l^c \Omega_{k-1,k}^l \varepsilon^l - R_e^c M \delta r^l
\end{aligned} \tag{3.20}$$

where R_e^c represents the rotation matrix from ECEF to the current camera frame, $\Omega_f^{l_{k-1}}$ is the skew-symmetric matrix of the feature coordinates in the local-level frame at the previous epoch, $\Omega_{k-1,k}^l$ is the skew-symmetric matrix of the perspective center translation from previous epoch $k-1$ to current epoch k in the local-level frame, ε^l is the attitude error in the state vector. Combining Eq (3.15) and (3.20), the submatrices in the design matrix associated with respect to position and attitude errors can be obtained, shown as follows

$$\begin{aligned}
H_r &= \frac{\partial z}{\partial X^c} \frac{\partial X^c}{\partial r} = -CR_e^c M \\
H_\varepsilon &= \frac{\partial z}{\partial X^c} \frac{\partial X^c}{\partial \varepsilon} = CR_l^c \Omega_f^l + CR_l^c \Omega_{k-1,k}^l
\end{aligned} \tag{3.21}$$

So far, the tight integration of INS and Stereo VO has been described and how the pixel coordinates on the images are used in the estimation is illustrated. Field test datasets have been applied to verify the effectiveness of the integration, which will be presented in Chapter 5.

3.3 Tight Integration of GNSS PPP, INS and Stereo VO

When GNSS signals are not blocked or interfered, GNSS signals (e.g. pseudoranges, carrier-phase, Doppler) can also be applied in the Kalman filter. In this section, the tight integration of GNSS PPP, INS and Stereo VO is presented. The integration architecture is the expansion of INS/Stereo VO integration. For Stereo VO, no additional unknowns need to be estimated. However, for PPP, apart from the position and velocity errors, the receiver clock error, receiver clock drift,

troposphere zenith delay and the ambiguities also need to be estimated. According to Eq (3.2), the state vector for the integrated system can be given as

$$X_k = [X_{INS} \quad X_{external}]^T = [\delta r^l \quad \delta V^l \quad \varepsilon^l \quad \delta f^b \quad \delta \omega^b \quad cdt^r \quad cdt \quad T \quad Amb]^T \quad (3.22)$$

where X_k has $18+n$ elements (n is the number of satellite), X_{INS} is the same as in Eq (3.2) containing 15 elements, cdt^r is the receiver clock error, cdt is the receiver clock drift, T is the zenith troposphere delay, Amb represents the IF ambiguities.

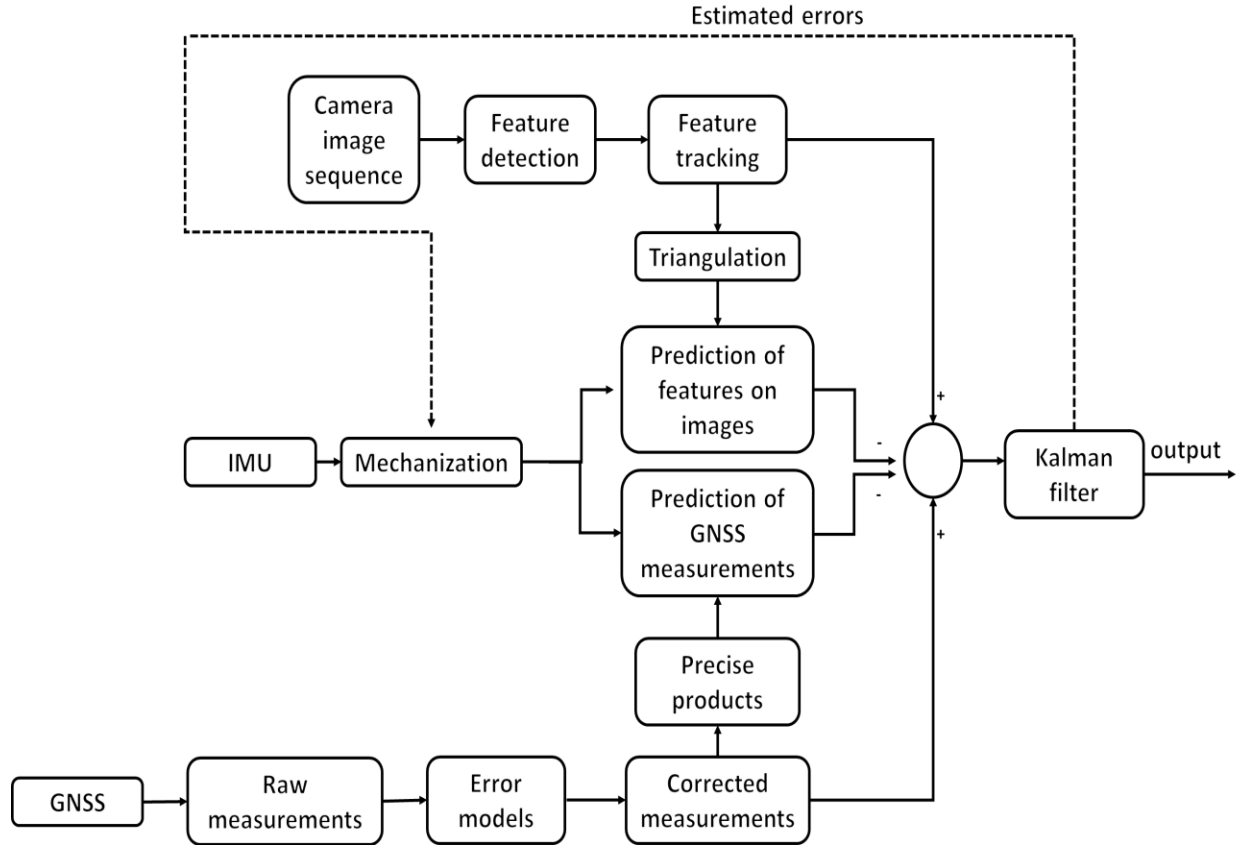


Figure 3.5 Implementation Procedures

The IMU mechanization results provide the dynamic information of the system namely the initial state (e.g. position, velocity, attitude) to predict the corresponding measurements of GNSS PPP

and Stereo VO. For instance, the position and velocity provided by the IMU are used to predict the GNSS measurements, while the position and attitude provided by the IMU are used to calculate the predicted pixel coordinates of features on the Stereo images. When GNSS or Stereo VO measurements are available, the corresponding differences between the predicted and actual measurements can be calculated to update the state vector. The closed-loop scheme is used in this work, which means that the corresponding errors are corrected for IMU mechanization after estimation. The implementation procedure is summarized in Figure 3.5.

The receiver clock error, receiver clock drift and troposphere delay for PPP need to be included in the state vector for PPP.

$$\begin{bmatrix} c\dot{d}t^r \\ c\dot{d}t \\ \dot{T} \end{bmatrix} = \begin{bmatrix} 0 & 1 & 0 \\ 0 & 0 & 0 \\ 0 & 0 & 0 \end{bmatrix} \begin{bmatrix} cdt^r \\ cdt \\ T \end{bmatrix} + G \cdot w \quad (3.23)$$

The ambiguities are modeled as random constant. The spectral density for troposphere is about $0.0001^2 \text{ m}^2/\text{s}$. The corresponding measurements applied in the Kalman filter with respect to different types of measurements are

$$Z = \begin{bmatrix} \delta_P \\ \delta_\Phi \\ \delta_D \\ \delta_u \\ \delta_v \end{bmatrix} = \begin{bmatrix} P_{IF} - P_{IMU} \\ \Phi_{IF} - \Phi_{IMU} \\ D_{IF} - D_{IMU} \\ u_{VO} - u_{IMU} \\ v_{VO} - v_{IMU} \end{bmatrix} \quad (3.24)$$

where Z is the measurement update in the Kalman filter, δ represents the difference between the actual and INS-derived measurements. The five types of measurements listed are ionosphere-free pseudoranges, carrier-phase measurements, Doppler measurements from GNSS PPP together with pixel coordinates u, v from stereo cameras, $*_{IMU}$ are the predicted measurements.

The corresponding design matrix can be given as

$$H = \begin{bmatrix} H_p \\ H_\phi \\ H_D \\ H_u \\ H_v \end{bmatrix} = \begin{bmatrix} SM & 0 & 0 & 0 & 0 & 0 & 1 & 0 & M_{trop} & 0 \\ SM & 0 & 0 & 0 & 0 & 0 & 1 & 0 & M_{trop} & I \\ S'M & SR_l^e & 0 & 0 & 0 & 0 & 0 & 1 & 0 & 0 \\ -C_1 R_e^c M & 0 & C_1 R_l^c \Omega_f^l + C_1 R_l^c \Omega_{k-1,k}^l & 0 & 0 & 0 & 0 & 0 & 0 & 0 \\ -C_2 R_e^c M & 0 & C_2 R_l^c \Omega_f^l + C_2 R_l^c \Omega_{k-1,k}^l & 0 & 0 & 0 & 0 & 0 & 0 & 0 \end{bmatrix} \quad (3.25)$$

where M , Ω_f^l , $\Omega_{k-1,k}^l$ are the same as in Eq (3.20); C_1 and C_2 are the first row and second row of matrix C in Eq (3.15). In addition, M_{trop} is the mapping function for the troposphere error in Eq (2.7), I is the identity matrix, R_a^b is the rotation matrix from frame a to frame b , S is the unit vector of line of sight from the receiver to the satellite, which can be given as

$$S = \begin{bmatrix} \frac{x^r - x^s}{\rho} & \frac{y^r - y^s}{\rho} & \frac{z^r - z^s}{\rho} \\ \vdots & \vdots & \vdots \\ \frac{x^r - x^s}{\rho} & \frac{y^r - y^s}{\rho} & \frac{z^r - z^s}{\rho} \end{bmatrix} \quad (3.26)$$

$$\rho = \sqrt{(x^r - x^s)^2 + (y^r - y^s)^2 + (z^r - z^s)^2}$$

where n is the number of satellites, ρ is the distance between the satellite and receiver. S' in Eq (3.25) can be given as

$$S' = \begin{bmatrix} \left(\frac{1}{\rho} - \frac{dx^2}{\rho^3} \right) dv_x - \frac{dydx}{\rho^3} dv_y - \frac{dzdx}{\rho^3} dv_{z1} & \cdots & \left(\frac{1}{\rho} - \frac{dx^2}{\rho^3} \right) dv_x - \frac{dydx}{\rho^3} dv_y - \frac{dzdx}{\rho^3} dv_{zn} \\ -\frac{dxdy}{\rho^3} dv_x + \left(\frac{1}{\rho} - \frac{dy^2}{\rho^3} \right) dv_y - \frac{dzdy}{\rho^3} dv_{z1} & \ddots & -\frac{dxdy}{\rho^3} dv_x + \left(\frac{1}{\rho} - \frac{dy^2}{\rho^3} \right) dv_y - \frac{dzdy}{\rho^3} dv_{zn} \\ -\frac{dxdz}{\rho^3} dv_x - \frac{dydz}{\rho^3} dv_y + \left(\frac{1}{\rho} - \frac{dz^2}{\rho^3} \right) dv_{z1} & \cdots & -\frac{dxdz}{\rho^3} dv_x - \frac{dydz}{\rho^3} dv_y + \left(\frac{1}{\rho} - \frac{dz^2}{\rho^3} \right) dv_{zn} \end{bmatrix}^T$$

$$\begin{aligned}
dx &= x^r - x^s \\
dy &= y^r - y^s \\
dz &= z^r - z^s \\
dv_x &= v_{xr} - v_{xs} \\
dv_y &= v_{yr} - v_{ys} \\
dv_z &= v_{zr} - v_{zs}
\end{aligned} \tag{3.27}$$

where v_{xr} , v_{yr} and v_{zr} represent the land vehicle velocity in x , y and z direction in ECEF; v_{xs} , v_{ys} and v_{zs} represent the satellite velocity in x , y and z directions in ECEF.

The determination of the variance-covariance matrix for the different types of measurements are as follows. The standard deviations for IF pseudoranges, carrier-phase and Doppler measurements are set as 3 meters, 0.03 centimeters and 0.03 cm/s respectively. As for the pixel coordinates, since KLT tracking method is adopted to find the correspondences in consecutive images, the tracking errors of features on the images are adopted as standard deviations for pixel coordinates.

So far, the matrices in the Kalman filter are all presented. Base on the Kalman filter equations in Eq (3.1), the tightly coupled multi-sensor integration can be implemented.

3.4 Summary

The multi-sensor tight integration scheme with IMU as the core sensor in this thesis is first introduced. The IMU provides the dynamic information of the land vehicle and predicts the other types of the measurements based on the mechanization results. The differences between the predicted and received measurements are used to estimate the errors.

The details of the implementation of tight integration of INS and Stereo VO have been presented. How the pixel coordinates are fused in the Kalman filter is also illustrated. Based on the rotation and translation between two epochs provided by IMU mechanization together with the 3D

coordinates of features obtained by the triangulation of stereo cameras, the pixel coordinates of the features in the next epoch can be predicted. The differences between the predicted pixel coordinates by IMU mechanization and measured pixel coordinates by tracking are used in the Kalman filter to correct the errors. In this way, the pixel coordinates are directly used to estimate the position and attitude errors. Since the position is highly correlated with the velocity estimation, the velocity can be updated as well. The correction of the velocity is the key to limiting the quick drift of INS mechanization.

The tightly coupled integration of INS and Stereo VO architecture can also be extended with GNSS measurements. The multi-sensor integration in this work is based on IMU as the core sensor. All the other types of measurements are used as the external aiding measurements in the Kalman filter. In the Kalman filter, the state vector and the dynamic matrix need to be extended if additional parameters for external measurements are required. In the integration of INS, Stereo VO and GNSS, the receiver clock, clock drift, troposphere zenith delay and the ambiguities are included in the state vector, and the dynamic matrix needs to be extended correspondingly. The design matrix is the key to the implementation of the integration, which has been illustrated in detail.

Chapter Four: DEVELOPMENT OF MAP MATCHING AND INTEGRATED SYSTEM FOR LAND VEHICLE NAVIGATION

In addition to GNSS, Map Matching is another way to provide the absolute positioning information. In this chapter, the fuzzy logic Map Matching method is introduced and integrated in the land vehicle navigation system. By projecting the INS/Stereo VO solution on the digital map in GNSS denied environments, the accumulated errors can be largely reduced. In Section 4.1, the fuzzy logic Map Matching method is introduced. In Section 4.2, Map Matching is integrated with INS/Stereo VO to improve the solution accuracy when there is GNSS outage. In open sky environment, GNSS outperforms the other types of navigation systems. With a single GNSS receiver, PPP can achieve centimeter to decimetre level accuracy after the convergence which takes tens of minutes. When the receiver is in kinematic mode, it takes even longer for PPP to get converged, and the PPP ambiguity resolution in kinematic mode is more difficult. A fast kinematic PPP AR method with the aid of Map Matching is proposed. The integer search space for N_I ambiguities is reduced with the positioning information provided by Map Matching. The details are presented in Section 4.3.

4.1 Fuzzy Logic Map Matching

Map Matching can project the land vehicle position on digital maps by identifying the correct link that the land vehicle is moving along. Generally, the Map Matching algorithms can be classified into three main categories, namely the geometric Map Matching (Greenfeld, 2002), the topological Map Matching (Meng, 2006) and the advanced fuzzy logic Map Matching (Quddus, 2006). Geometric Map Matching algorithm only takes advantage of the geometry of the digital road network. Several geometric Map Matching methods have been developed namely point-to-point Map Matching, point-to-curve Map Matching and curve-to-curve Map Matching. Point-to-point

Map Matching finds the closest node to vehicle position, which is sensitive to how the road network is digitized and would generate numerous mismatches. Point-to-curve Map Matching identifies the closest road link to the vehicle position, which is easy to be implemented but a considerable number of mismatches exist as well. Curve-to-curve Map Matching finds the closest road link to a traveled line segment, which would reduce the mismatching possibility. Topological Map Matching algorithm makes use of not only the geometry of the digital road network but also the connectivity and continuity of the road links. A weighting scheme is used to assign weights to the candidate links. The perpendicular distance of the vehicle position from the link (proximity), the degree of the parallelism between the traveled line and the link (orientation), and the angle between the traveled line and the road link (intersection) are all taken into consideration. The topological Map Matching improves the correct link identification, but it is still sensitive to outliers. Quddus (2006) proved that the fuzzy logic Map Matching method outperforms the other two methods in terms of correct link identification, validation, and integrity. Fuzzy logic Map Matching utilizes the fuzzy logic theory to determine the maximum likelihood of the candidate links based on the land vehicle state and digital map information. Hence, the principles of fuzzy logic theory and fuzzy logic Map Matching procedures are illustrated below.

4.1.1 Overview of Fuzzy Logic Theory

Fuzzy logic utilizes the real number between 0 and 1 to represent the situation instead of true or false in Boolean logic, which has been widely applied in control theory and data processing (Rosyara, Vromman, & Duveiller, 2008). In other words, fuzzy logic uses an imprecise but very descriptive variable to represent the likelihood of current state. The fuzzy logic has several advantages. It is robust, does not require precise and noise-free inputs, generates smooth output

despite wide-range of input variation and can be applied to complicated systems which are difficult to model. The development of fuzzy logic theory is reviewed by Zadeh (1965), Van Broekhoven & De Baets (2008), Sugeno & Takagi (1983) and Mamdani (1974). This section only briefly overviews the fuzzy logic theory. The procedures of fuzzy logic can be divided into three main steps namely 1). Fuzzify all the input values into fuzzy membership functions; 2). Execute the rules of the membership functions to compute the fuzzy output; 3). De-fuzzify the fuzzy output to generate the final output. The membership function is a curve that defines how the inputs are mapped to a membership value between 0 and 1, as shown in Figure 4.1.

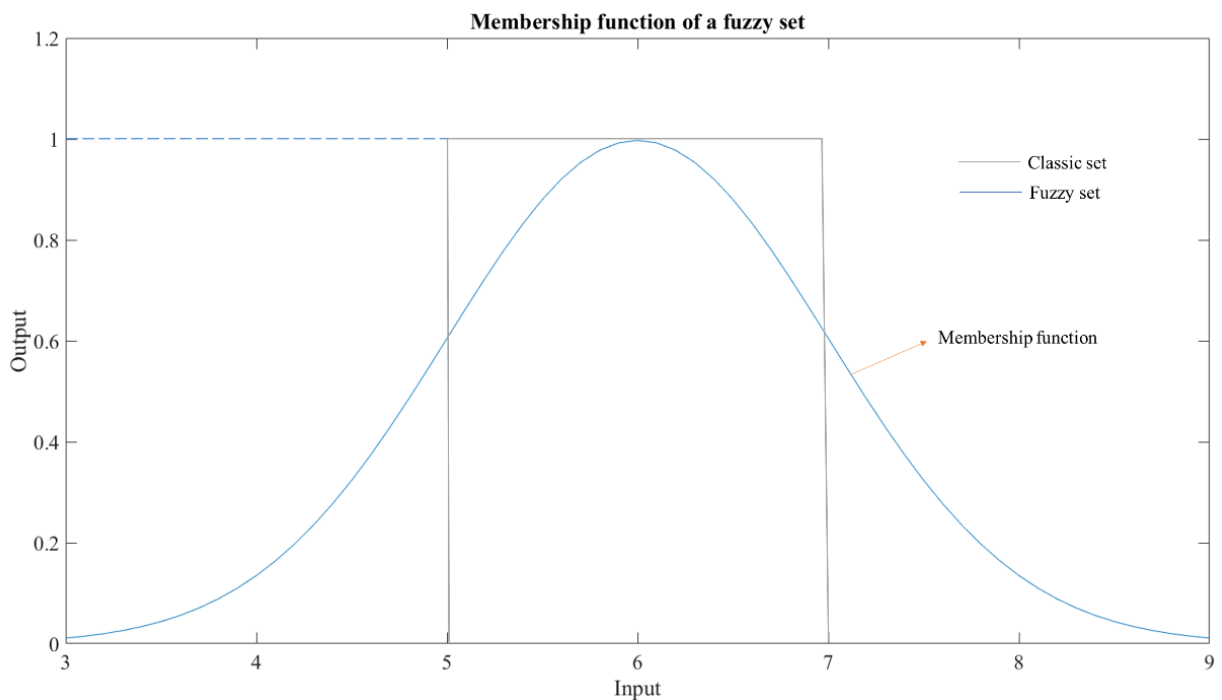


Figure 4.1 Membership Function Example

It can be seen from Figure 4.1 that in the fuzzy set, instead of defining the clear boundary in classic (crisp) set, the membership function converts the input to fuzzy values. Fuzzy logic usually adopts simple IF-THEN rules (e.g. If X is A and Y is B THEN Z is C) in the second step. In the IF-THEN

rules, non-numeric values are often used to facilitate the expression of rules and facts. One simple example is that IF the temperature is cold and the moisture is low THEN the fan speed is slow. The input variables of this rule are the temperature and moisture, and the input fuzzy subsets are cold and low. The output variable is the speed of the fan and the output fuzzy subset is slow.

Sugeno's Fuzzy Inference System (FIS) (Sugeno & Takagi, 1983) is applied to the fuzzy logic Map Matching in this thesis. To explain the fuzzy logic rules more clearly, this time we use a Map Matching example to illustrate the Sugeno's FIS. Two fuzzy rules are applied as 1): IF the heading error (HE) (the difference between the vehicle heading and the link azimuth) is small and the perpendicular distance (PD) from the vehicle position to the road link is small THEN the likelihood of the correct link matching is high; 2). IF the HE is large and PD is long THEN the likelihood of the correct link matching is low. To be more specific, the procedure can be divided into 5 steps. The first step is to define the fuzzy variables, fuzzy subsets and their membership functions together with the fuzzy rules. The fuzzy variables in this example are the HE and PD, while the corresponding fuzzy subsets for HE and PD are small, large and short, long respectively in the two fuzzy rules. The challenging task is the shape definition of membership functions. There are different membership function shapes such as triangular, trapezoidal, Z-shaped, S-shaped, Gaussian, etc. One instance for the "HE is small" membership function can be defined as:

$$\mu_{HE_SMALL} = \begin{cases} 1 & HE \leq 20^\circ \\ 1 - 2\left(\frac{HE - 20}{25}\right)^2 & 20^\circ < HE \leq 32.5^\circ \\ 2\left(\frac{HE - 45}{25}\right)^2 & 32.5^\circ < HE \leq 45^\circ \\ 0 & HE > 45^\circ \end{cases} \quad (4.1)$$

where μ_{HE_SMALL} is the membership value for “HE is small”, HE is the heading error input. In contrast, the membership function for “HE is large” can be given as:

$$\mu_{HE_LARGE} = \begin{cases} 0 & HE \leq 25^\circ \\ 2\left(\frac{HE - 25}{35}\right)^2 & 25^\circ < HE \leq 42.5^\circ \\ 1 - 2\left(\frac{HE - 60}{35}\right)^2 & 42.5^\circ < HE \leq 60^\circ \\ 1 & HE > 60^\circ \end{cases} \quad (4.2)$$

Similarly, the membership functions for “PD is short” and “PD is long” can be defined as

$$\mu_{PD_SHORT} = \begin{cases} 1 & PD \leq 0.9 \\ 1 - 2\left(\frac{PD - 0.9}{1.6}\right)^2 & 0.9 < PD \leq 1.7 \\ 2\left(\frac{PD - 2.5}{1.6}\right)^2 & 1.7 < PD \leq 2.5 \\ 0 & PD > 2.5 \end{cases} \quad (4.3)$$

$$\mu_{PD_LONG} = \begin{cases} 0 & PD \leq 3 \\ 2\left(\frac{PD - 3}{4}\right)^2 & 3 < PD \leq 5 \\ 1 - 2\left(\frac{PD - 7}{4}\right)^2 & 5 < PD \leq 7 \\ 0 & PD > 7 \end{cases} \quad (4.4)$$

The plots of the membership functions can be given as:

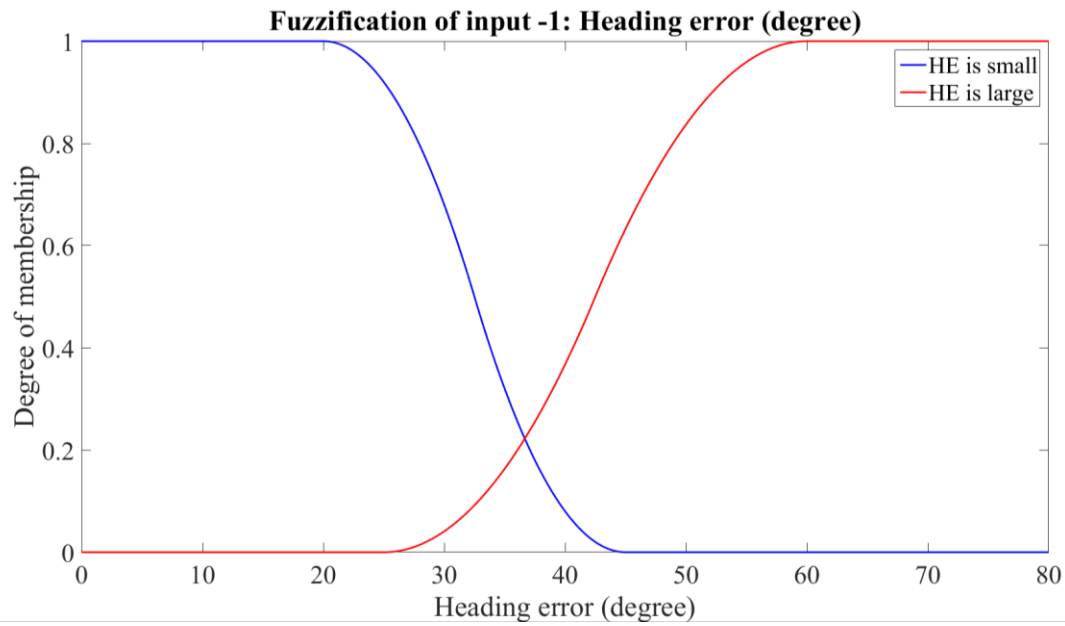


Figure 4.2 Membership Functions for HE

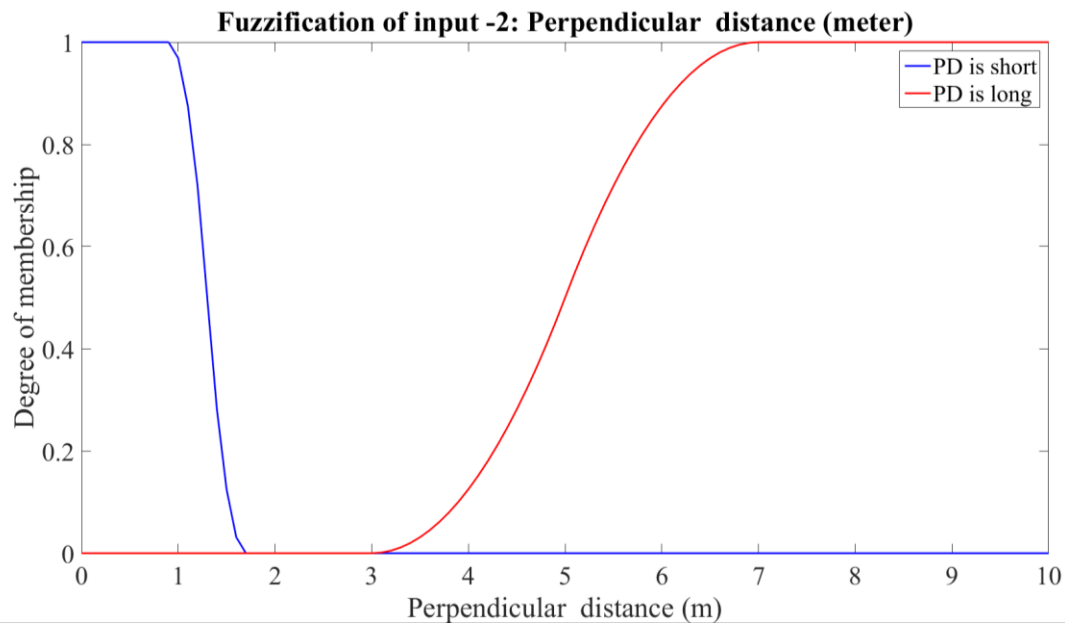


Figure 4.3 Membership Functions for PD

The second step is the application of fuzzy operators. In the example given above, there are two parts in one fuzzy rule to determine the correct link matching likelihood namely “HE is small” and

“PD is short”. Fuzzy operators (AND, OR) are normally used to combine the two parts in one rule. Two popular AND methods are *min* (minimum) and *prod* (product), and two widely applied OR methods are *max* (maximum) and the probabilistic OR method. In this thesis, the AND and OR methods adopt *min* and *max* methods respectively. For instance, given that *HE* is 20 degrees and PD is 3 meters, for the two parts “HE is small” and “PD is short” in the rule, the fuzzy membership values are 1 and 0 respectively. Using the *min* method, the final membership function output is 0. The third step is to assign weight to each rule. In the example, using Sugeno’s Fuzzy Inference System, a constant number is applied to describe the correct Map Matching likelihood (e.g. 100 for high, 10 for low). In other words, multiplying the rule strength and the assigned weight for each rule is the result of each fuzzy rule.

The fourth step is the aggregation of each fuzzy rule result. Assuming that W_i is the rule strength obtained in the second step, Z_i is the weight assigned in the third step, the weighted average of the consequences is the output of the system shown as:

$$Z = \frac{\sum_{i=1}^n W_i Z_i}{\sum_{i=1}^n W_i} \quad (4.5)$$

The last step is to determine the link as the correct one with maximum Z value.

4.1.2 Fuzzy Logic Map Matching Procedures

The fuzzy logic Map Matching adopts the fuzzy logic to calculate the likelihood of each road link. It can be divided into two steps: Initial Map Matching Process (IMP) and Subsequent Map Matching Process (SMP). SMP can be further divided as SMP along a link (SMP-1) and SMP close to a junction (SMP-2). Each step is illustrated in the following part.

4.1.2.1 Initial Map Matching Process.

As the name indicates, an initial road link is selected in IMP. Road links around the land vehicle within a certain radius are selected as the candidates for IMP. At least one link should be included in the candidates. Otherwise, the radius has to be increased. Each road link candidate needs to be assigned likelihood value based on the five steps introduced in above. The inputs of MF are the land vehicle position, velocity, heading error (HE), perpendicular distance (PD) from the vehicle position to the road link and the GNSS HDOP (Horizontal Dilution Of Precision). IF-THEN rules are applied to identify the likelihood of matching the vehicle position to the link. Here, LH1 is used to denote the likelihood. The rules for IMP can be summarized as follows.

- 1) If HE is small and velocity is high, then LH1 is average.
- 2) If HE is large and velocity is high, then LH1 is low.
- 3) If PD is short and HE is small, then LH1 is high.
- 4) If PD is long and HE is large, then LH1 is low.
- 5) If PD is short and HDOP is good, then LH1 is average.
- 6) If PD is long and HDOP is good, then LH1 is low.

According to Quddus (2006), the membership functions for “HE is small”, “HE is large”, “PD is short” and “PD is long” are shown in Figure 4.11 and Figure 4.12 while “velocity is fast”, “velocity is slow”, and “HDOP is large”, “HDOP is small” are given as:

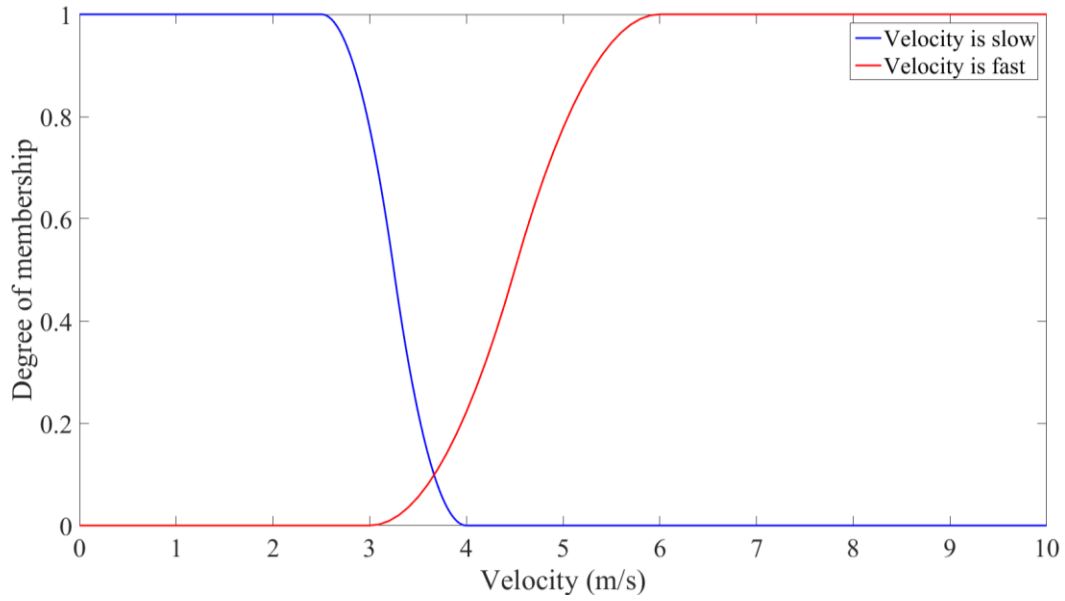


Figure 4.4 Membership Functions for Velocity

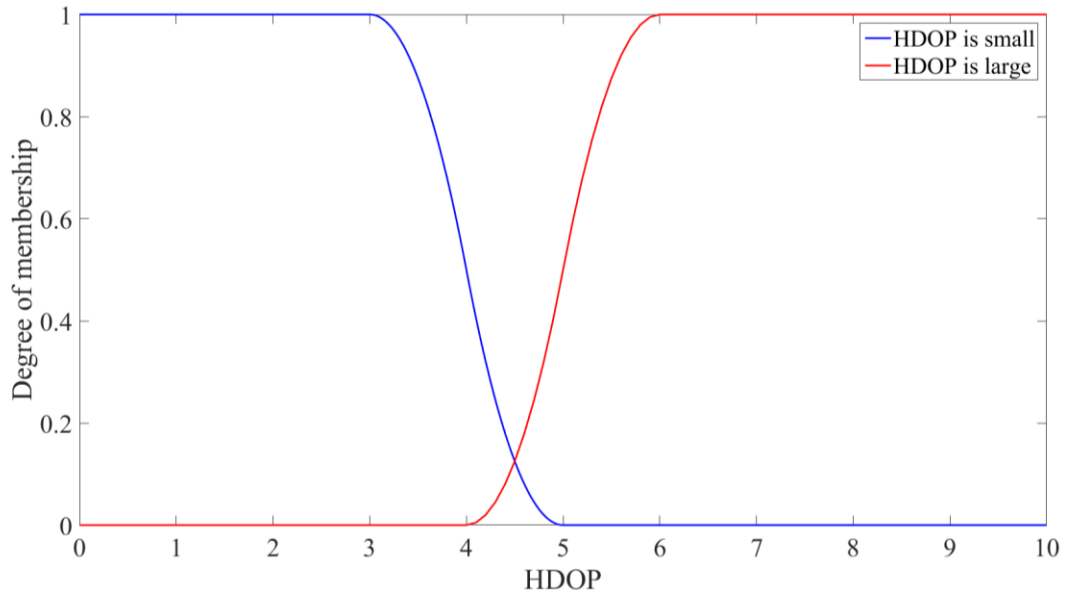


Figure 4.5 Membership Functions for HDOP

The weights assigned for “LH1 is high” “LH1 is average” and “LH1 is low” are 100, 50 and 10 respectively. Using Eq (4.5), the road link with the largest likelihood is determined as the correct

one and the perpendicular projection of the vehicle position on the selected link is the map matched point. If the same link is selected for several consecutive epoch, IMP is finished, and the fuzzy logic Map Matching starts the second step SMP. IMP is of great importance since it is the first step and the result would have an impact on the following step SMP.

4.1.2.2 Subsequent Map Matching Process

After determination of the correct link in IMP, SMP is activated to check whether the vehicle is still on the same road link (SMP-1) and whether the land vehicle is approaching or just crossing the junction (SMP-2). In addition to the inputs for IMP, the vertical gyro-rate reading $\Delta\theta$ and the parameters illustrated in Figure 4.6 are also input to SMP. In Figure 4.6, α is the angle between the current point, previous map matched point and the junction; β is the angle between the current point, junction and the previous map matched point; P_k is the current vehicle position and P_{k-1} is the previous vehicle position; d_1 is the distance between the previous map matched point and the junction; d_2 is the distance travelled by car; d_3 is the shortest distance between the perpendicular projection of the vehicle position on the candidate road links and the previous map matched point.

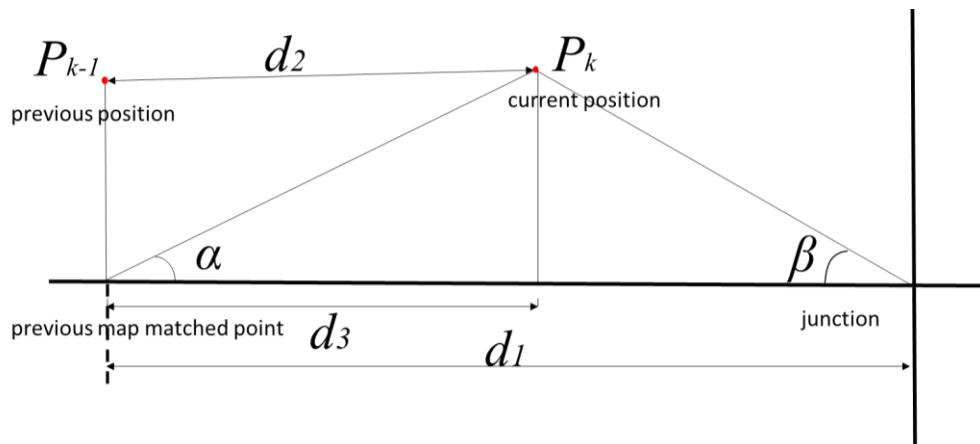


Figure 4.6 Parameters for Fuzzy Logic Map Matching (Quddus, 2006)

The fuzzy logic rules for SMP-1 are as follows. The likelihood for SMP-1 is denoted as LH2.

- 1) If α is below 90, β is below 90 and $\Delta\theta$ is small, then LH2 is high.
- 2) If Δd (d_1-d_2) is positive, α is above 90 and $\Delta\theta$ is small, then LH2 is low.
- 3) If Δd is positive, β is above 90 and $\Delta\theta$ is small, then LH2 is low.
- 4) If α is below 90, β is below 90 and HI (Heading Increment, namely the difference between the vehicle headings at consecutive epochs) is small then LH2 is high.
- 5) If Δd is positive, α is above 90 and HI is small then LH2 is low.
- 6) If Δd is positive, β is above 90 and HI is small then LH2 is low.
- 7) If α is below 90, β is below 90 and $\Delta\theta$ is small, then LH2 is low.
- 8) If α is below 90, β is below 90 and HI is large, then LH2 is low.
- 9) If HI is small and the velocity is high, then LH2 is average.
- 10) If the velocity is zero and HDOP is good, then LH2 is high.
- 11) If Δd is negative and HDOP is good, then LH2 is low.
- 12) If Δd is positive and HDOP is good, then LH2 is average.
- 13) If velocity is high, HI is 180° and HDOP is good and $\Delta\theta$ is small then LH2 is high.

According to Quddus (2006), the membership functions for “ α is below 90”, “ α is above 90”, “vertical gyro-rate reading $\Delta\theta$ is small”, “vertical gyro-rate reading $\Delta\theta$ is large”, “ Δd is negative”, “ Δd is positive”, “HI is small”, “HI is large” and “HI is 180°” are given as:

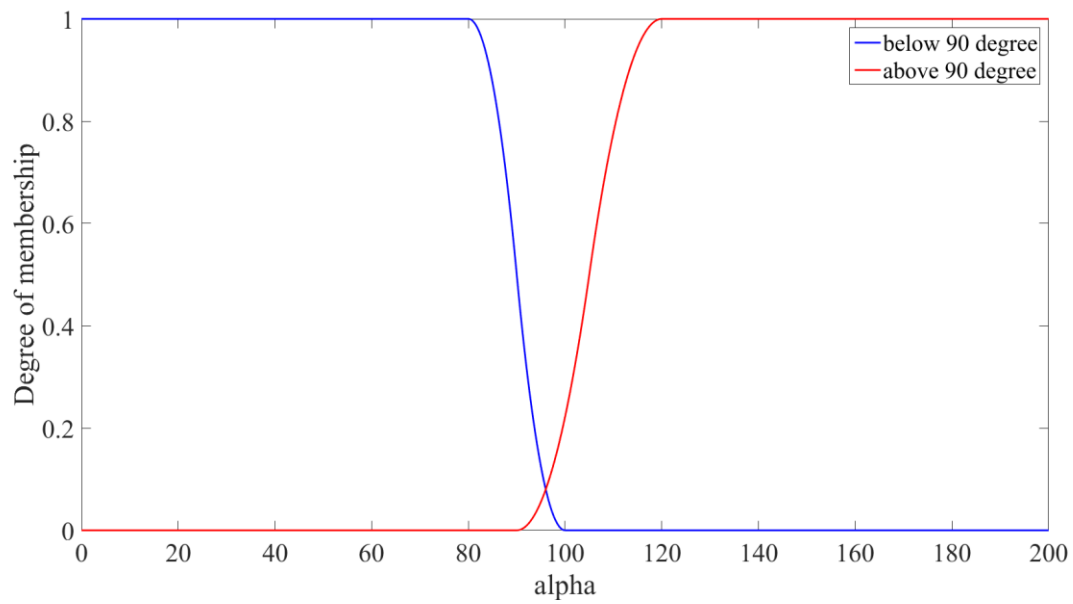


Figure 4.7 Membership Functions for α

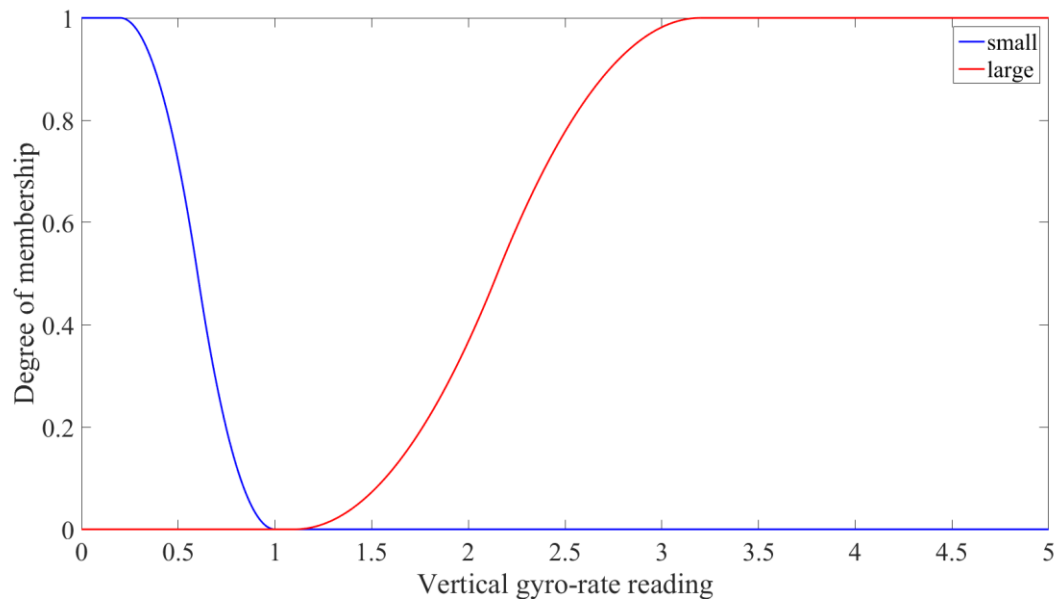


Figure 4.8 Membership Functions for $\Delta\theta$

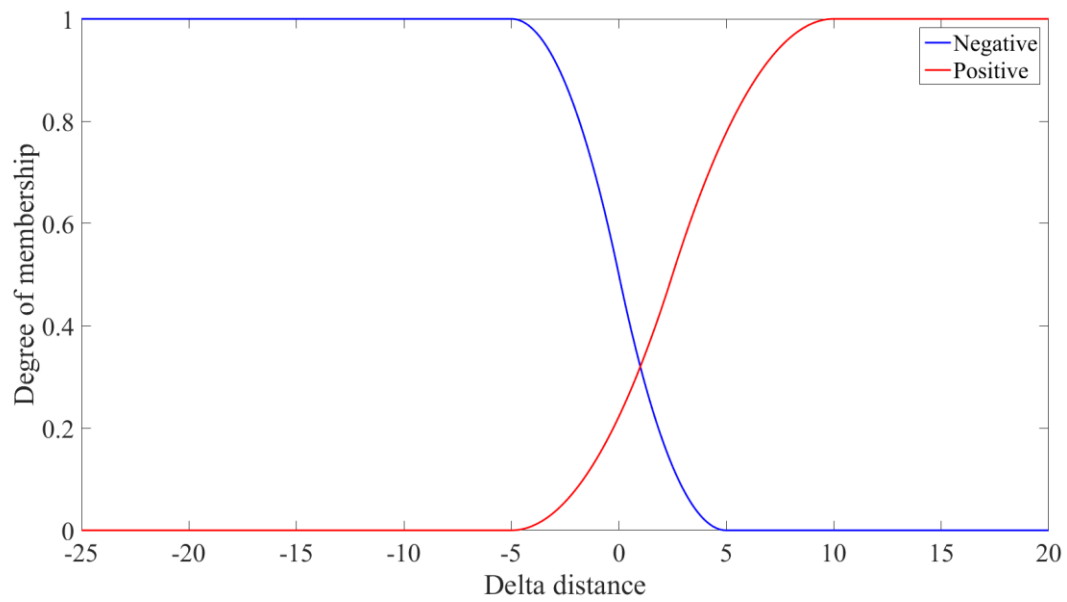


Figure 4.9 Membership Functions for Δd

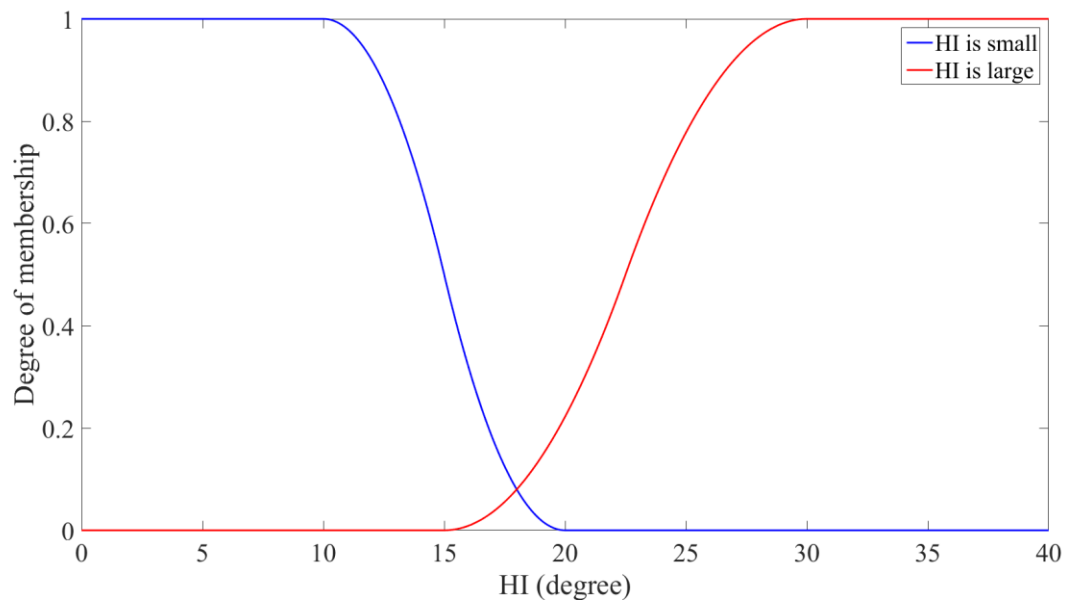


Figure 4.10 Membership Functions for HI

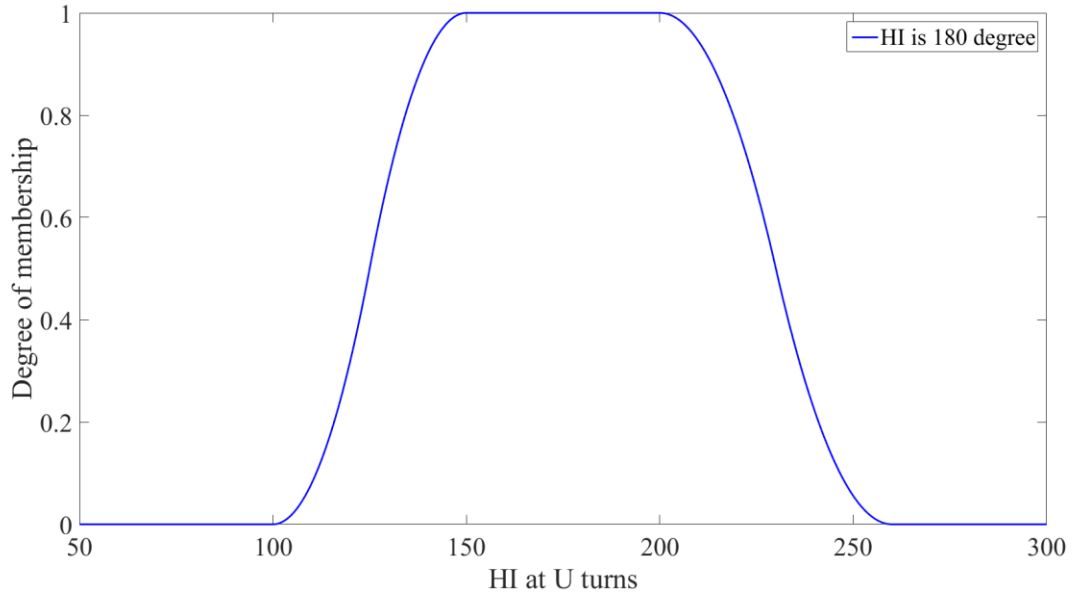


Figure 4.11 Membership Functions for HI at U-Turns

The weights assigned for “LH2 is high” “LH2 is average” and “LH2 is low” are 100, 50 and 10 respectively. Using Eq (4.5), the likelihood of the selected road link can be calculated. If the calculated value is greater than a certain threshold, the vehicle is still moving on the same road link. Otherwise, the Map Matching moves to the next step SMP-2. The SMP-2 is also activated when the vehicle is near the junction or has just crossed the junction. SMP-2 fuzzy inference system has ten fuzzy rules (Quddus 2006). Apart from the six rules used in IMP, four additional rules are listed as follows

- 1) If the connectivity with the previous link is true, then LH3 is high.
- 2) If the connectivity with the previous link is false, then LH3 is low.
- 3) If the distance error is high, then LH3 is low.
- 4) If the distance error is low, then LH3 high.

where distance error equals to $|d_2 - d_3|$, connectivity checks whether the candidate links are connected to previously selected link or not. The connectivity is Boolean logic while the membership functions for “distance error is low” and “distance error is high” are given as:

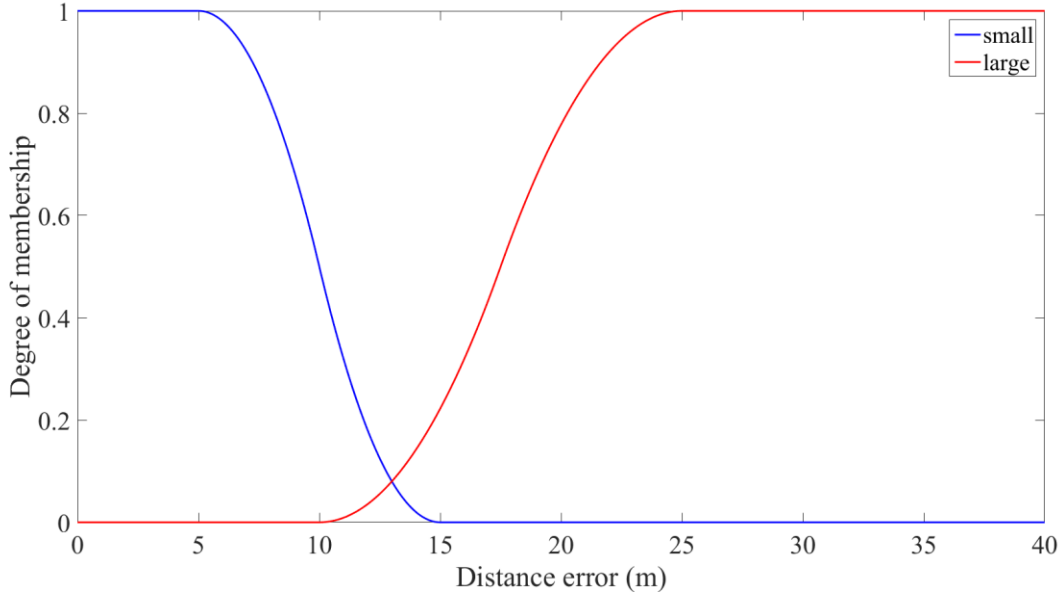


Figure 4.12 Membership Functions for Distance Error

Similarly, the weights is defined as the constant values used in IMP and SMP-1. The link with the largest likelihood is selected as the correct one. If the selected link likelihood is smaller than a threshold, Map Matching goes back to the IMP step.

4.2 Tight Integration of INS, Stereo VO and Digital Map

As illustrated before, in addition to GNSS, the digital map can also provide absolute positioning information for DR systems to limit the unbounded accumulated positioning errors. The fuzzy logic Map Matching algorithms can be further integrated with the INS/Stereo VO system introduced in the previous chapter. This section is mainly about the integration of the INS, Stereo VO and Map Matching. INS/Stereo VO system can provide the navigation solution for Map Matching. Map Matching has two roles. The first role is to identify the correct road link and to

project the vehicle position on the selected road link based on the integrated results and the digital map information. The second role is to reduce the drift error of INS/Stereo VO system by constraining the vehicle position on the road link. Map Matching provides the feedbacks including the position of the map matched point and the azimuth of the road link for IMU mechanization in next epoch to reduce the drift of the integration solution of INS and StereoVO.

In this thesis, the digital used map is based on the OpenStreetMap (OSM) (<https://www.openstreetmap.org>). OSM provides digital maps of most cities worldwide in shape files. An open source Relational DataBase Management System (RDBMS) named PostgreSQL was used to load the road link shape file which includes the information about road line string geometry, start point and end point position of each road link, road link length and azimuth. The Map Matching algorithm introduced in the previous section was applied with PostgreSQL managing the spatial queries. The processing flow is illustrated in Figure 4.13.

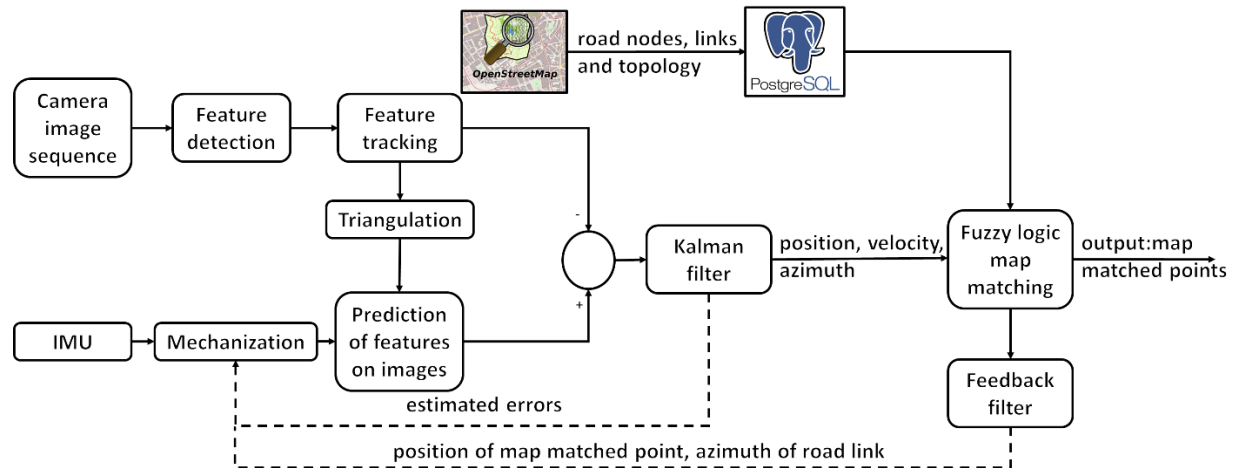


Figure 4.13 Tightly Coupled Integration of Digital Map and INS/Stereo VO.

This figure is the expansion of Figure 3.3. It can be seen from Figure 4.13 that the outputs of tightly coupled INS/Stereo VO (e.g. position, velocity and azimuth) are used for fuzzy logic Map Matching together with the digital map information from OSM. PostgreSQL is used to manage the digital map data. The fuzzy logic Map Matching algorithms illustrated in the previous section are used to find out the map matched points on the digital map, which are further used as feedbacks to compensate for the errors in IMU mechanization in the next epoch, in order to limit the drift of INS/Stereo VO. For the fuzzy logic rules in IMP, SMP-1 and SMP-2, the GNSS related rules are removed since only IMU and stereo cameras are used in this implementation. It is of great importance that the map matched points found by the fuzzy logic Map Matching algorithms are correct since it would cause significant error in positioning if incorrect Map Matching feedback is used for INS/Stereo VO. To avoid incorrect map matched points, a feedback filter is designed to guarantee the correctness of the map matched points. The criteria of the feedback filter are listed as follows. Firstly, the SMP-1 has to show that the vehicle is still on the same road link. Secondly, the HE needs to be smaller than a threshold. Thirdly, the vertical rotation angle has to be smaller than a threshold, which means that the vehicle is not turning. Lastly, the distance to junctions should be greater than a threshold. Map Matching has to meet all the four requirements to pass the feedback filter.

After passing the feedback filter, the map matched point position and the road azimuth information would be used for the IMU mechanization in next epoch. Specifically, the integrated output roll, pitch and the road link azimuth are used to calculate R_b^l (the rotation matrix from the body frame to the local-level frame), and the map matched latitude and longitude are used to calculate R_l^e (the rotation matrix from the local-level frame to the ECEF frame), the position is replaced with the

map matched point. In this way, the estimated position of INS/Stereo VO is forced to the road links on the digital map, which could largely reduce the quick drift.

4.3 Tight Integration of GNSS PPP and Map Matching

In open sky environment, GNSS is still the best option to achieve accurate solutions. PPP can provide world-wide decimeter to centimeter level solutions using just one receiver after convergence of ambiguities. However, it usually takes tens of minutes for PPP to get converged especially in kinematic mode, which limits its applications. PPP AR could reduce the convergence time by fixing the PPP ambiguities. But it still needs tens of minutes for PPP AR to fix the ambiguities because the float IF ambiguities have to get converged to a certain accuracy level first to ensure the successful fixing rate. The key to reducing the ambiguity integer searching time is to reduce the number of integer candidates. One way is to increase the carrier-phase wavelength toward decreasing the number of the candidate. This involves the application of triple-frequency signals. However, triple-frequency precise products are not widely applied yet, and there exist some issues in the GPS third frequency phase signals (Li, Zhou et al., 2012; Liu and Gao, 2017; Montenbruck, et al., 2012). The other way is to reduce the search space of the integer ambiguities. The second strategy is adopted in this thesis. To accelerate the ambiguity convergence, external position information is needed. For the conventional multi-sensor integration system (e.g. GNSS/INS), DR systems are usually integrated with GNSS PPP. However, DR system solutions depend on the previous solution, which means that it could make the integrated system get re-converged faster than the stand-alone GNSS PPP system. However, the integration with DR systems does little to the PPP convergence at the very beginning. In this research, different from the GNSS and DR system integration method, the accurate digital map is used to provide the

external position information. When the land vehicle is moving on the road, the PPP solution is projected on the corresponding road link by Map Matching. The projected point position on the road link would be applied as additional measurements in Kalman filter to accelerate the PPP convergence. If the map matched point on the road link is accurate, the error of PPP solution in the cross-road direction can be largely reduced. Since the projection is perpendicular to the road link, the along-road error is not reduced.

The PPP ambiguity resolution and Map Matching methods have been reviewed in Section 2.1.2 and Section 4.2.2 respectively. In this section, the method to tightly integrate GNSS PPP and Map Matching algorithms is introduced. In this work, the integer clock products provided by CNES are used to recover the integer properties of PPP ambiguities. Eq (2.17) ~ Eq (2.20) are used to implement the PPP AR. Specifically, single-difference between-satellite is implemented to remove the receiver clock error. The PPP IF ambiguities can be decomposed as WL and NL ambiguities according to Eq (2.15). The MW combination is applied to fix the WL ambiguities while LAMBDA method is adopted to search for the NL ambiguities. The fuzzy logic Map Matching method introduced in Section 4.2.2 is applied to project the PPP solutions on the road links. The Map Matching rules are illustrated before, and the gyro related rules are removed since only GNSS is applied in this implementation. Generally, at the very beginning, the correct road link is selected around the PPP solution in IMP with several candidates. While the land vehicle is moving on, SMP-1 checks whether it is still on the selected road link. When the land vehicle is approaching to or just crossing an intersection, the road link has to be re-selected according to SMP-2 rules. The map matched points and road link azimuth can be applied as additional measurements apart from code and phase measurements as

$$z = \begin{bmatrix} X_{map} - X_{PPP} \\ \alpha_{map} - \alpha_{PPP} \end{bmatrix} \quad (4.6)$$

where X_{map} and α_{map} represent the map matched point coordinates and road link azimuth respectively; X_{PPP} and α_{PPP} are the PPP position and azimuth solutions. With the additional Map Matching constraints, not only the positioning accuracy would be improved, the ambiguities can get converged faster. This is because the ambiguities are correlated with the position parameters. The general implementation procedure of the tight integration of PPP and Map Matching is shown in Figure 4.14. The Precise Point Positioning is implemented using P3 software developed at the University of Calgary. Position errors, zenith tropospheric delay and ambiguities are estimated in Kalman filter. In general, the float solution is first projected on the road links if the Map Matching passes the feedback filter. Then the outputs of Map Matching are further used as external measurements to estimate the float solution and accelerate the convergence of ambiguities. The feedback filter is to ensure the road link selected by Map Matching is correct. Because the incorrect map matched point would cause a serious problem for the PPP AR. In this implementation, the feedback filter has to check whether the land vehicle is still moving on the previous road link selected, the heading error is smaller than the given threshold, and the distance to the road junction is larger than the given threshold. When the covariance of the ambiguities is reduced to a certain level, the fixed solution can be achieved. In this way, fast kinematic PPP ambiguity resolution becomes possible.

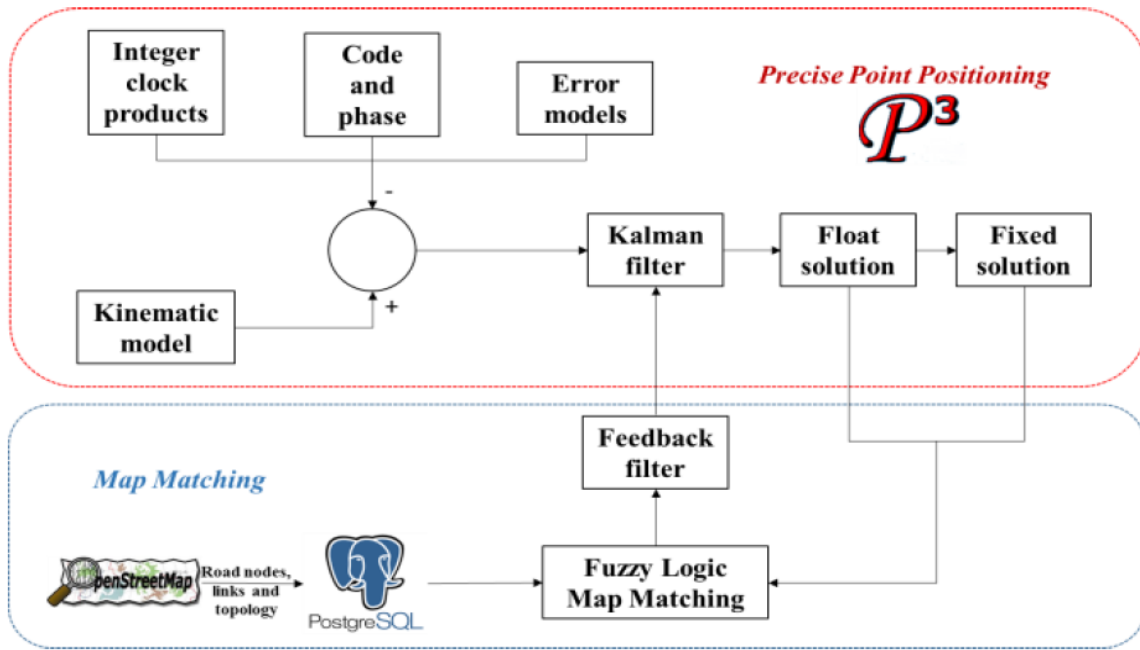


Figure 4.14 Implementation Procedure of PPP AR with the Aid of Map Matching

In this implementation, the PPP position solution is generated epoch-by-epoch. Specifically, the spectral densities for the position are set to large values, which indicates that the position needs to be estimated without any prior information at every epoch. For Map Matching implementation, OpenStreetMap (OSM) is used to provide the map information. Since the road accuracy provided by OSM is in meter level, which cannot satisfy the accuracy requirements for PPP, the OSM shape file was modified based on the RTK (Real Time Kinematic) fixed solution using QGIS software. PostgreSQL is used to manage the digital map data and PPP solutions. The road link shape files of the modified digital map are managed by PostgreSQL, and P3 software can connect to PostgreSQL for the spatial queries. The inputs for the fuzzy logic Map Matching algorithm are the PPP solution (e.g. the position, velocity, azimuth and DOP values) and the digital map information. Based on the Map Matching algorithms introduced in the previous section, the outputs of fuzzy

logic Map Matching are the map matched points and the road link azimuth, which are applied as external measurements in Kalman filter.

4.4 Summary

Fuzzy logic Map Matching utilizes the fuzzy logic to find the correct road link based on the land vehicle states (e.g. position, velocity, heading, etc.) and the digital map information. The fuzzy rules used in Map Matching and the implementation procedures are illustrated in this chapter. Map Matching can project the Stereo VO and INS integrated solution on the road link to force the trajectory back to the road link, which effectively reduces the horizontal errors. In addition, the road link azimuth can be used to reduce the heading errors as well. With the application of Map Matching, the integrated solution can be greatly improved.

The integration of GNSS PPP and Map Matching is also proposed. In open sky environment, with an accurate digital map, when the PPP float solution is projected on the road links, the map matched point coordinates and the road link azimuth can be applied as additional measurements to accelerate PPP convergence. The PPP ambiguities are correlated with the position, which means the ambiguity convergence could be accelerated as well. In this way, the integer search space will be reduced and fast PPP AR can be achieved.

Chapter Five: RESULTS AND ANALYSIS

In this chapter, the experiment results of using datasets from the field tests conducted by KITTI (Karlsruhe Institute of Technology and Toyota Technological Institute) and from the field tests conducted in Calgary are presented and analyzed. The KITTI datasets are widely applied by professionals for performance analysis with inertial and visual data synchronized better than 5 ms. The stereo images provided by KITTI are also well calibrated and rectified. The land vehicle tests were also conducted at Calgary, which include a GNSS receiver, an IMU and two cameras mounted on the roof rack attached to a land vehicle. Measurements from all sensors are synchronized and tagged with GPS time. The camera images are also calibrated and rectified. The results with KITTI and Calgary datasets are presented in Section 5.1 and Section 5.2 respectively.

5.1 Results and Analysis of KITTI Datasets

5.1.1 Data Description

In this section, the datasets collected by KITTI are used to test the tight integration of INS/Stereo VO. All the sensors are mounted on the roof of a land vehicle including a GPS/IMU unit and stereo cameras, which is shown in Figure 5.1 (A Geiger et al., 2013). The lever arms and misalignment between each sensor are accurately measured before the field test. Besides, different types of datasets (e.g. inertial measurements, images) are already synchronized and the stereo images have been well calibrated and rectified. The cameras are set at 10 FPS (Frame Per Second) and the IMU data sampling rate is 10 Hz. The GPS/IMU used is OXTS RT 3003, which is a MEMS-based IMU, and grayscale cameras are PointGrey Flea 2 (FL2-14S3M-C). The installation of the sensors is shown in Figure 5.2. The GNSS raw measurements are not provided by KITTI, therefore, there are not GNSS related test results shown in Section 5.1.



Figure 5.1 KITTI Equipment Installation (A Geiger et al., 2013)

In addition to the IMU and stereo cameras, a laser scanner and another stereo camera unit are also installed on the land vehicle roof. In this test, only the gray stereo cameras and IMU are used. The specifications of the gray camera PointGrey Flea 2 (FL2-14S3M-C) are shown in Table 5.1. The OXTS RT 3003 unit is a dual-antenna GPS/IMU system with the positioning accuracy of 0.4 m (circular error probable) with DGPS applied, the velocity accuracy of 0.05 km/h (RMS) and the heading accuracy of 0.05°(RMS) . The OXTS RT 3003 solution is used as the reference to verify the effectiveness of the proposed method in different scenarios. The acceleration bias stability of the IMU is 5 μg (1σ) and the angular rate bias stability is 36°/h (1σ). The misalignment and lever arms between each sensor are illustrated in Figure 5.2. The Cam 0 and Cam 1 are the cameras used in this thesis.

Table 5.1 Specifications of FL2-14S3M-C

Specifications	
Resolution	1384*1032
Frame Rate	Up to 15 FPS
Megapixels	1.4 MP
Chroma	Mono
Sensor Name	Sony ICX267
Sensor Type	CCD
Sensor Format	1/2"
Pixel Size	4.65 μm

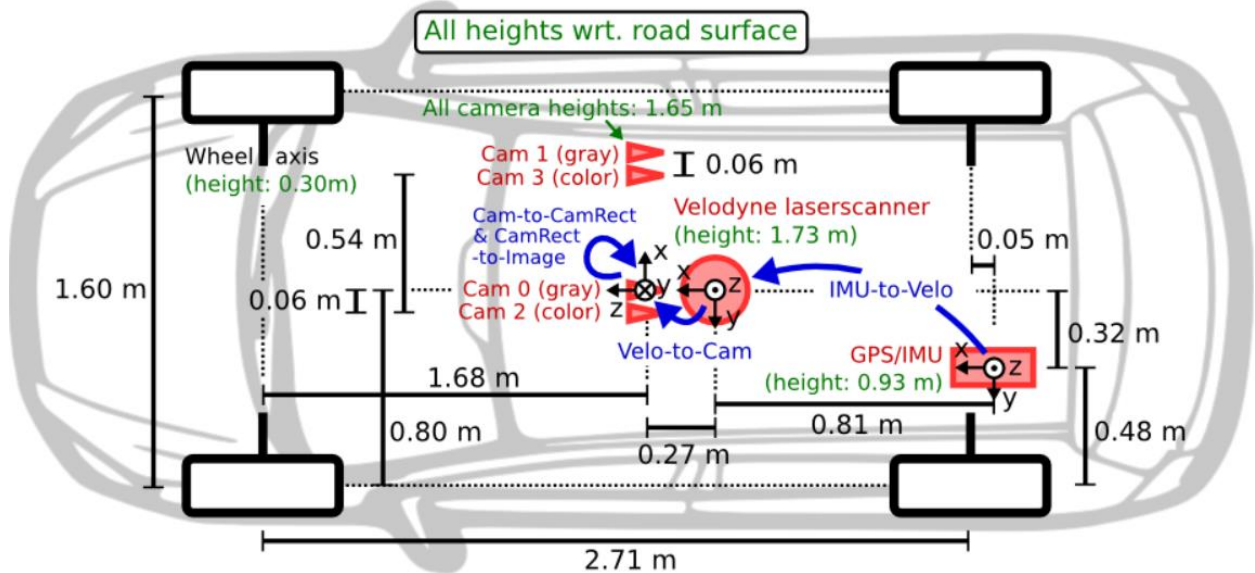


Figure 5.2 Installation Details of Each Sensor (A Geiger et al., 2013)

5.1.2 Tight Integration of INS and Stereo VO

The first dataset contains 1200 epochs (2 minutes), which was collected in a residential area with several maneuvers in the City of Karlsruhe in Germany. The distance traveled by the land vehicle is approximately 940 meters in this dataset. The test environment is shown in Figure 5.3. Stereo VO results are compared with the tight integration of INS and Stereo VO. For Stereo VO, Harris corner detector and KLT (Kanade-Lucas-Tomasi) feature tracker are used to detect and track the corresponding features between consecutive epochs. Bucketing is applied to avoid too many mismatched features and optimize the distribution of features on the image. Specifically, the image is divided into 9 rectangle parts in bucketing, and a certain number of features are randomly selected in each rectangle part. After that, the mismatched features and moving objects on the images need to be filtered out. In this work, RANSAC (RANdom SAmple Consensus) method is used to reject outliers. To be more specific, a certain number of features are randomly selected to calculate the rotation and translation between two adjacent epochs based on the resectioning model. With the calculated rotation and translation, the other features are projected on the image as well. A certain threshold is determined to define inliers and outliers. This procedure is repeated for 200 times to find out the rotation and translation with the maximum number of inlier in this epoch. In Stereo VO, the rotation and translation with respect to the first epoch can be achieved by accumulation of rotation and translation between two adjacent epochs. In the tight integration proposed in this thesis, the raw measurements of stereo images are the pixel coordinates of features detected and tracked. Sarvrood and Gao (2014) and Geiger et al. (2011) have detailed the method of Stereo VO. In addition to the Stereo VO, the Stereo VO with windowed bundle adjustment is also compared with the proposed method in this section.



Figure 5.3 Test Environment of the First Dataset

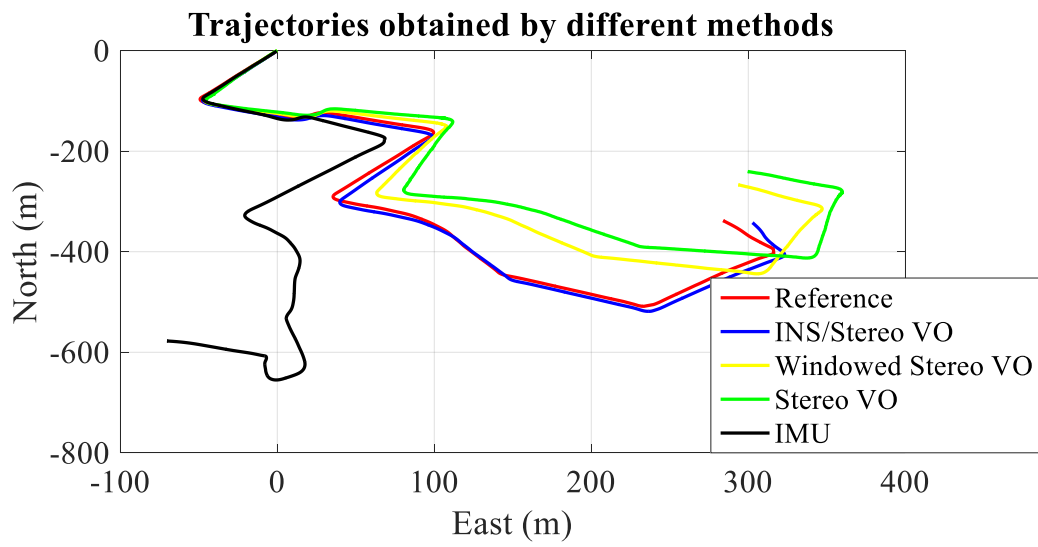


Figure 5.4 Trajectories of the First Test

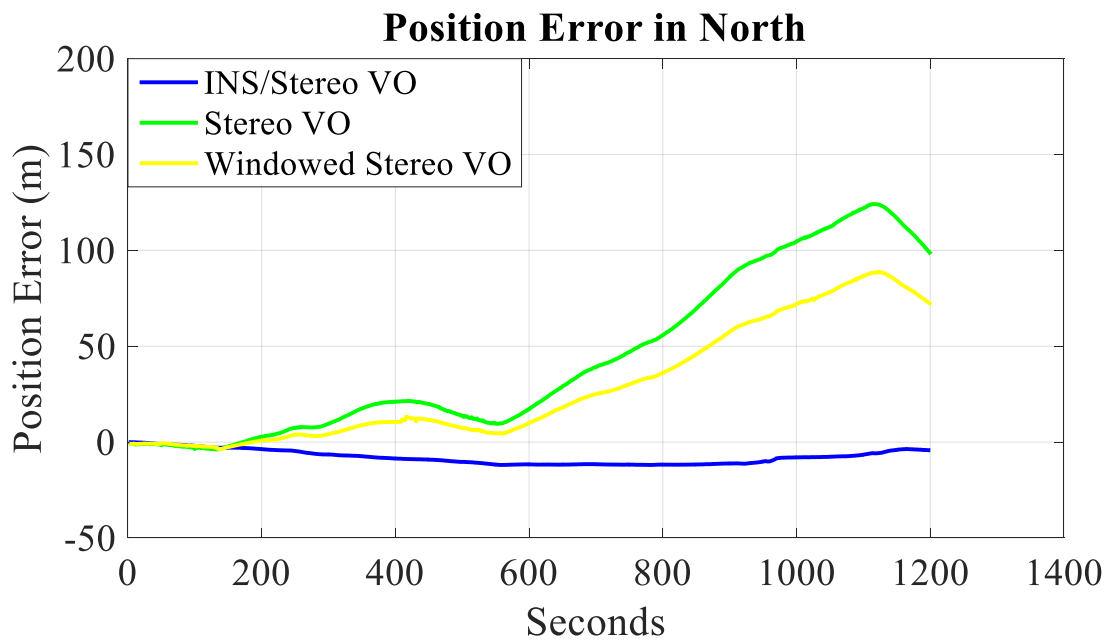
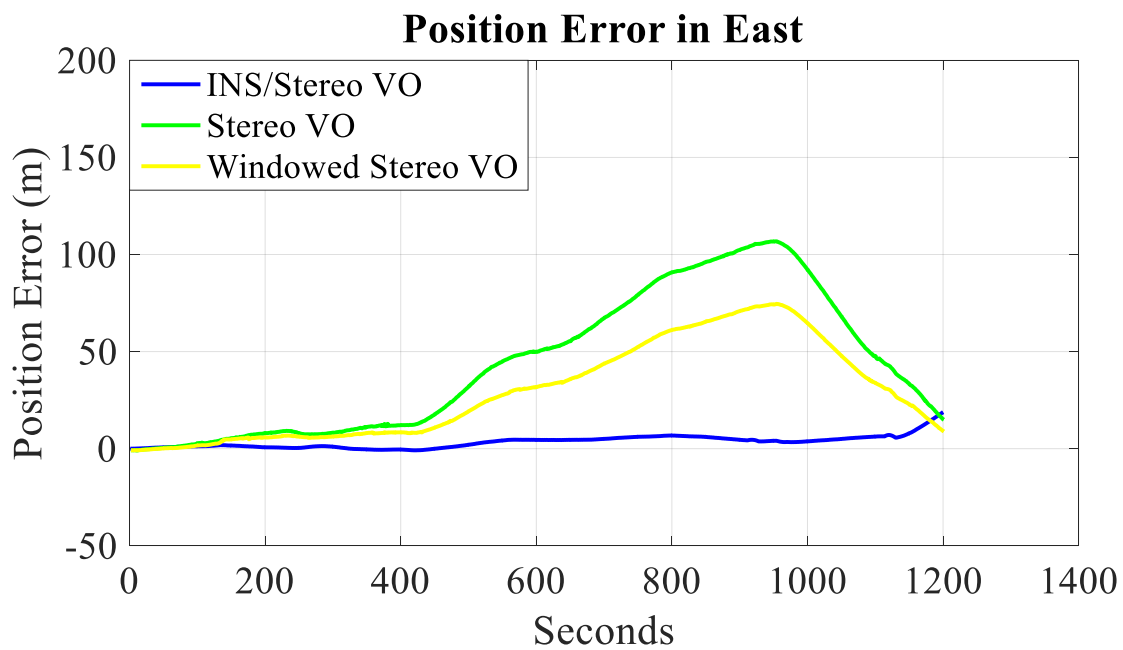




Figure 5.5 Position Error in East, North and Height

Table 5.2 Position Error RMS in East, North and Height (Unit: meter)

	East	North	Height	Horizontal	Total
INS/Stereo VO	4.704	8.619	2.066	9.819	10.0345
Stereo VO	56.916	61.507	10.651	83.474	84.151
Windowed Stereo VO	40.768	39.881	12.666	56.706	58.100
INS	160.266	100.384	15.118	188.922	189.525

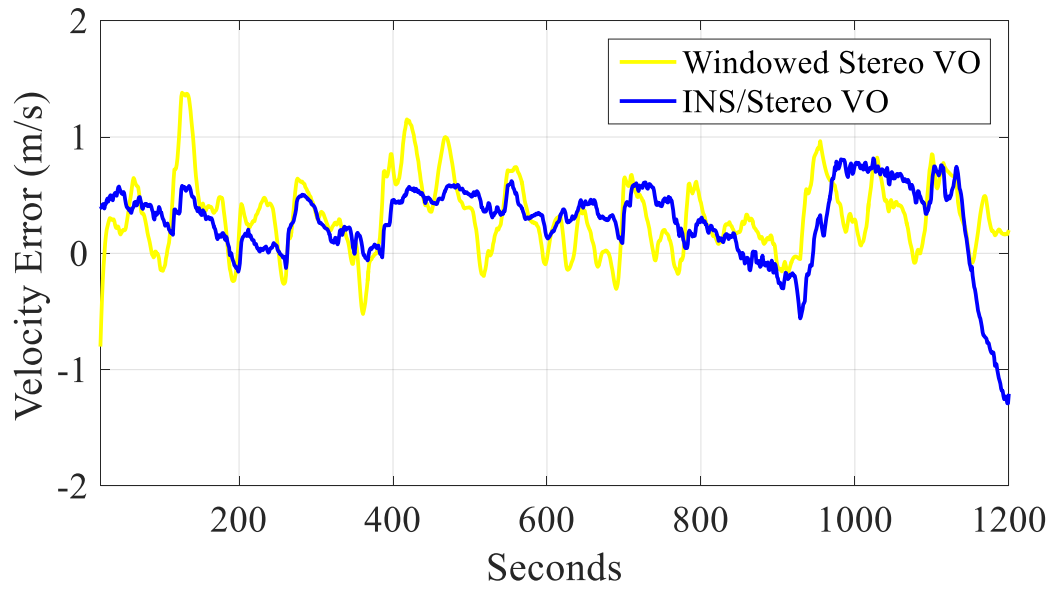


Figure 5.6 Forward Velocity Error

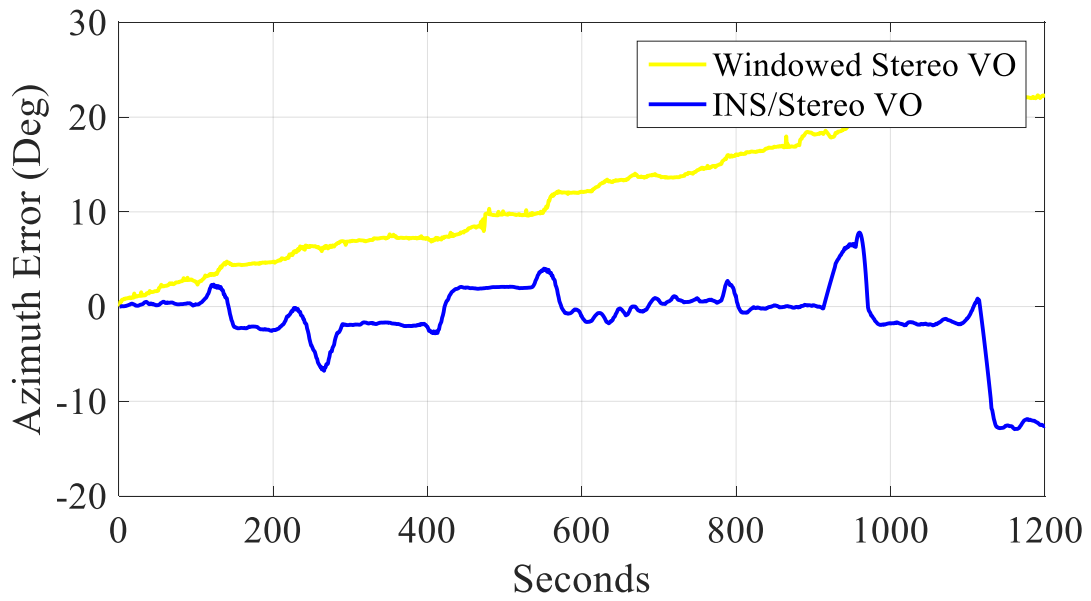


Figure 5.7 Azimuth Error

Figure 5.4 shows the trajectories obtained by different solutions using different colors. The start point is at (0, 0). It can be seen that the tight integration outperforms the other methods. The Stereo

VO adopts the same feature detection and matching strategies as in the integrated solution. Stereo VO solution drifts faster than the integrated solution. Even with windowed bundle adjustment applied, the Stereo VO performs worse than the tight integration proposed. To see the position accuracy clearly, the positioning errors of each solution are also plotted in Figure 5.5. The stand-alone IMU mechanization result is the worst (shown in Figure 5.4) and its position errors in each direction are not plotted. It is obvious that the tight integration of INS/Stereo VO has the best performance in three directions, which is less than 15 meters most times. The RMS (root-mean-square) of positioning errors using different methods is shown in Table 5.2. From Table 5.2, it can be seen that the Stereo VO and IMU mechanization results are large in each direction while the tight integration largely reduces the drift with the smallest error in every direction. Another advantage of tightly coupled integration method is that the velocity can be obtained directly. Stereo VO has to use position to calculate the velocity, and the noise of velocity is larger with this method. Usually, the velocity obtained by Stereo VO has to be processed (filtering out spikes and smoothing) before being used in other applications. Figure 5.6 shows the forward velocity errors obtained directly from the proposed method and Stereo VO. Slight improvement in the forward velocity can be achieved. The RMS of the forward velocity error obtained by the proposed method is 0.438 m/s while the RMS of the Stereo VO with windowed bundle adjustment applied is 0.449 m/s. The azimuth is much improved with the proposed method, which can be seen from Figure 5.7. The azimuth error of the proposed method is less than 10 degrees most times. Although the pixel measurements are directly related to the position and attitude, the velocity can be corrected since it is closely coupled with the position solution. Therefore, the tight integration improves not only the velocity and azimuth estimation in addition to the position solution.

To test the performance of the proposed method over a longer period, the second dataset with 5100 epochs (8.5 minutes) is applied. Similar to the first dataset, the lever arms and misalignment are measured before the data acquisition, and the stereo images are rectified and calibrated. The scenario of the second dataset is similar to the first one, which can be seen from Figure 5.8. The total distance of the second trajectory is approximately 4105 meters. The trajectories and position errors of each method are shown in Figure 5.9 and Figure 5.10 respectively. The trajectory of the tight integration is the closest one to the reference, compared with other methods. The RMS values of the positioning errors with different methods are summarized in Table 5.3. The RMS of the proposed method is only 20% of the Stereo VO in the horizontal plane. Due to much longer period, the IMU mechanization errors accumulate up to thousands of meters. The RMS of the forward velocity estimated by the integrated method is similar to the Stereo VO (0.74 m/s). As for azimuth estimation, the integrated solution is more accurate, which is one important reason for the improved position solution. The DGPS heading is not used in the integration.



Figure 5.8 Test Environment of the Second Dataset

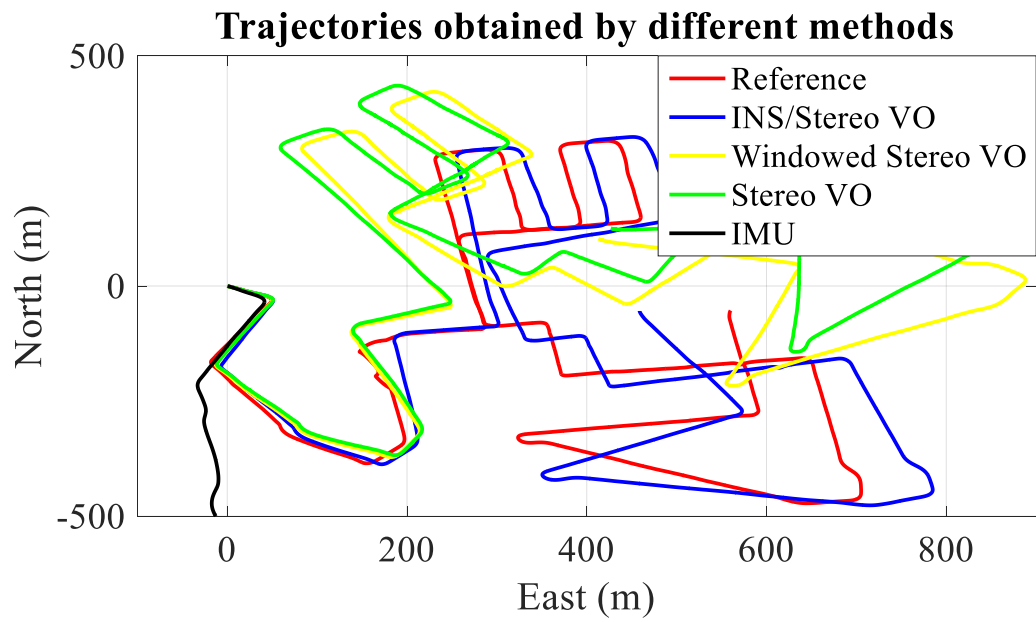
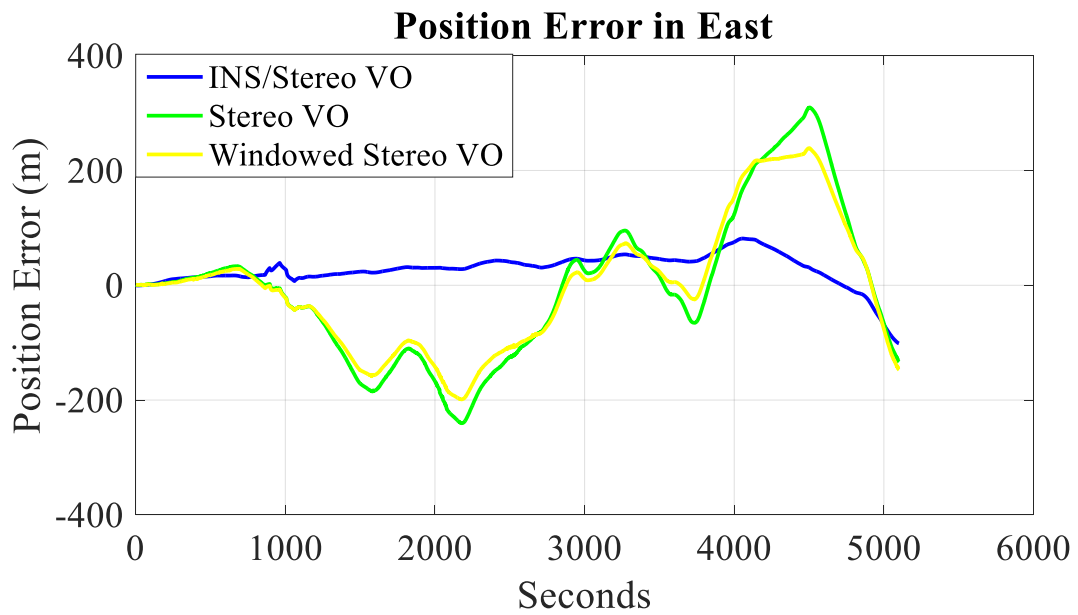


Figure 5.9 Trajectories of the Second Test



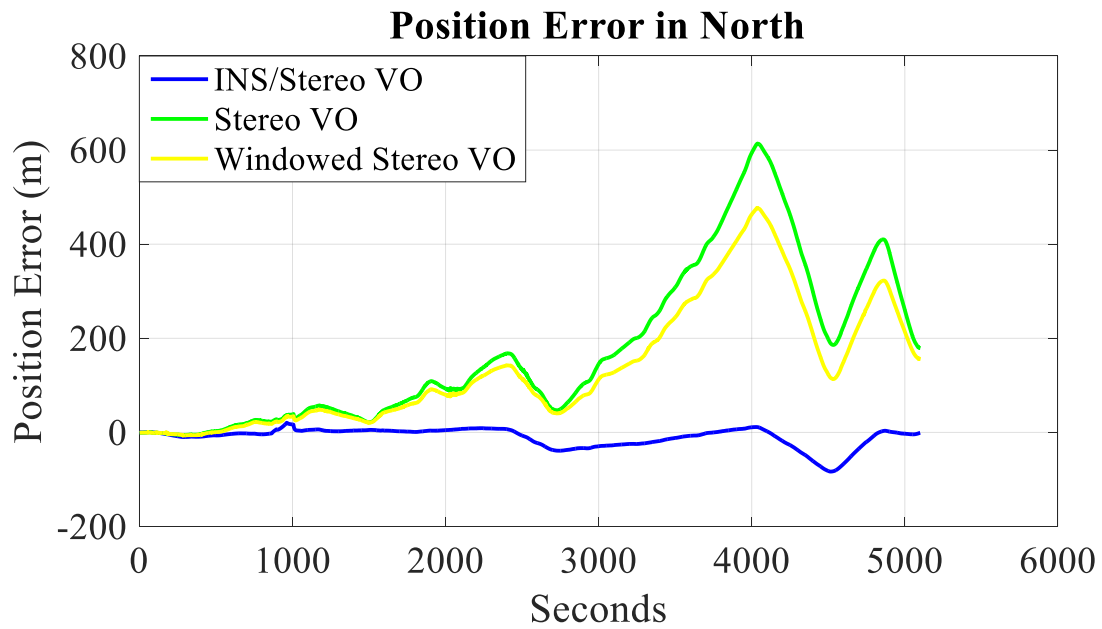


Figure 5.10 Position Error in East, North and Height

Table 5.3 Position Error RMS in East, North and Height (Unit: meter)

	East	North	Height	Horizontal	Total
INS/Stereo VO	39.319	22.847	9.638	45.475	46.486
Stereo VO	128.367	241.764	78.766	273.780	284.885
Windowed Stereo VO	111.738	188.042	21.822	218.788	219.873
INS	9140.053	6067.490	322.632	10965.131	10969.870

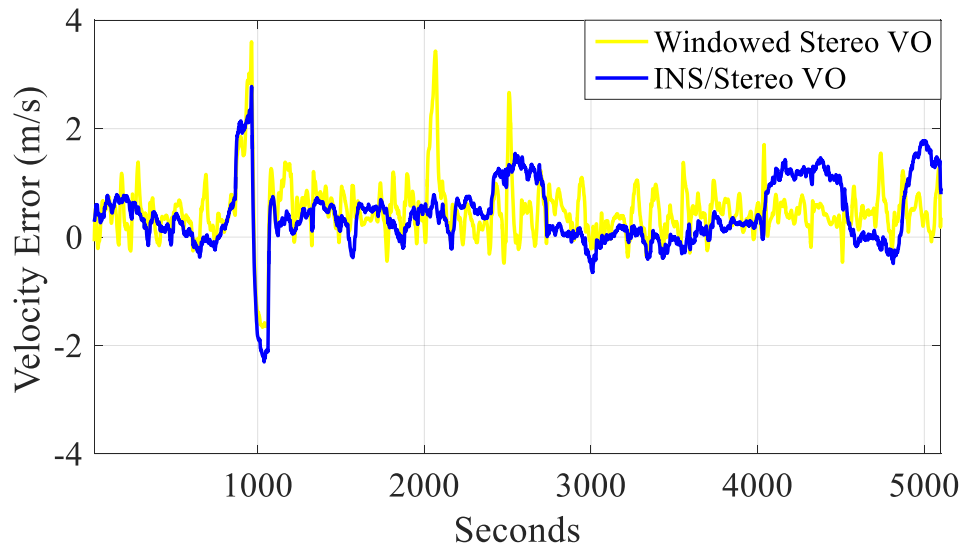


Figure 5.11 Forward Velocity Error

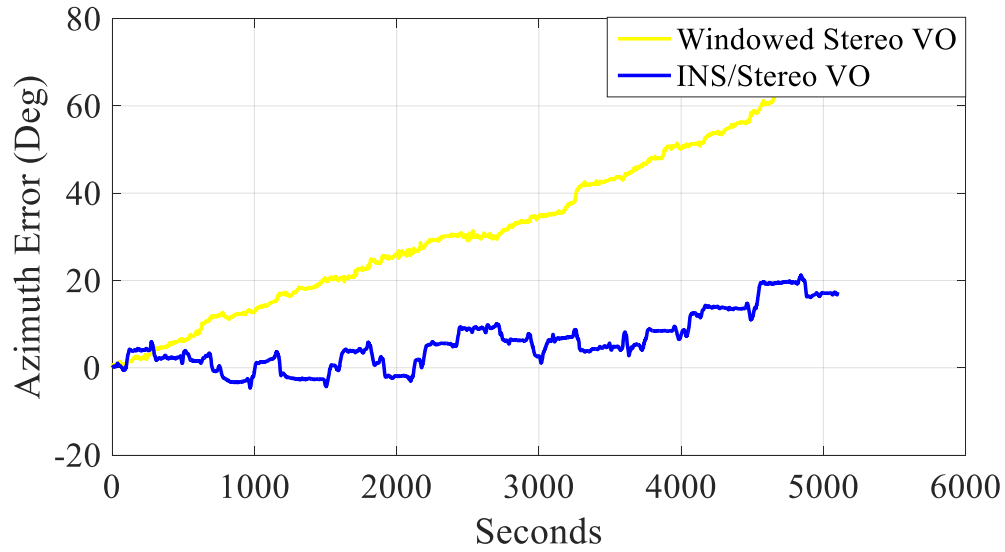


Figure 5.12 Azimuth Error

The results from both datasets demonstrate better performance using the proposed algorithm in residential areas. One more test in suburban was conducted as well. This dataset was collected on the road with trees on both sides, as shown in Figure 5.13. The traveled distance of the land vehicle is about 4980 m. The trajectories are plotted in Figure 5.14. This time, the position accuracy of the integrated solution is worse than the results from the previous two datasets. However, the integrated solution is still the best when compared to others. The Position errors in each direction are plotted in Figure 5.15, and the RMS is summarized in Table 5.4.



Figure 5.13 Test Environment of the Third Dataset

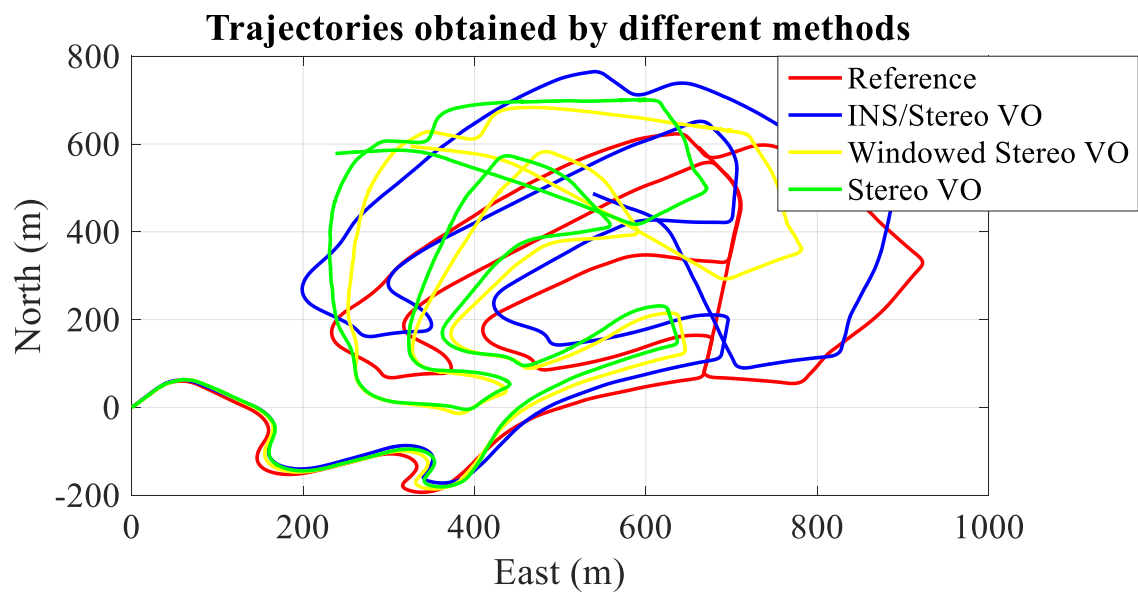


Figure 5.14 Trajectories of the Third Test

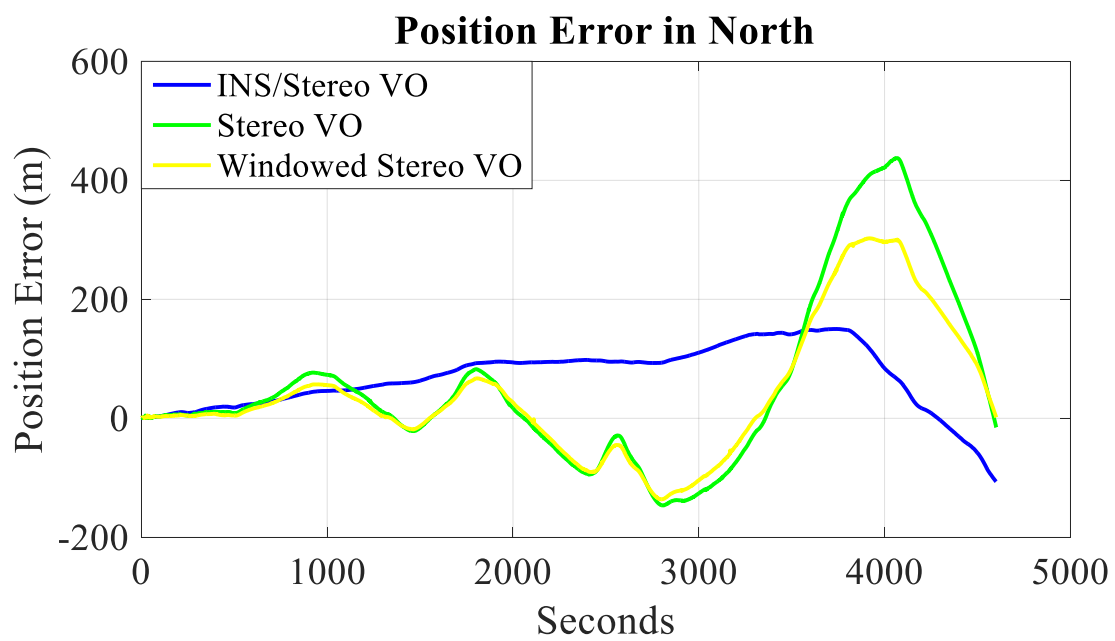
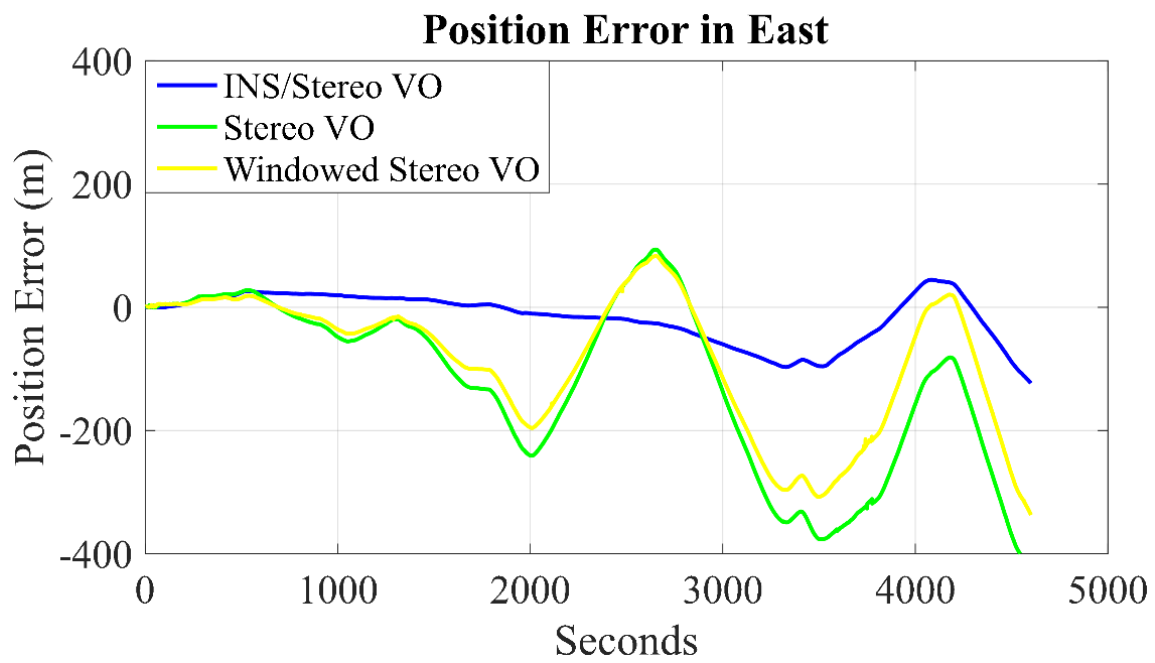




Figure 5.15 Position Error in East, North and Height

Table 5.4 Position Error RMS in East, North and Height (Unit: meter)

	East	North	Height	Horizontal	Total
INS/Stereo VO	42.806	87.338	35.060	97.264	103.390
Stereo VO	182.786	157.509	102.512	241.374	262.240
Windowed Stereo VO	138.681	117.677	62.851	182.019	192.566
INS	1199.560	1725.890	289.567	2100.406	2120.221

Table 5.5 Relative Horizontal Position Errors of Each Method

Dataset	Distance (meter)	Stereo VO	Windowed Stereo VO	INS/Stereo VO
1	940	8.88%	6.03%	1.04%
2	4105	6.67%	5.33%	1.11%
3	4980	4.85%	3.65%	1.95%

To see the horizontal position accuracy more clearly, the relative horizontal position error for each test is provided in Table 5.5. The relative horizontal position error is the horizontal error divided by the total traveled distance. It can be seen that the relative horizontal position error for all three datasets using the proposed method is less than 2%, which is much better than the Stereo VO.

5.1.3 Tight Integration of INS, Stereo VO and Map Matching

The used digital map is provided by OpenStreetMap with meter-level accuracy. The straight road link accuracy is within 4~5 meters while accuracy degrades at the maneuvers. The covariance matrix for visual measurements is based on the tracking errors of features. The map matched point is directly used as the output. The first dataset contains 5186 epochs (about 8.6 minutes), which was collected in a residential area with several maneuvers in the City of Karlsruhe in Germany. There are seldom pedestrians, bicycles and vehicles in this dataset. The average number of valid features used in this dataset is 81 per epoch. The maximum and a minimum number of valid features used are 137 and 23 respectively. The horizontal distance traveled by the land vehicle in the first dataset is approximately 4130 meters. It has been proved that the tightly coupled integration of INS and Stereo VO outperforms the individual sensor in the previous section. Thus,

only the reference trajectory, tightly coupled INS/Stereo VO and INS/Stereo VO/MM are plotted in red, green and blue respectively in Figure 5.16. As can be seen, it is inevitable that the INS/Stereo VO suffers drift after a certain time. The Map Matching forces the solution to project on the road link when the correct road link can be determined. In this way, the position information of the map matched point is utilized in the INS/ Stereo VO system. This is also the reason that the INS/Stereo VO/MM trajectory is not continuous since the trajectory is forced to the road link. It might cause incorrect Map Matching when the land vehicle is turning. With the algorithms used in this thesis, it is obvious that there is no Map Matching point when the land vehicle is turning. This is due to the uncertainty of the road link determination in SMP-2 and the feedback filter conditions in the Map Matching. The RMS values of the positioning error in each direction are shown in Table 5.6. It can be seen that the RMS in the horizontal plane is largely reduced after the application of Map Matching algorithms.



Figure 5.16 Trajectories of the First Dataset for Map Matching

Table 5.6 Positioning Error RMS for the First Dataset (Unit: meter)

	East	North	Height	Horizontal	Total
INS/Stereo VO	52.720	23.308	9.621	57.642	58.440
INS/VO/MM	11.588	8.109	12.522	14.144	18.891

In addition to the improvement in position, the azimuth and velocity estimation has also been improved. The digital map azimuth is used in INS mechanization after Map Matching. The RMS of azimuth error with Map Matching feedback is reduced from 8.03 degree to 5.01 degree. With

the improvements in position and azimuth, the velocity estimation is slightly better as well. The RMS of the forward velocity error is decreased from 1.49 m/s to 1.05 m/s.

The second dataset was collected in suburban with trees on both sides. The distance of this dataset is about 4980 meters. At the beginning of the dataset, not enough valid features can be tracked due to similar scenes with trees along the road. In two epochs, no valid visual measurements can be used, which means only mechanization results of IMU is provided for Map Matching. Averagely, 84 valid features are used in each epoch in this test. The trajectories are plotted in Figure 5.17, and the position error RMS is provided in Table 5.7. The horizontal accuracy is greatly improved with the application of Map Matching while the height accuracy keeps the same level. This is due to the 2D digital map used can only provide horizontal position information. Since the digital map can provide the azimuth, the azimuth error is reduced from 7.15 degrees to 4.12 degrees. With the improvement of azimuth estimation, the velocity estimation is also slightly improved.

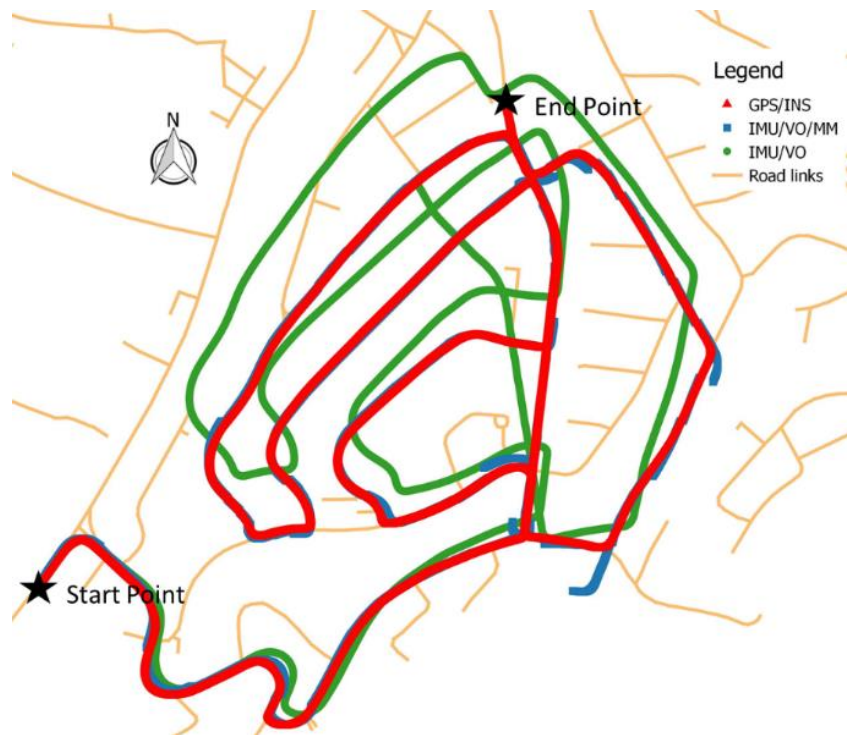


Figure 5.17 Trajectories of the Second Dataset for Map Matching

Table 5.7 Positioning Error RMS for the Second Dataset (Unit: meter)

	East	North	Height	Horizontal	Total
INS/Stereo VO	34.639	69.681	32.296	77.816	84.252
INS/VO/MM	7.579	17.293	33.373	18.881	38.344

The third dataset contains 2761 epochs (around 4.6 minutes). The distance of the third test is about 2206 meters. Averagely, there are 78 features used in each epoch. The maximum number of inliers of visual measurements is 138 while the minimum number is 25. There are almost no moving objects in this dataset. The trajectories of each method are plotted in different colors shown in Figure 5.18. The trajectory with the Map Matching feedback is not continuous like the previous tests. The RMS values of the positioning errors with different methods are provided in Table 5.8. It can be seen that the horizontal accuracy is much improved with the application of Map Matching. The RMS is reduced from over 50 meters to less than 10 meters. Similarly, the azimuth error decreased from 8.68 degrees to 2.29 degrees, and the horizontal velocity error is reduced from 1.435 m/s to 0.719 m/s.

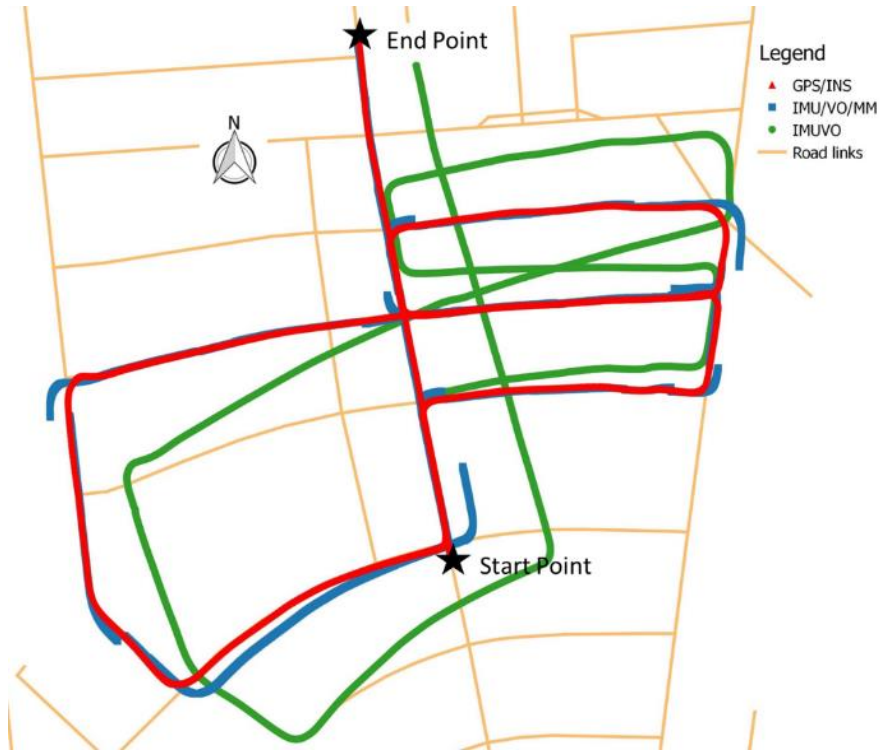


Figure 5.18 Trajectories of the Third Dataset for Map Matching

The Map Matching method used in this paper would not improve the estimation of the height component since the digital map can only provide horizontal information. For all the datasets, the positioning error in height is higher when applying INS/Stereo VO/MM. The reason for this might be that only the horizontal coordinates of map matched point are used while other states (velocity and attitude) keep the same, resulting in little improvement in velocity. With no height information and the velocity is not too much improved, the height error stays the same. However, the height accuracy is not the concern in this case since the horizontal position is more important for land vehicle navigation.

The relative horizontal errors of all three datasets of each solution are listed in Table 5.8. As expected, the tightly coupled integration with no Map Matching has the largest relative horizontal

position error for the third dataset while INS/Stereo VO/MM solution provides more accurate and stable performance with relative horizontal position error less than 0.4% in each case.

Table 5.8 Positioning Error RMS for the Thrid Dataset (Unit: meter)

	East	North	Height	Horizontal	Total
INS/Stereo VO	40.471	31.299	5.587	51.162	51.466
INS/VO/MM	7.814	3.358	7.832	8.505	11.562

Table 5.9 Relative Horizontal Positioning Errors of Different Methods

Dataset	Distance (meter)	INS/Stereo VO	INS/VO/MM
1	4130	1.40%	0.34%
2	5061	1.54%	0.37%
3	2206	2.32%	0.39%

5.2 Results and Analysis of Calgary Datasets

In addition to the KITTI datasets, we also conducted field tests in Calgary to verify the methods developed in this thesis. The sensors used in the field tests are shown in Figure 5.19. The GNSS receiver, IMU and cameras used are Trimble R10, Crossbow NAV440 and PointGrey CM3-U3-13Y3M-CS respectively. Trimble R10 is a survey grade receiver capable of RTK and high-frequency output. In the implementation in this thesis, only one Trimble R10 receiver is used to conduct PPP with the data rate at 1 Hz. Crossbow NAV440 is a MEMS-based IMU with an internal GPS receiver. The gyro bias stability in run is 10 deg/h and the bias stability over temperature is

0.02°/s. The accelerometer bias stability in run is 1mg and the bias stability over temperature is 4 mg. In this implementation, data rate for Crossbow NAV440 is 100 Hz. PointGrey CM3-U3-13Y3M-CS is an industrial camera with a global shutter. The details of the camera specifications are shown in Table 5.10. In the implementation, 10 FPS is used. The lenses mounted on the cameras are Fujinon DV3.4x3.8SA-1. The focal length is 3.8mm-13mm and the optical format is 1/2".



Figure 5.19 Sensors in the Field Tests

All the sensors are mounted on a rack installed on the roof of a land vehicle. The Trimble R10 receiver, the IMU and the left camera are mounted close to each other. The lever arms between them are neglected. The baseline between two cameras is about 80 cm. The installation of each sensor on the roof can be seen from Figure 5.20. The Trimble R10 receiver has one internal battery that can last for several hours. The Crossbow NAV440 IMU needs to be connected to external power source. The PointGrey CM3-U3-13Y3M-CS cameras can be powered by laptop through USB 3.0 cables.

Table 5.10 PointGrey CM3-U3-13Y3M-CS Specifications

Specifications

Resolution	1280*1024
Frame Rate	Up to 149 FPS
Megapixels	1.3 MP
Chroma	Mono
Sensor Name	ON Semi PYTHON 1300
Sensor Type	CMOS
Sensor Format	1/2"
Pixel Size	4.8 μm



Figure 5.20 Installation of Sensors

5.2.1 Test Preparation

Before the field tests, the sensors used need to be set up properly including the synchronization of all sensors, the stereo camera settings, the stereo camera calibration and rectification. Since different types of measurements are fused into one filter, they need to be synchronized first. The

exact setting and synchronization of the stereo cameras are of great importance in Stereo VO because the 3D objects have to be projected on the stereo images in the same way. Otherwise, the feature tracking, correct triangulation and rectification in Stereo VO would be impossible. The camera calibration and rectification are also required because the Stereo VO models introduced in Chapter 2 would be invalid with distorted images applied in the Stereo VO.

5.2.1.1 System Synchronization

For the integrated system, one of the most important things is the synchronization of all the sensors. In our implementation, all sensors are synchronized to GPS time. The GNSS measurements from Trimble R10 are tagged with GPS time. The Crossbow NAV440 IMU has an internal GPS receiver which enables the inertial measurements to be tagged with GPS time. Here the difference between the receiver clocks in Trimble R10 and Crossbow NAV440 is small enough (less than 0.5 ms) that they can be safely neglected. For the PointGrey cameras, firstly, the two cameras need to be synchronized together to capture images simultaneously. Secondly, the images captured by the two cameras have to be tagged with GPS time, in order to be integrated with other types of measurements in Kalman filter. Apart from the USB port on the camera, there is a 9-pin General-Purpose Input/ Output (GPIO) port, which can be used to send or receive trigger signals. The GPIO port on the camera is shown in Figure 5.22. The functions of each pin of the GPIO port can be seen in Figure 5.23. In the implementation, an Ublox M8T receiver is used to trigger the stereo cameras to capture images at the same time. Ublox M8T can send up to 10M Hz time-pulse signals to trigger external sensors. The stereo cameras are triggered by the same time-pulse signals from the Ublox M8T receiver. In this way, not only the synchronization of two cameras can be guaranteed, but also the images are synchronized with GPS time. When the camera is set in the

trigger mode, the camera starts capturing images from external trigger input falling/rising edge. The camera can be triggered in this mode by using the GPIO pins as an external trigger or by using a software trigger. In our implementation, the external trigger input is from the Ublox M8T receiver. M8T is used to trigger the cameras instead of Trimble R10 is due the capability of M8T to send scalable frequency signals. The synchronization procedure can be seen from Figure 5.21. It can be seen from the figure that the exposure duration also affects the time that images are taken. Therefore, the exposure duration should be as short as possible.

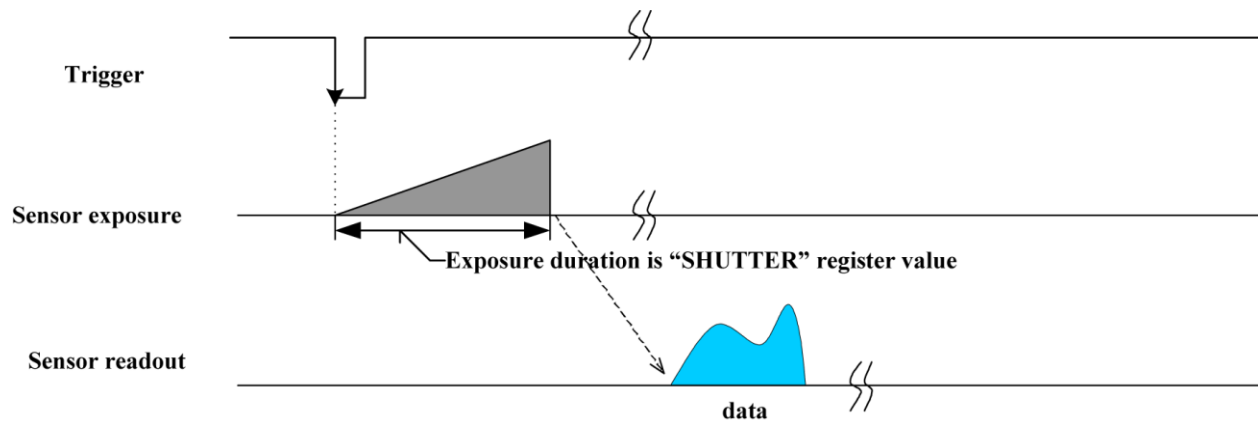


Figure 5.21 PointGrey Camera Trigger Mode (FLIR Knowledge Base, 2017)

The other issue is the time tag of each image taken by the cameras. The FlyCapture Software Development Kit (SDK) provides basic functions for PointGrey cameras, e.g. trigger, strobe, time tag, etc. When the stereo cameras are connected to a laptop with USB 3.0 cables, the laptop UNIX time can be assigned to each image captured. The UNIX time is defined as the seconds that have elapsed since 00:00:00 Coordinated Universal Time (UTC), Thursday, 1 January 1970, minus the leap seconds that have taken place since them. In other words, the images can be tagged with UTC time provided by the laptop. However, as we know, the laptop clock is not accurate in most cases. If the laptop cannot access the Internet, the error of laptop time can be up to several seconds. To

solve this problem, the Ublox receiver is not only used to trigger the cameras, GPS time of the Ublox receiver is also recorded on the laptop connected to the cameras. Meanwhile, the laptop time is recorded at the same time. In this way, the time gap between GPS time and the laptop time can be known. Therefore, the image time tags can be converted to GPS time. In this way, all the sensor measurements are tagged with GPS time. The method used to record the Ublox receiver GPS time is to decode the measurements of the receiver. There is a 50 ~ 150 ms delay receiving and decoding the GNSS measurements compared with the time-pulse signals. 100 ms is subtracted when recording the GPS to compensate for the delay.



Figure 5.22 GPIO Port on PointGrey CM3-U3-13Y3M-CS

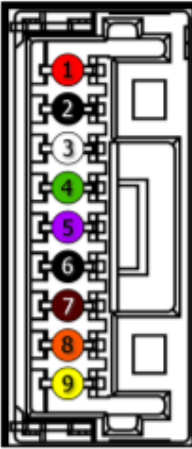
Diagram	Color	Pin	Function	Description
	Red	1	V_{EXT}	Allows the camera to be powered externally 5 - 24 VDC
	Black	2	GND	Ground for Input/Output, V_{EXT} , +3.3 V pins
	White	3	+3.3 V	Power external circuitry fused at 150 mA maximum
	Green	4	GPIO3 / Line3	Input/Output/Tx
	Purple	5	GPIO2 / Line2	Input/Output/Rx
	Black	6	GND	Ground for Input/Output, V_{EXT} , +3.3 V pins
	Brown	7	OPTO_GND	Ground for opto-isolated IO pins
	Orange	8	OPTO_OUT / Line1	Opto-isolated output
	Yellow	9	OPTO_IN / Line0	Opto-isolated input
To configure the GPIO pins, consult the General Purpose Input/Output section of your camera's Technical Reference Manual.				

Figure 5.23 Functions of the 9-pin GPIO Port on PointGrey CM3-U3-13Y3M-CS (FLIR Knowledge Base, 2017)

The field test setup is illustrated in Figure 5.24. A laptop is used to record the inertial measurements and the images. When the Crossbow NAV440 is connected to a GPS antenna, it can work independently, and the inertial measurements are time tagged with GPS time. The IMU is powered up by an external power box and the inertial measurements are recorded by the laptop connected to the IMU. The Trimble R10 receiver can work by itself with its own internal antenna and battery. The Ublox M8T plays two roles here. Firstly, it sends out 10 Hz time-pulse signals to trigger the stereo cameras to take images at the same time and synchronize the images with GPS time. Secondly, it provides the time gap between the laptop time and GPS time in order to tag the images with GPS time. When the stereo cameras are triggered, they capture the images at the same time, and the images are saved by the laptop.



Figure 5.24 Field Test Setup

5.2.1.2 Camera Settings

The settings (e.g. Brightness, Exposure, Sharpness, Gamma, Shutter, Gain, etc.) should be exactly the same for the stereo cameras to take the same images to the largest extent. The PointGrey cameras provide auto modes for some settings. For example, the shutter and exposure can be set as an automatic mode to obtain the best images in the current situation. However, such optimized functions should be turned off when taking stereo images since the automatic mode cannot guarantee the same settings for both cameras at the same time. The slight difference might lead to degradation of Stereo VO results. For example, if the shutters for two cameras are different, the

times that the cameras take images may not be the same since the trigger time is the same, but shutters could take unequal time. The camera settings for the field tests are shown in table 5.11.

Table 5.11 Camera Settings for Field Tests

Property	Value	Auto Mode
Sharpness	1024 (default)	OFF
Shutter	7 ms	OFF
Gain	5 dB	OFF
GAMMA	1	OFF
Brightness	17%	OFF
Auto Exposure	0	OFF

One thing needs to be mentioned is that a buffer is needed to save the images during tests. This is to prevent the loss of images during the tests due to the large size of data storage. For instance, one raw image is about 1.25 M so 10 FPS with two cameras make the total size 25M/s. Therefore, a buffer is necessary to make the captured images first queue in the buffer before saving in case loss of images during the tests. All the images taken during the tests are in binary format in order to reduce the image storage size.

5.2.1.3 Calibration and Rectification

The Visual Odometry equations introduced in Section 2.3.2 (e.g. Eq (2.31) and Eq (2.33)) are based on the assumption that all the images used are not distorted. However, it is inevitable that distorted images are captured using industrial cameras in applications. Therefore, to apply VO algorithms, the first thing to do is to correct the distorted images. This can be done by estimating

the parameters of the camera lens (Bradski & Kaehler, 2008; Heikkila & Silven, 1997; Zhang, 2000). Generally, the distortion consists of the radial distortion and the tangential distortion. The radial distortion is most visible with straight lines appearing curved, as shown in Figure 5.25. The radial distortion can be modeled as Eq (5.1),

$$\begin{aligned} x_{undistorted} &= x_{distorted} + (x_{distorted} - u)(1 + k_1 r^2 + k_2 r^4 + k_3 r^6) \\ y_{undistorted} &= y_{distorted} + (y_{distorted} - v)(1 + k_1 r^2 + k_2 r^4 + k_3 r^6) \end{aligned} \quad (5.1)$$

where $(x_{undistorted}, y_{undistorted})$ is the undistorted image point used in Eq (2.31), $(x_{distorted}, y_{distorted})$ is the distorted imaged point as captured on the image, (u, v) is the principal point pixel coordinate, k_1, k_2 and k_3 are the radial distortion coefficients, $r = \sqrt{(x_{distorted} - u)^2 + (y_{distorted} - v)^2}$.

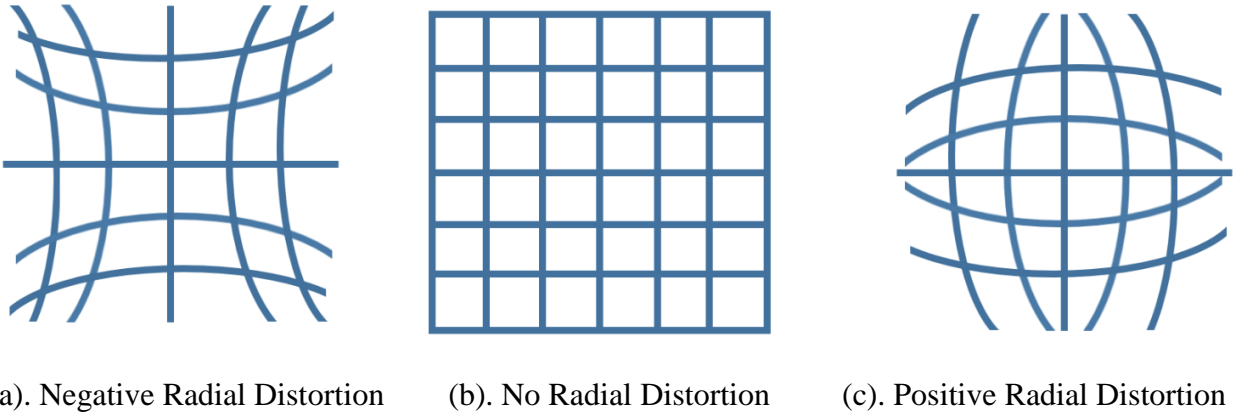


Figure 5.25 Radial Distortion (Mathworks Documentation, 2017)

The tangential distortion occurs if the camera lens and the sensor format are not parallel as shown in Figure 5.26. The tangential distortion can be modeled in Eq (5.2).

$$\begin{aligned} x_{undistorted} &= (p_1(r^2 + 2(x_{distorted} - u)^2) + 2p_2(x_{distorted} - u)(y_{distorted} - v))(1 + p_1 r^2 + p_2 r^4 + p_3 r^6) \\ y_{undistorted} &= (2p_1(x_{distorted} - u)(y_{distorted} - v) + p_2(r^2 + 2(y_{distorted} - v)^2))(1 + p_1 r^2 + p_2 r^4 + p_3 r^6) \end{aligned} \quad (5.2)$$

where $u, v, r, (x_{undistorted}, y_{undistorted}), (x_{distorted}, y_{distorted})$ have the same meaning in Eq (5.1), p_1, p_2 and p_3 are the tangential distortion coefficients.

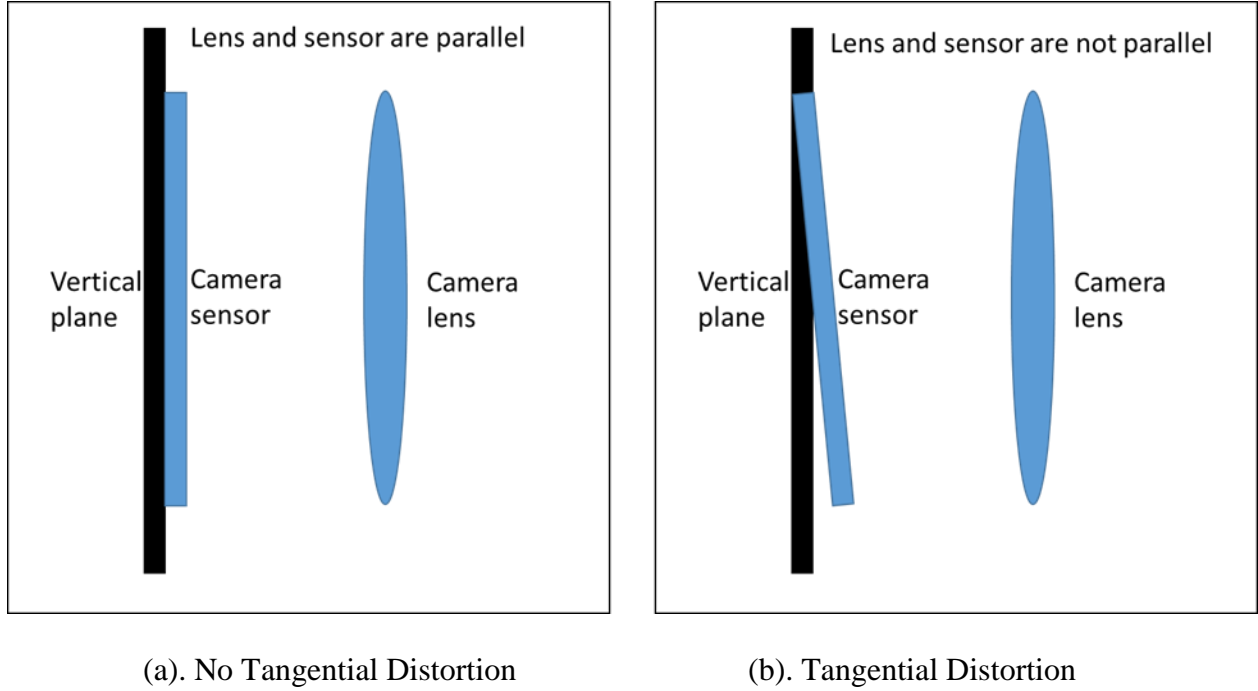


Figure 5.26 Tangential Distortion

Combining Eq (5.1) and Eq (5.2), the calibration model can be written as

$$\begin{aligned}
 x_{undistorted} &= (p_1(r^2 + 2(x_{distorted} - u)^2) + 2p_2(x_{distorted} - u)(y_{distorted} - v))(1 + p_1r^2 + p_2r^4 + p_3r^6) \\
 &\quad + (p_1(r^2 + 2(x_{distorted} - u)^2) + 2p_2(x_{distorted} - u)(y_{distorted} - v))(1 + p_1r^2 + p_2r^4 + p_3r^6) \\
 y_{undistorted} &= (2p_1(x_{distorted} - u)(y_{distorted} - v) + p_2(r^2 + 2(y_{distorted} - v)^2))(1 + p_1r^2 + p_2r^4 + p_3r^6) \\
 &\quad + (2p_1(x_{distorted} - u)(y_{distorted} - v) + p_2(r^2 + 2(y_{distorted} - v)^2))(1 + p_1r^2 + p_2r^4 + p_3r^6)
 \end{aligned}
 \tag{5.3}$$

The Least Square method can be used to estimate the unknowns in Eq (5.3). Eq (2.31) is used to calculate the undistorted point $(x_{undistorted}, y_{undistorted})$. Therefore, the 3D coordinates of objects should be known and the projection on the image should be easily distinguished, which makes the

chessboard a good pattern for camera calibration. There are two camera calibration methods using the chessboard. The first one is to capture multiple chessboards in a single shot (Geiger et al., 2012) and the second one is to capture multiples images of one chessboard with different locations (Laganière, 2017). In this thesis, the second method is used, and the chessboard is captured from different views, shown in Figure 5.28. The total number used for camera calibration is 54. Here only parts of the images are shown. In the calibration, the chessboard was placed at 2~10 meters away from the cameras from different views.

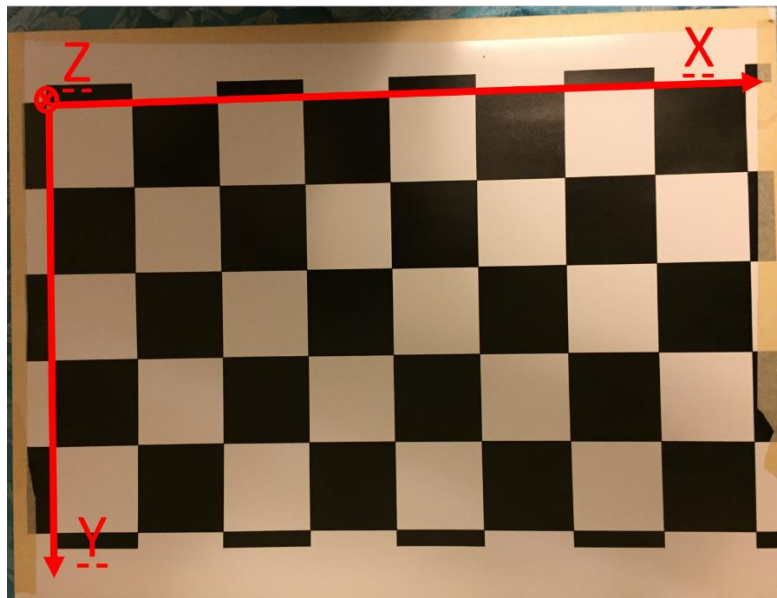


Figure 5.27 Chessboard for Camera Calibration

The valid chessboard size is 6 by 3 squares with each square side 6.9 cm. The chessboard is attached to a flat surface, which is shown in Figure 5.27. In Figure 27, the left-up corner is selected as the origin of the world frame. The X axis and Y axis lie on the chessboard plane while the Z axis is perpendicular to the chessboard plane. The 3D coordinates of each detected corners are easy to be determined since the world frame is based on the chessboard plane. It can be seen that the

projected point of each corner can be easily detected on the image and the projected point pixel coordinates namely $(x_{distorted}, y_{distorted})$ can be known. With multiple images taken from different views, multiple equations based on Eq (2.31) and Eq (5.3) can be set up. The unknowns k_i, p_i, u, v, f can be estimated.



Figure 5.28 Images for Camera Calibration

For stereo camera calibration, two cameras need to capture the same chessboard at the same time. In addition to the unknowns in single camera calibration, the rotation and translation between two cameras are also included in the estimation. The next step after stereo calibration is stereo

rectification, which transforms the stereo image planes on the same plane paralleling to the baseline between two cameras (Bradski & Kaehler, 2008; Forsyth & Ponce, 2011; Hartley & Zisserman, 2003). After stereo rectification, epipolar lines become collinear and parallel to baseline as well. Shown in Figure 5.29 is the rectified and calibration stereo images. The rectified and calibrated images are used in the Stereo VO, which makes the tracking between left and right images in consecutive epochs easier. More importantly, the equations introduced in Section 2.3.2 can be applied after stereo calibration and rectification.

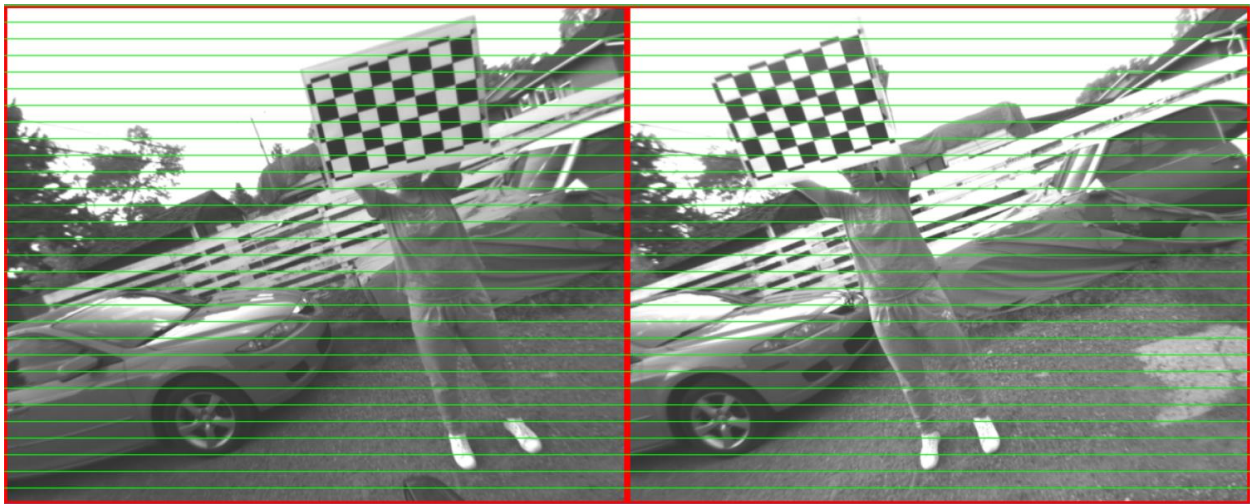


Figure 5.29 Stereo Images After Rectification

5.2.2 Tight Integration of INS and Stereo VO

The first test was in the Triwood community near the University of Calgary. The test lasted for about three and half minutes. It started with the point (0, 0). There are trees and houses along the roads. The general test environment can be seen in Figure 5.30. During the test, the land vehicle made four maneuvers.



Figure 5.30 First Test Environment

The trajectories of stand-alone Stereo VO and tightly coupled INS/Stereo VO are plotted in green and blue respectively in Figure 5.31. The meter level GPS standard point positioning (SPP) result is used as the reference. The horizontal accuracy is within 5 meters, which is good enough to evaluate the positioning results of the DR systems used in this thesis since all the DR systems suffer accuracy degradation over 20 meters. The reference trajectory is plotted in red in Figure 5.31. In this implementation, the windowed bundle adjustment of Stereo VO is not applied. The Stereo VO results are obtained by triangulation and resection at every single epoch. RANSAC is applied to filter out obvious outliers of the tracked features. Specifically, RANSAC is applied to find out the rotation and translation with the maximum number of inliers within a certain threshold (7 pixels). Features are randomly selected to calculate the rotation and translation for 200 times. Based on the calculated rotation and translation, the other features are projected on the images.

Those with projection error larger than the threshold are rejected. The calculation with the most inliers is treated as the resectioning results of Stereo VO, and the inliers on the images are used for the tightly coupled integration. In other words, the visual measurements used in the stand-alone Stereo VO and the tightly coupled integration are the same. In this way, if the tightly coupled integration method result is better, it is proved that the integration has an effect on position accuracy improvement.

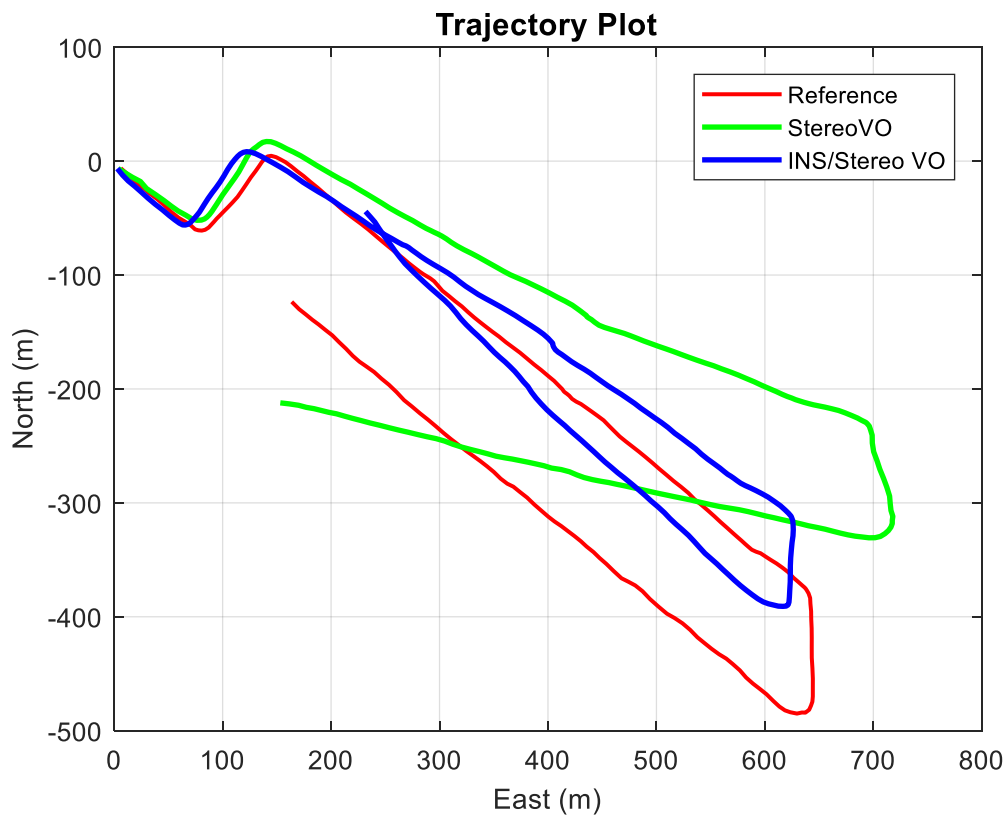
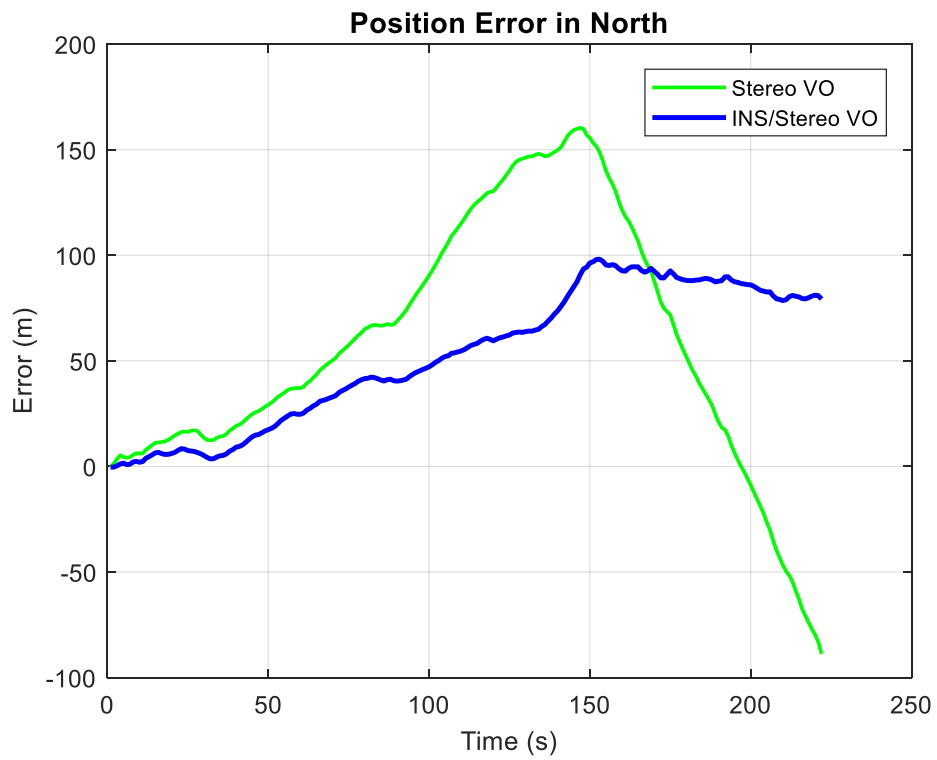
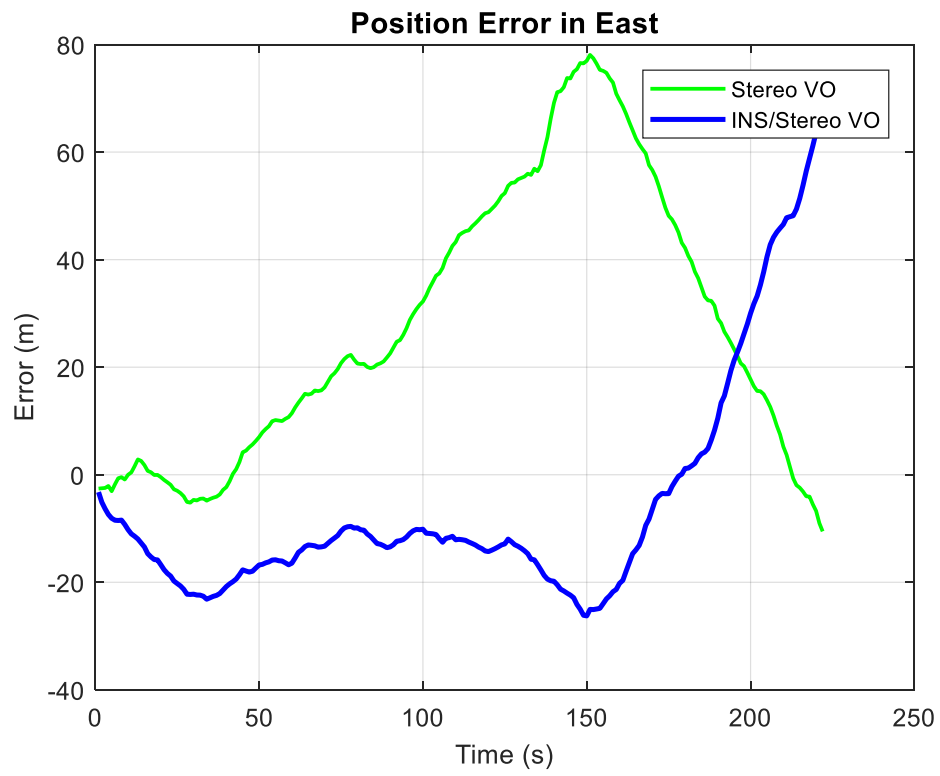


Figure 5.31 Trajectory of the First Test

From Figure 5.31, it can be seen that the stand-alone Stereo VO drifts more than the tightly coupled INS/ Stereo VO system. The integration results follow the correct trajectory for longer time. The result of the stand-alone INS is not provided in Figure 5.31 since the IMU mechanization results

drift quickly after beginning. To see the positioning results more clearly, the positioning errors of each system are shown in Figure 5.32. The moving direction was changed at 150 s, which reduces the Stereo VO error while increases the INS/Stereo VO error. The RMS values of the positioning errors are summarized in Table 5.12. For this dataset, the tightly coupled integration of INS and Stereo VO proposed in this thesis outperforms the stand-alone Stereo VO in all directions, which verifies the effectiveness of the proposed method. As explained in Chapter 4, the dynamic information provided by IMU improves the results of the stand-alone Stereo VO. The IMU position and attitude are used to predict the pixel coordinates of features on the next image. In this way, the IMU information is fused in the filter. With closed-loop method used, the IMU mechanization errors are corrected, which maintains the dynamic information of IMU within certain accuracy. Compared with the stand-alone IMU solution, the pixel coordinates corrections provided by the Stereo VO correct not only the IMU mechanization position but also the velocity and attitude. Due to the correction of the velocity, the accumulation of position error is not as fast as the stand-alone IMU. This is the main reason the integration greatly improves the mechanization results.



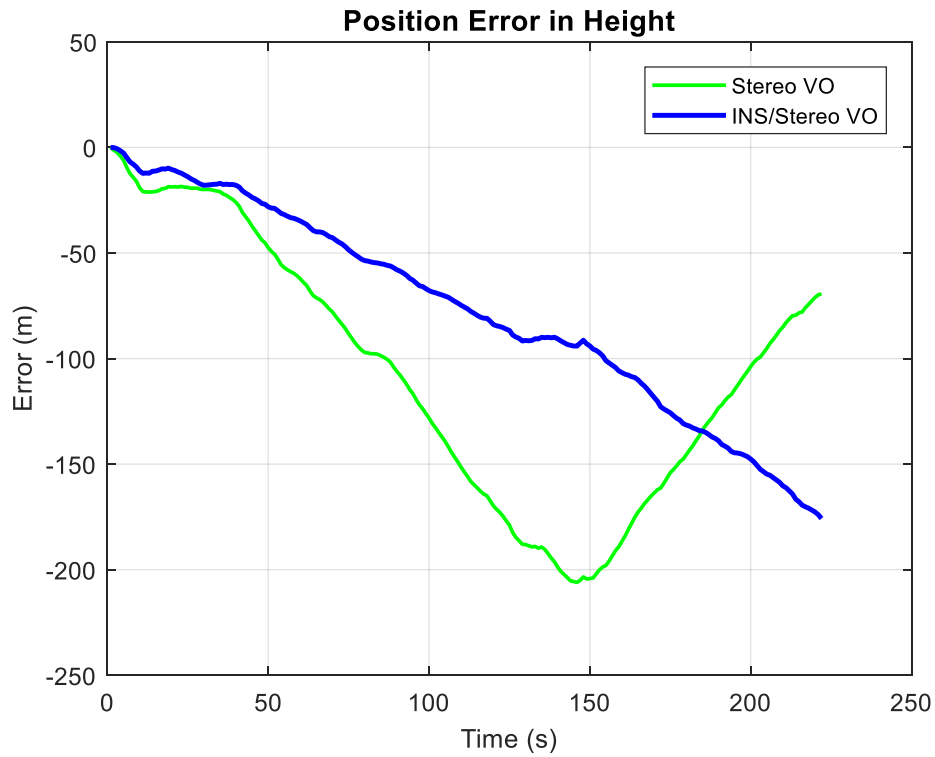


Figure 5.32 Position Errors in East, North and Height

Table 5.12 RMS of Position Errors in East, North and Height (Unit: meter)

	East	North	Height
Stereo VO	37.545	83.505	123.500
INS/ Stereo VO	21.672	61.777	91.390

To test the tightly coupled integration of INS and Stereo VO, a longer test was conducted in the same area. The second test lasted for more than five minutes. This test was conducted on a different day, but the implementation was the same as the first test. The trajectories of the reference, Stereo VO and tight integration of INS and Stereo VO are plotted in red, green and blue respectively in Figure 5.33. This time, it is also very clear that the tightly coupled integration trajectory is closer

to the reference. For the first 150 seconds, the tight integration result follows the correct trajectory very well. After that, the east direction is not as good as the north direction, but still in a reasonable range (about 30 meters). The integrated trajectory still followed the reference. The position error RMS in each direction are summarized in Table 5.13. This time, the height error is much larger than the Stereo VO, but the horizontal accuracy is much improved by the integration method proposed, especially for the north direction. It can be seen that the horizontal error drops from about 185 meters to about 35 meters. Although the error in the height component increases greatly, the 3D error is still reduced by the proposed method.

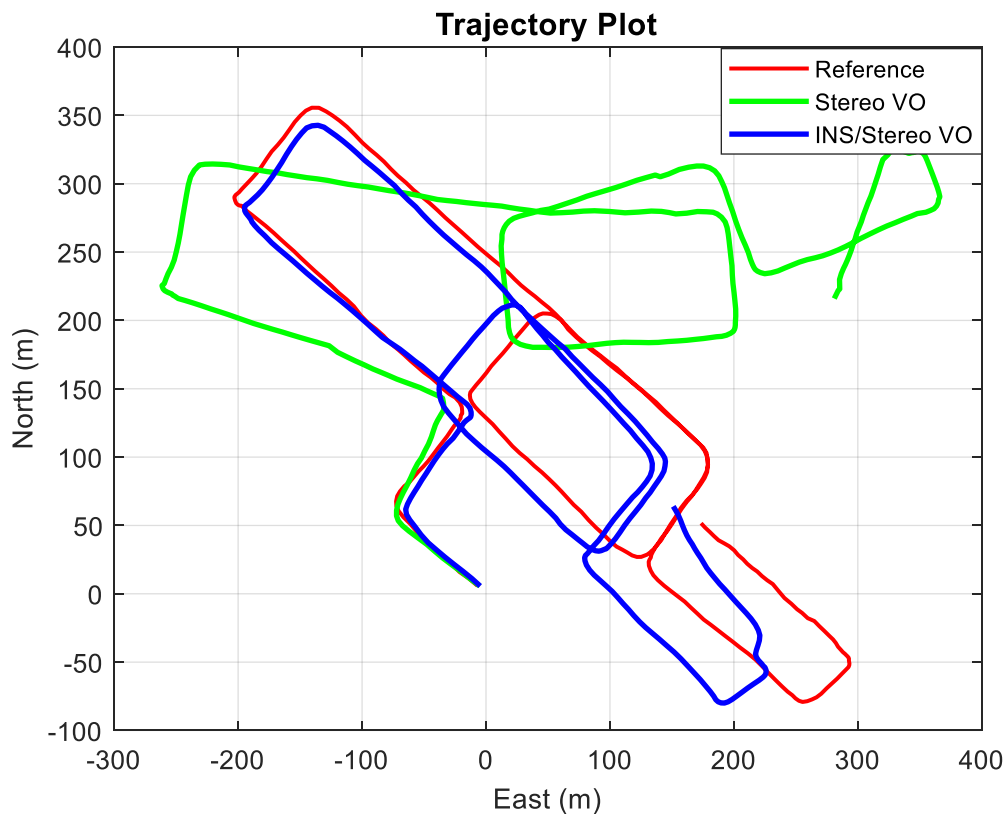


Figure 5.33 Trajectory of the Second Test

Table 5.13 RMS of Position Errors in East, North and Height (Unit: meter)

	East	North	Height
Stereo VO	57.863	176.770	41.055
INS/ Stereo VO	34.866	6.862	114.768



Figure 5.34 Third Test Environment

The results of the tight integration method depend on the quality of the visual measurements namely the pixel coordinates on the stereo images. Since the same visual measurements are used for Stereo VO and the integration, good integration results can be expected if the stand-alone Stereo VO performs well. This is because the good Stereo VO results mean that the quality of the detected and tracked features is high. If the Stereo VO results are not as good as expected, which

means the accuracy of tracked feature coordinates on the images is not good enough, the tight integration of Stereo VO and INS would suffer quick degradation of positioning results as well. However, with the dynamic information provided by the IMU, the tightly coupled integration should have a better result than stand-alone Stereo VO as well. This is the case for the third case. In the third test, the land vehicle was moving in the Brentwood community near the University of Calgary. There are trees and houses along the road that the land vehicle was moving on. The test environment can be seen in Figure 5.34.

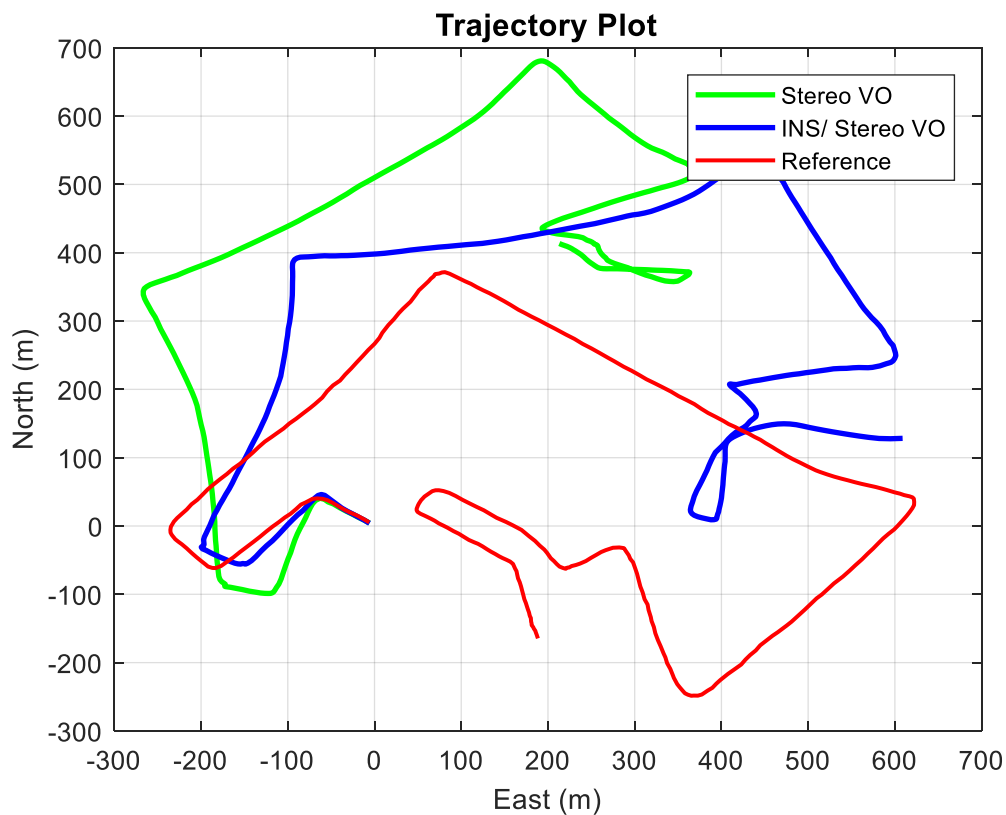
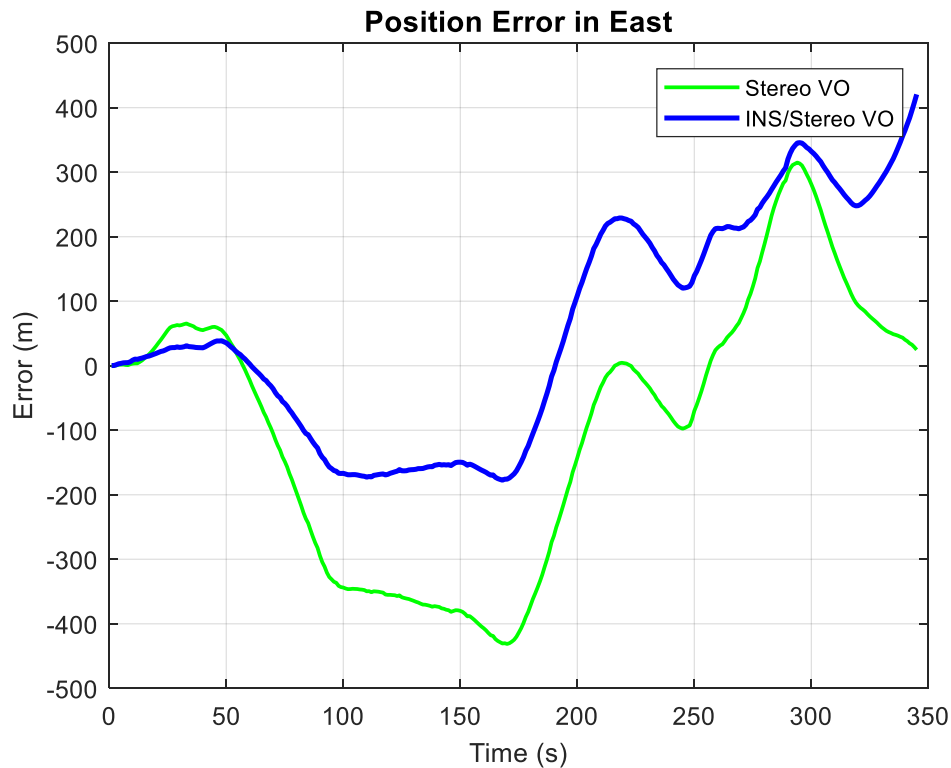


Figure 5.35 Trajectory of the Third Test

The test contained 3450 images lasting about 5.75 minutes. The trajectories of each method are plotted in Figure 5.35. It can be seen that the Stereo VO suffered quicker and larger drift, compared

with the previous two datasets. The reason might be that the cameras suffered more flare due to the weather that day. This results in more outliers and inaccurate pixel coordinates of features. Even though, with INS applied, the tight integration still shows better performance using the method proposed. It can be seen that the trajectory of the integration method becomes closer to the reference with the same features used. The positioning errors in North, East and Height are plotted in Figure 5.36. The errors in each direction using two methods show a similar tendency, but the magnitude of the integration is clearly smaller than the stand-alone Stereo VO. The RMS of the errors is shown in Table 5.14. The RMS values for the integration in three directions are much smaller than the stand-alone Stereo VO.



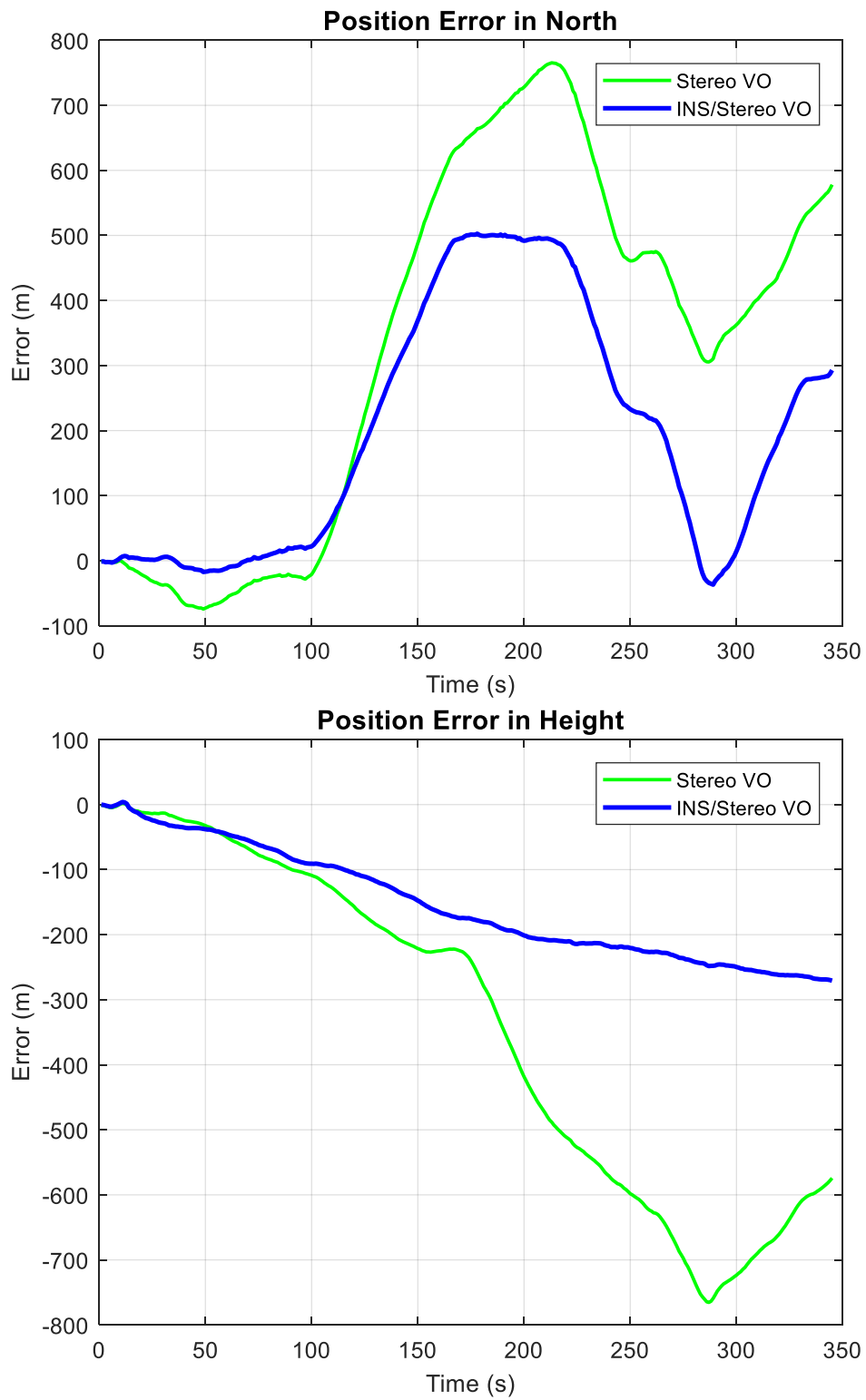


Figure 5.36 Position Errors in East, North and Height

Table 5.14 RMS of Position Errors in East, North and Height (Unit: meter)

	East	North	Height
Stereo VO	227.351	433.893	425.356
INS/ Stereo VO	185.235	271.206	175.487

For DR systems used in the land vehicle navigation, the horizontal accuracy is more important than the vertical accuracy. Therefore, the relative horizontal position errors in each method are summarized in Table 5.15. The tightly coupled integration has the best performance using the second dataset. In comparison, the stand-alone Stereo VO has the worst accuracy for the third dataset due to the inaccuracy of the visual measurements. Improvements can be found for in all three datasets regardless of the performance of the Stereo VO.

Table 5.15 Relative Horizontal Position Errors of Each Method

Dataset	Distance (meter)	Stereo VO	INS/Stereo VO
1	1520	6.02%	4.31%
2	1925	9.66%	1.85%
3	2629	18.63%	12.49%

So far, all three datasets collected in Calgary also show the effectiveness of the tightly coupled integration of INS and Stereo VO. But the results of self-collected datasets are not as good as the KITTI datasets. One of the reasons is that the synchronization of the KITTI dataset is much better

than the dataset collected in Calgary. The more blurred images collected in Calgary also contributes to the degradation of the positioning accuracy. Moreover, the alignment between the sensors, the stereo camera calibration and rectification may also affect the performance of each method.

5.2.3 Tight Integration of INS, Stereo VO and Map Matching

An integrated DR system will suffer a drift after a while as demonstrated in the results of the previous section. Map Matching is necessary in order to further reduce the accumulated error when there is GNSS outage. The results of INS/ Stereo VO/ Map Matching with datasets collected in Calgary are shown in this section. The feature detection and tracking methods used in this part are the same as before. The tightly coupled integration scheme keeps the same as well. The map matched point's coordinates and the road link azimuth are further applied in the IMU mechanization in the next epoch.

The first dataset was collected in the Triwood community near the University of Calgary campus. It lasted for 4 minutes with the traveled distance of about 1716 meters. The estimated trajectories from the tight integration of INS and Stereo VO, INS/ Stereo VO/Map Matching and the GPS SPP reference trajectory are plotted in green, blue and red respectively in Figure 5.37. The road link provided by OpenStreetMap is also plotted. There is an offset between the road link and the GPS trajectory (about 2 meters), which is neglected in the calculation of the position error RMS. The GPS solution is still used as the reference. When there are feedbacks from Map Matching, the tight integration solution is forced to the map matched point on the road link. Therefore, the trajectory of the one with Map Matching suffered discontinuity. If no feedbacks from Map Matching available, the INS/Stereo VO solution is the output, resulting in offset at turnings. With the

correction of Map Matching, the accumulated drift of the integration is greatly reduced. Generally, the trajectory with Map Matching followed the reference. The RMS of positioning errors for INS/ Stereo VO and INS/ Stereo VO/ MM are shown in Table 5.16. It is clear that the horizontal error drops from over 90 meters to less than 20 meters, which indicates the effectiveness of Map Matching. Since the digital map can only provide horizontal coordinates of the map matched point. There is no improvement in the height direction.

Table 5.16 Position RMS of Different Methods for the First Dataset (Unit: meter)

	East	North	Height	Horizontal
INS/Stereo VO	39.114	85.206	113.980	93.755
INS/VO/MM	15.503	10.765	121.419	18.874

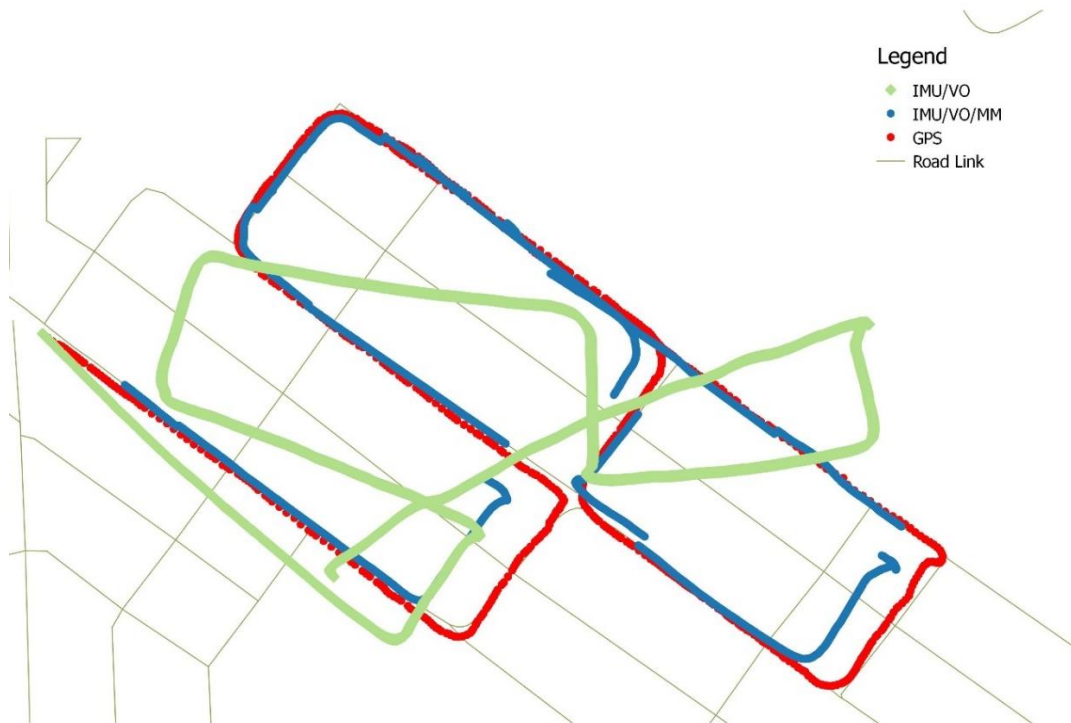


Figure 5.37 Test Trajectories for the First Dataset

The second dataset was collected around the research park near the campus of the University of Calgary. The length of the trajectory with this data is about 1816 meters, and the test lasted for about 4 minutes. The trajectories of each method are plotted in different colors in Figure 5.38. Similar to the previous dataset, the trajectory of the one with Map Matching is forced to the road link when there are feedbacks from Map Matching. The position errors of INS/Stereo VO and INS/Stereo VO/MM are shown in Table 5.17. The horizontal position errors are greatly reduced with Map Matching applied.

Table 5.17 Position RMS of Different Methods for the Second Dataset (Unit: meter)

	East	North	Height	Horizontal
INS/Stereo VO	117.984	99.263	135.561	154.186
INS/VO/MM	12.317	16.256	141.008	20.395



Figure 5.38 Test Trajectories for the Second Dataset

The relative horizontal position errors of these two datasets are summarized in Table 5.18. It can be seen that the horizontal accuracy is greatly improved with the Map Matching applied. The positioning errors decrease from 5.46% to 1.10% and from 8.49% to 1.12% respectively.

Table 5.18 Relative Horizontal Position Errors of Each Method

Dataset	Distance (meter)	INS/Stereo VO	INS/Stereo VO/MM
1	1716	5.46%	1.10%
2	1816	8.49%	1.12%

5.2.4 Tight Integration of GPS, INS and Stereo VO

The dataset of GPS/INS/Stereo VO was collected around the Alberta Children's Hospital in Calgary. All used used were introduced in Section 5.2.1. One Trimble R10 receiver is also set up on the roof of the Engineering Building at the University of Calgary, which is used as the base station for RTK positioning. The RTK solution will be used as the reference to evaluate the results using different sensors. The test environment was open sky with trees and low buildings along the road as shown in Figure 5.39.

The kinematic test lasted for about 6 minutes. The trajectory of this test is shown in Figure 5.40. The trajectory started at (0, 0). Since with GNSS applied, the trajectories are similar, only the one with stand-alone GPS PPP is plotted in Figure 5.40. The land vehicle was in static mode for tens of minutes to make the PPP converged before moving. During the test, code measurements on L1 for some satellites cannot be recorded by the receiver for unknown reasons. To form PPP observations, both L1 and L2 signals are needed. Therefore, only 5 ~6 valid satellites were used for PPP in this test. However, the PPP results are still at decimeter level in the test. The lever arm between sensors were not taken into consideration. The reason for worse GPS/INS solution than GPS PPP may due to the lever arm between the IMU and the GNSS receiver.



Figure 5.39 Test Environment

The position errors in east, north and up directions with GPS, GPS/INS and GPS/INS/Stereo VO are plotted in different colors in Figure 5.41. The accuracy of results using different sensors is similar to each other. Besides, the error tendency of the three methods is similar as well. In open sky environment, GNSS dominates the positioning accuracy because of accurate GNSS measurements. The RMS of results using different sensors in east, north and up directions is summarized in Table 5.19.

The spikes for GPS/INS/Stereo VO are due to the inaccurate synchronization. When the land vehicle is taking maneuvers, there might be a large difference between the predicted measurements and the actual measurements. There is no obvious accuracy difference with GNSS applied in the open sky environment. Since the number of satellite used is only 5~6 and the test time is not long enough, which may lead to the offset in the east direction.

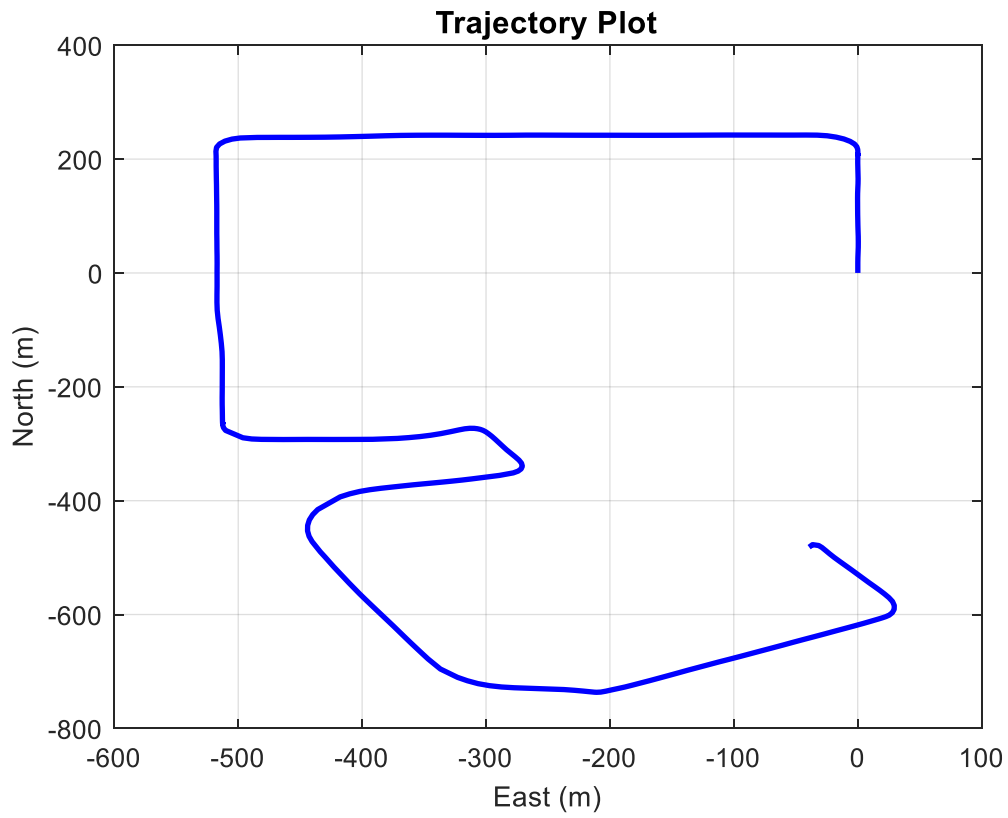
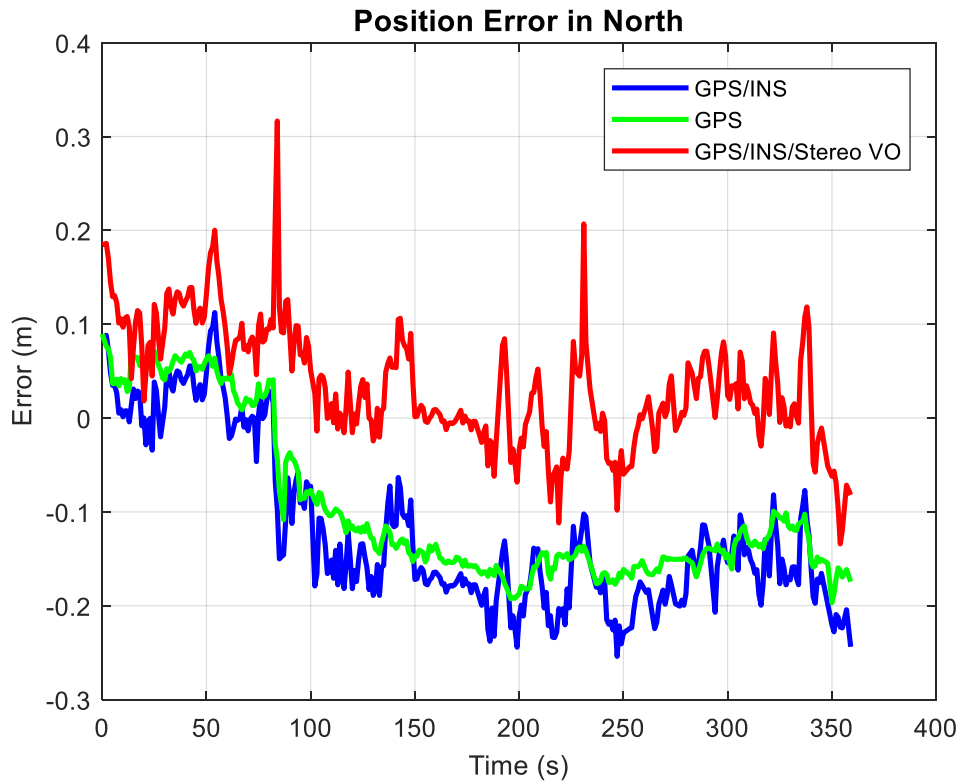
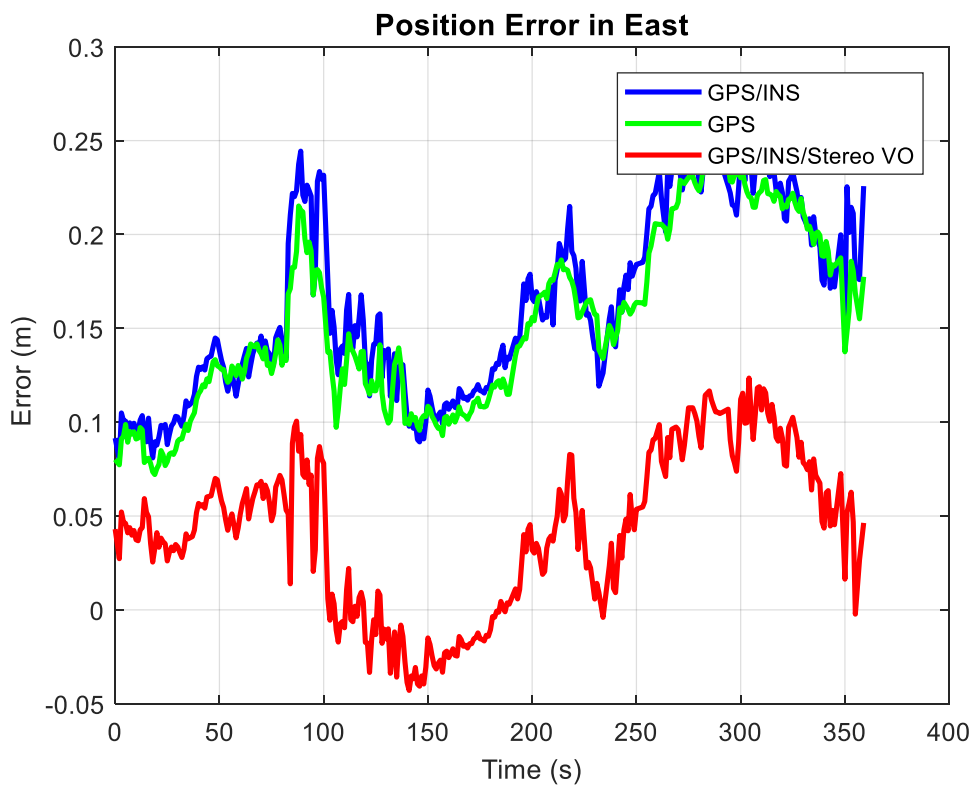


Figure 5.40 The First Test Trajectory

Table 5.19 Positioning Errors with Different Sensors (Unit:meter)

	GPS/INS	GPS PPP	GPS/INS/Stereo VO
East	0.168	0.158	0.059
North	0.147	0.125	0.073
Up	0.175	0.176	0.177



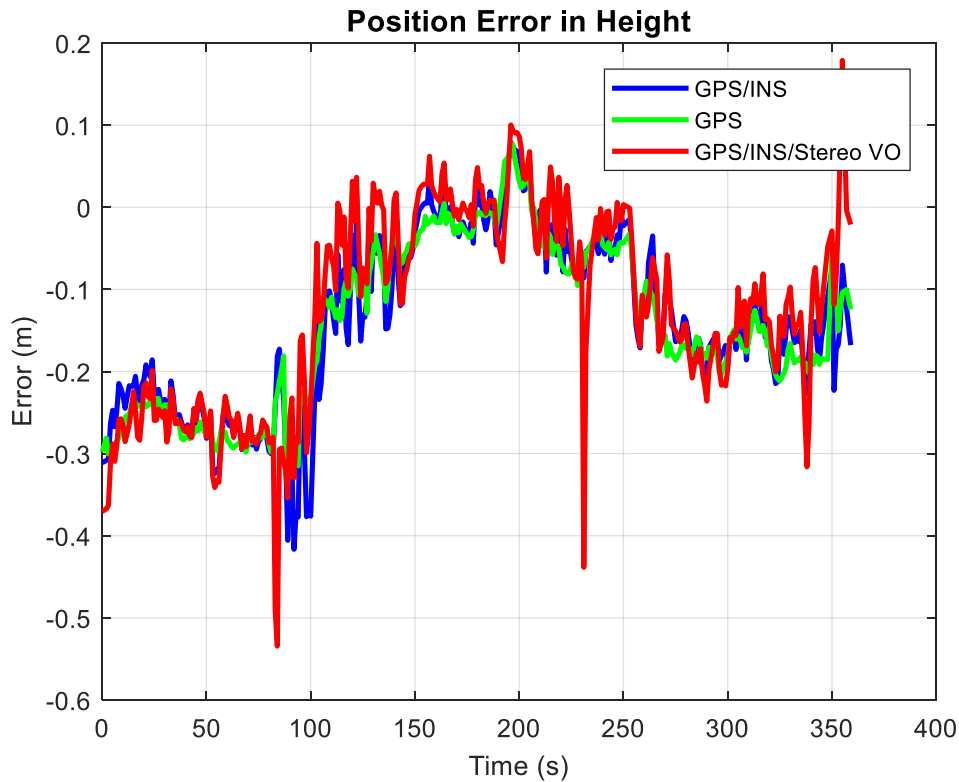


Figure 5.41 Positioning Results in Each Direction

5.2.5 Kinematic PPP AR with the Aid of Map Matching

A field test was conducted to demonstrate the effectiveness of the tight integration of PPP and Map Matching around the campus of the University of Calgary. A Trimble R8 receiver mounted on a land vehicle roof was used to implement the kinematic PPP. A base station was set up at the roof of Engineering Building of the University of Calgary to achieve RTK fixed solution, which is applied as the reference to verify the test results. The test environment is shown in Figure 5.42. There are constructions and trees along the road. The multipath effect of satellites with low elevation would be obvious. Therefore, the elevation mask is set as 15 degrees in this test to exclude those satellites with large noise. The test trajectory is shown in Figure 5.43. The land vehicle began to move after 2 minutes of data collection.



Figure 5.42 Test Environment

This field test was about 13 minutes, and the average velocity of the land vehicle is about 7 m/s. The digital map used in this test is made based on the RTK solution. The fixed RTK solution is in centimeter level, which means the accuracy of the generated digital map is within 20 centimeters. The Map Matching is not applied in the first several minutes during the WL ambiguity resolution. This is to make the float IF ambiguities more converged before Map Matching constraints applied. If the Map Matching is conducted at the beginning, the error of the Map Matching constraints may have a great impact on the ambiguity convergence. In contrast, if the ambiguities take a few minutes to get more converged, it is more likely for the ambiguities to get converged to the correct value. It takes a few minutes to fix the WL ambiguities due to the large noise of code measurements. The MW combination has to be smoothed with multiple measurements collected in order to guarantee the correctness of the fixed WL ambiguities. With Map Matching, the cross-track error of PPP results can be largely reduced while the along-road error cannot be effectively removed.

The ambiguities are correlated with the position errors. With external position measurements, the ambiguities can get converged faster as well, which makes fast PPP AR possible.

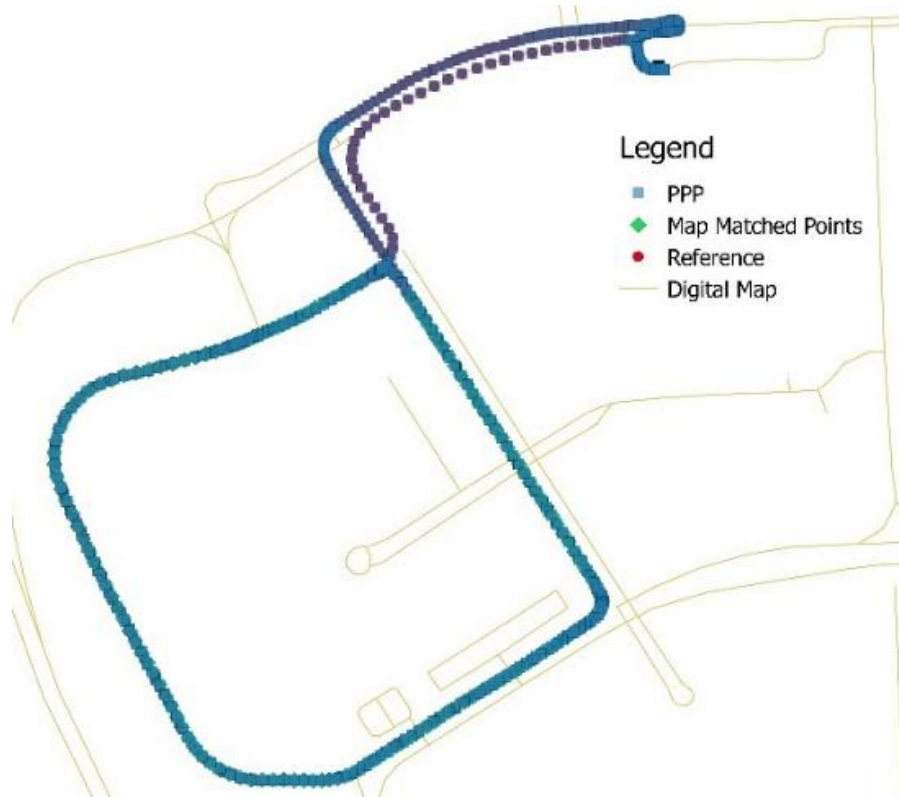


Figure 5.43 Test trajectory

Figure 5.44 shows the satellite sky plot. It can be seen that G21 is the satellite with the highest elevation. In this test, the single-difference between-satellite was implemented. Therefore, G27 was chosen as the reference satellite. In this test, the total number of observed satellites was 9, as shown in Figure 5.44. Among the rest 8 satellites, there were 6 single-difference measurements used in the implementation. G29 was only observed for a short period due to the low elevation. G16 was rejected due to the quality check in the PPP AR, results in ambiguity re-initialization during the test. Partial ambiguity resolution method is applied in this test to improve the ambiguity resolution speed.

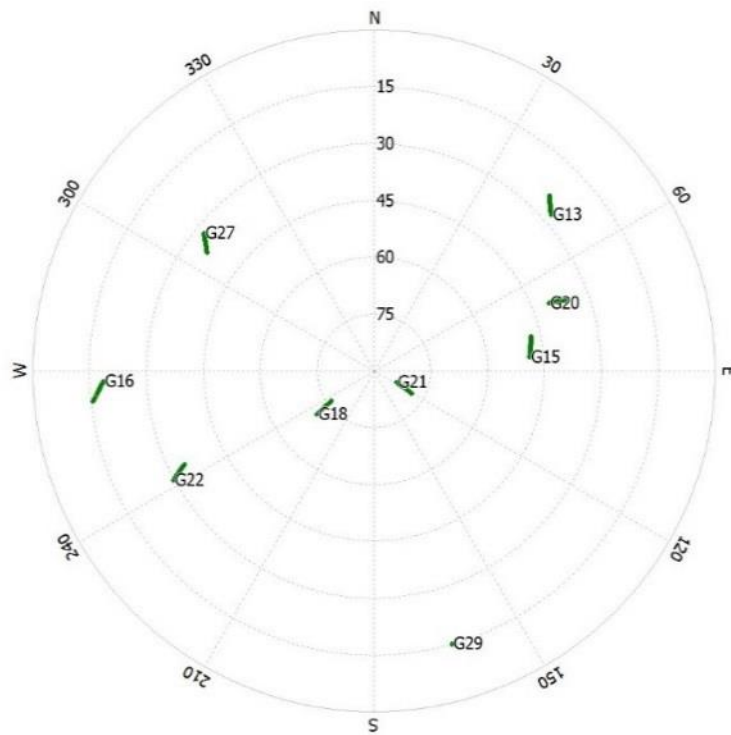
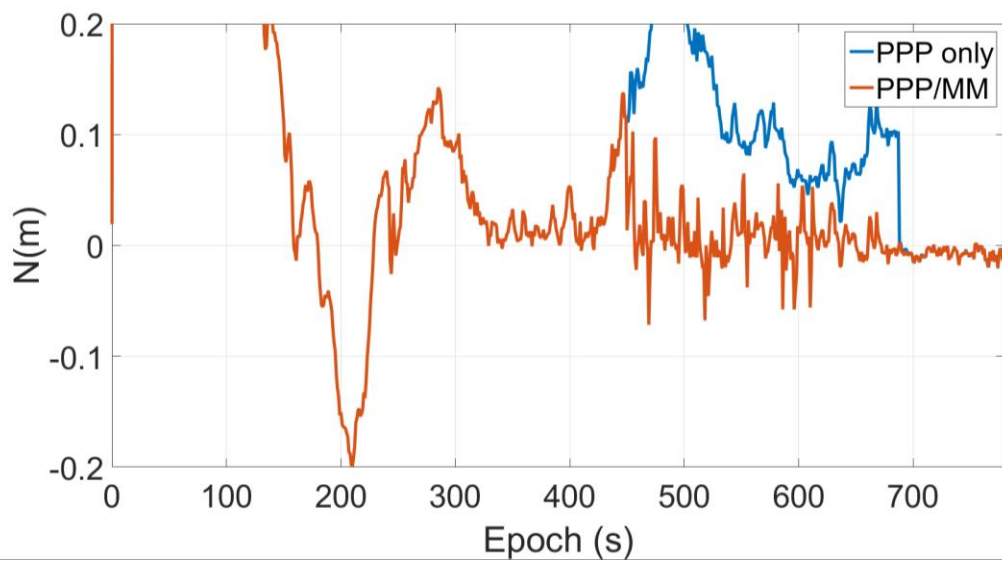
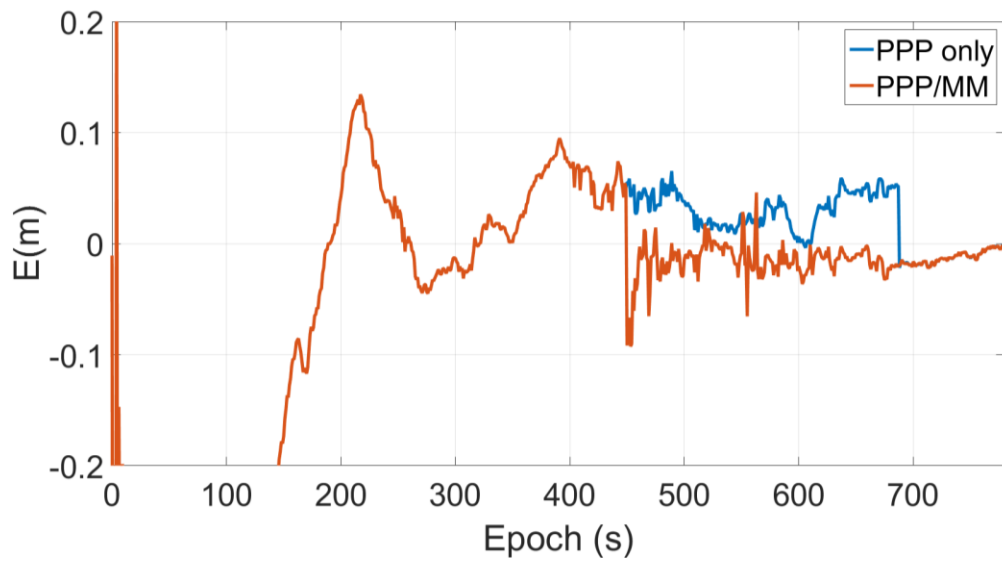


Figure 5.44 Satellite Sky Plot

The positioning results of PPP only and PPP/MM are shown in Figure 5.45 with the RTK fixed solution used as the reference to calculate the positioning errors of each method. The PPP only and PPP/MM results are plotted in different colors. There is no difference between the two different methods in the first half session. This is because the Map Matching was not applied yet before the WL ambiguities were fixed. Application of the Map Matching started at 450th epoch in this test. It is obvious in Figure 5.45 that the Map Matching algorithm immediately improved the positioning accuracy after application, especially for the North direction. The improvement in East is not as good as in North. This is because most of the along-track error is in East direction while the cross-track error mainly lies in North direction. There is little improvement in Up direction with Map Matching

applied, compared with the horizontal directions. This is because the map matched points can only provide horizontal restrictions.



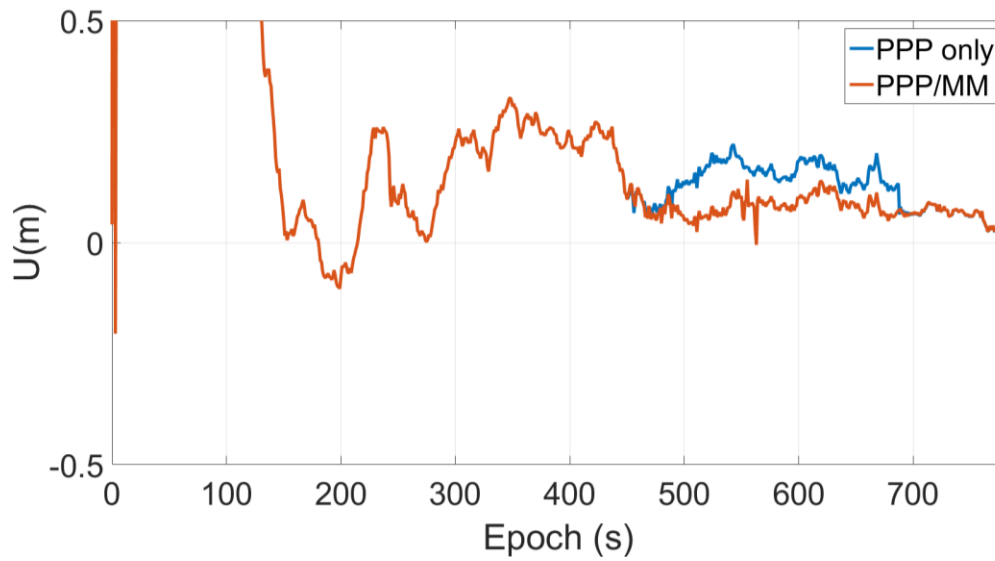


Figure 5.45 Positioning Errors of Each Method

According to Figure 5.45, the NL ambiguities are fixed just several seconds after applying Map Matching. In comparison, without the aid of Map Matching, it takes about another six minutes to fix the NL ambiguities. To see the positioning errors more clearly, the RMS of the positioning errors are shown in Table 5.20. With the aid of Map Matching, the positioning errors in each direction are largely reduced, especially in the north direction. This is not only due to the position improvement with Map Matching constraints, the fast ambiguity resolution also helps improve the positioning results. The horizontal accuracy is at centimeter level after Map Matching and ambiguity resolution.

Table 5.20 Position Error RMS in Each Direction (Unit: meter)

	East	North	Up
PPP only	0.035	0.138	0.151
PPP/MM	0.022	0.024	0.086

As illustrated before, the ambiguities are highly correlated with the estimation of position. Since the position results are improved with the Map Matching constraints, the estimation of ambiguities is improved as well. Besides, with the constraints of Map Matching, the variance-covariance of ambiguities is reduced, which means the search space in ambiguity resolution is reduced, and the ambiguities can be fixed in much shorter time. The estimation of ambiguities is shown in Figure 5.46.

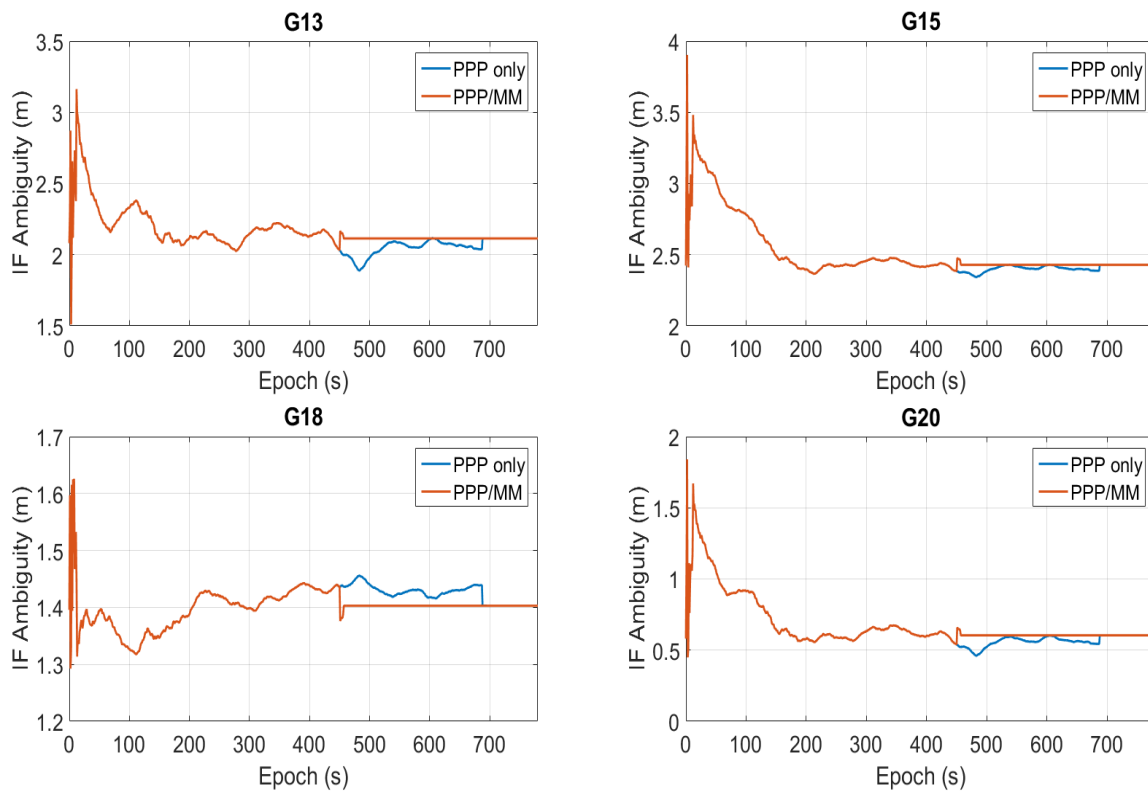


Figure 5.46 Single Difference IF Ambiguities

Shown in Figure 5.46 is the estimated IF ambiguities. Although the corrections for the ambiguities may not be that accurate, it is good enough to achieve partial ambiguity resolution in less than 10 seconds. The stand-alone PPP still needs approximately 200 seconds more to get the NL ambiguities fixed. To see the variation of NL ambiguities more clearly, the NL ambiguities after

applying Map Matching are shown in Figure 5.47. The NL ambiguities with Map Matching are fixed at the 457th epoch while the PPP only fixed the ambiguities at the 688th epoch.

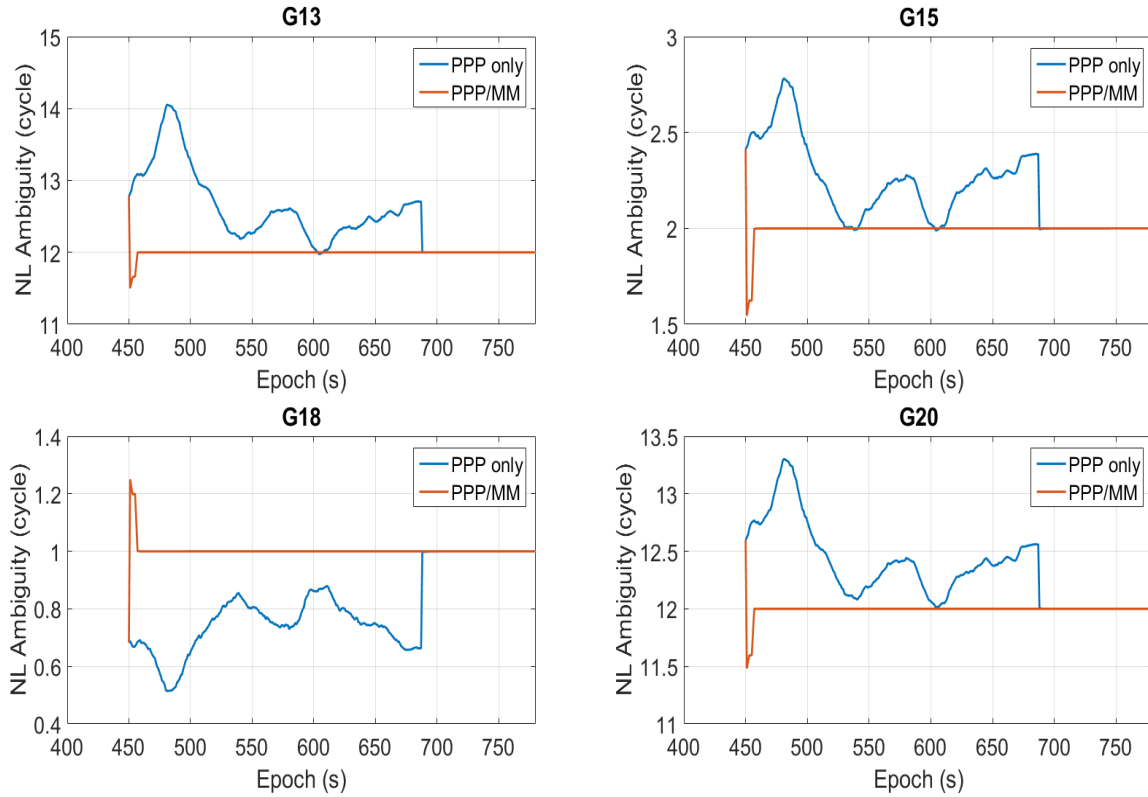


Figure 5.47 Single Difference NL Ambiguities

From Figure 5.47, it can be seen that the NL ambiguities are overcorrected after application of Map Matching, but the reduced search space of integer ambiguities makes the LAMBDA method find the correct integers in much shorter time, compared with the stand-alone PPP.

5.3 Summary

The results of the tests using both KITTI and Calgary datasets have verified the effectiveness of the proposed multi-sensor integration methods. The KITTI data provides the IMU inertial measurements and stereo images, but the raw GNSS data is not available. Therefore, only the

integration of INS, Stereo VO, and the integration of INS, Stereo VO and Map Matching has been conducted with KITTI datasets. The data collection procedures in Calgary are described in detail. The synchronization, calibration and rectification are done professionally for the KITTI datasets, while the datasets collected in Calgary are not as good as KITTI datasets. However, the tightly coupled integration of INS and Stereo VO has shown better performance than the stand-alone Stereo VO using both datasets. Moreover, the application of Map Matching has further reduced the accumulated navigation errors during GNSS outage periods using both datasets.

The integration of INS, Stereo VO and GNSS with IMU as the core sensor is tested using the data collected in Calgary. The IMU data is available all the time, which makes it suitable to provide the dynamic information of the land vehicle while the measurements from other sensors are used to correct the errors and update the solution. The result shows that the GNSS dominates the positioning accuracy in open sky environments.

In open sky environment, fast kinematic PPP ambiguity resolution method with the aid of Map Matching is explored and verified by the Calgary data. Map Matching projects the PPP float solution on the road links, and the projected point could be used as additional measurements in Kalman filter. Besides, the road link azimuth can be treated as constraints for PPP as well. With these external position information, the PPP ambiguities can converge faster since the ambiguities are correlated with the position unknown parameters. The Calgary dataset shows that the PPP ambiguities can be fixed in several seconds after the application of Map Matching.

Chapter Six: CONCLUSIONS AND FUTURE WORKS

The development and analysis of GNSS, INS and Stereo VO tight integration system for land vehicle navigation is the major aim of this thesis. The tight integration architecture for three different types of systems is proposed and developed to improve the performance of the navigation system. In addition, Map Matching is integrated with INS/ Stereo VO in GNSS denied environment to limit the accumulation of errors, and it is also used to accelerate the PPP ambiguity resolution in kinematic positioning in open sky environment. Generally, IMU is applied as the core sensor in the implementation. When GNSS or Stereo VO measurements are available, the accumulated error of INS can be limited, and the solution can be improved because of external measurements. In this way, the system can work in most environments. When the land vehicle is in GNSS denied environments, an INS/ Stereo VO integrated system can provide a continuous solution to bridge the outages of GNSS. Map Matching integrated with INS/ Stereo VO can further improve the position accuracy. When the land vehicle is traveling in open sky environments with just one GNSS receiver, the accurate digital map can be used to provide external position information to aid PPP AR.

6.1 Conclusions

1. A tightly coupled integration of INS and Stereo VO method can effectively reduce the accumulation of errors, compared to an INS-alone or VO-alone system. The implementation aspects for tightly coupled integration of inertial sensors and stereo cameras are explored in detail. The IMU mechanization provides the dynamic information for the system. Specifically, the position and attitude can be utilized to predict the pixel coordinates of features on the stereo images. The visual measurements from the Stereo

cameras, namely the pixel coordinates of the tracked features are used to reduce the inertial errors. The error-state model in the Kalman filter is used in this implementation. The difference between the predicted and measured pixel coordinates is used to estimate the errors. In this way, the visual information could be fully applied in the integration. The improvements are obvious when compared to stand-alone Stereo VO. Besides, Stereo VO cannot provide direct velocity while the tightly coupled integration is capable of providing the velocity with less noise.

2. The tightly coupled integration architecture for INS and Stereo VO can be extended to include GNSS measurements as well. A tight integration of GNSS, INS and Stereo VO is proposed. The IMU is applied as the core sensor while GNSS and Stereo VO measurements are used to correct the INS errors. With such integration architecture, the implementation can be flexible. With either type of the measurements is available, it can be applied in the integrated system. GNSS dominates the system in open sky environments and the accuracy of the integrated system is similar to a stand-alone GNSS system.
3. Digital maps can be used to provide external position information to the integrated navigation system in addition to GNSS. With the fuzzy logic Map Matching method used in this thesis, the INS/Stereo VO solutions can be projected on the digital map. With the information of the projected points on the digital map, the cross-road errors can be largely reduced and better results can be achieved. The integration of INS, Stereo VO and Map Matching could be a valid method for land vehicle navigation in GNSS denied environments.

4. In open sky environment, Map Matching can also be used to accelerate the PPP ambiguity resolution. With the position information provided by the accurate digital map, the PPP ambiguities can converge faster since the ambiguities are correlated with the position. The projected point on the digital map and the road link azimuth is applied as the additional measurements in Kalman filter. With the additional measurements, the integer ambiguity search space is reduced and the efficiency of finding the correct integer ambiguities can be greatly improved. This results in fast kinematic PPP AR.

6.2 Future Work

Several future research works are identified and provided as follows:

1. Improvement of feature detection and tracking algorithms. The current feature detection and tracking still need to be further improved to have better performance for stand-alone Stereo VO.
2. The correlation between the tracking pixel coordinates needs to be taken into consideration in implementation.
3. Development of quality control methods for GNSS and Stereo VO measurements, based on the tightly coupled integration architecture. One of the advantages of tightly coupled integration is better quality control with the prediction of measurements based on INS. More efficient outlier detection methods should be developed and implemented.
4. Development and test of the integrated system in challenging environments (e.g. not enough number of satellites). With the development of multi GNSS constellations, it is more frequent to meet the situation where some satellites are not working properly, compared with GNSS denied environment. In some cases, only few satellites can provide valid measurements. Methods for

positioning with less number of satellites should be developed. Combined with the outlier detection, this could further improve the system integrity.

5. Development of real-time processing system. The real-time system would be much more challenging, but it is also much more useful for land vehicle navigation. The processing speed needs to be improved and the saved images have to be handled properly to deal with the large size of image data.

6. Development of integration with other sensors. There are other sensor options that can be utilized for the land vehicle navigation. For example, a depth camera can provide the depth information to avoid the depth ambiguity with a monocular camera. The laser scanner can work without illumination, which could further improve the integrity of the system.

7. Integration with reduced IMU (2 accelerometers, 1 gyro) to reduce the quick accumulation of errors. For land vehicle navigation, the reduced IMU can satisfy the application in general cases. The integration with reduced IMU needs to be studied.

8. IMU mechanization with non holonomic constraints. The main drawback of the low-cost IMU is the quick drift with full mechanization. The non holomic constraints can effectively reduce the quick accumulation of errors. Integration with holomic constraints can further reduce the error.

References

- Abdel-salam, M. A. (2005). *Precise Point Positioning Using Un-Differenced Code and Carrier Phase Observations*. Department of Geomatics Engineering. University of Calgary.
- Ahmed El-Rabbany. (2002). *Introduction to The Global Positioning System*. Artech house.
- Angrisano, A. (2010). GNSS/INS integration methods. *Dottorato Di Ricerca (PhD) in Scienze Geodetiche E Topografiche Thesis, Universita' degli Studi Di Napoli PARTHENOPE, Naples*.
- Asadi, E., & Bottasso, C. L. (2014). Tightly-coupled stereo vision-aided inertial navigation using feature-based motion sensors. *Advanced Robotics*, 28(11), 717–729.
<https://doi.org/10.1080/01691864.2013.870496>
- Ashby, N. (2003). The Sagnac effect in the Global Positioning system. In *Fundamental Theories of Physics* (Vol. 135, pp. 11–28). Springer. Retrieved from
http://areeweb.polito.it/ricerca/relgrav/solciclos/ashby_d.pdf
- Aumayer, B. M., Petovello, M. G., & Lachapelle, G. (2014). Development of a Tightly Coupled Vision/GNSS System. *Proceedings of the 20th International Technical Meeting of the Satellite Division of The Institute of Navigation (ION GNSS 2014)*, (September 2014), 8–12.
- Bailey, T., & Durrant-Whyte, H. (2006). Simultaneous localization and mapping (SLAM): Part II. *IEEE Robotics & Automation Magazine*, 13(3), 108–117.
- Baker, S., & Matthews, I. (2002). Lucas-Kanade 20 Years On: A Unifying Framework: Part 1. *International Journal of Computer Vision*, 56(3), 221–255.
- Balazadegan Sarvrood, Y. (2016). *Multi-Sensor Map Matching Techniques for Autonomous Land Vehicle Navigation*. University of Calgary.
- Balazadegan Sarvrood, Y., & Amin, N. (2011). Server Based Real Time GPS-IMU Integration Aided by Fuzzy Logic Based Map Matching Algorithm for Car Navigation. *Built Environment*, (September).
- Balazadegan Sarvrood, Y., & Gao, Y. (2014). Analysis and Reduction of Stereo Vision Alignment and Velocity Errors for Vision Navigation. In *Proceedings of the 27th International Technical Meeting of The Satellite Division of the Institute of Navigation* (p. 3254–3262.). IEEE. Retrieved from

- <https://www.ion.org/publications/abstract.cfm?jp=p&articleID=12408>
- Balazadegan Sarvrood, Y., Liu, F., & Gao, Y. (2017). Tight integration of kinematic precise point positioning and digital map for land vehicle localisation. *Survey Review*, 1–9.
- Bay, H., Tuytelaars, T., & Van Gool, L. (2006). Surf: Speeded up robust features. *Computer vision–ECCV 2006*, 404–417.
- Bisnath, S., & Gao, Y. (2008). Current State of Precise Point Positioning and Future Prospects and Limitations. In *Observing our Changing Earth* (pp. 615–623). Berlin, Heidelberg: Springer Berlin Heidelberg. https://doi.org/10.1007/978-3-540-85426-5_71
- Bradski, G., & Kaehler, A. (2008). *Learning OpenCV: Computer vision with the OpenCV library*. “O’Reilly Media, Inc.”
- Brubaker, M. A., Geiger, A., & Urtasun, R. (2013). Lost! Leveraging the Crowd for Probabilistic Visual Self-Localization. In *Proceedings of the IEEE Conference on Computer Vision and Pattern Recognition* (pp. 1–8). Retrieved from <http://www.cs.toronto.edu/~mbrubake/projects/map/%0Apapers3://publication/uuid/15AA848E-6274-4104-A173-173F15874D5E>
- Caligiuri, L. M., & Sorli, A. (2014). The Sagnac effect in GPS, absolute simultaneity and the new meaning of time. In *Proceedings 20th IMEKO TC4 International Symposium*.
- Cannon, S. G. Æ. M. E. (2007). GPS / MEMS INS integrated system for navigation in urban areas. *Gps Solutions*, 11(3), 193–203. <https://doi.org/10.1007/s10291-006-0050-8>
- Carrillo, L. R. G., López, A. E. D., Lozano, R., & Pégard, C. (2012). Combining stereo vision and inertial navigation system for a quad-rotor UAV. *Journal of Intelligent & Robotic Systems*, 65(1–4), 373–387.
- Collins, P. (2008). Isolating and Estimating Undifferenced GPS Integer Ambiguities. In *Proceedings of the 2008 National Technical Meeting of The Institute of Navigation* (Vol. 2830, pp. 720–732). <https://doi.org/10.1017/CBO9781107415324.004>
- Du, S., & Gao, Y. (2012). Inertial aided cycle slip detection and identification for integrated PPP GPS and INS. *Sensors*, 12(11), 14344–14362.
- Durrant-Whyte, H., & Bailey, T. (2006). Simultaneous localization and mapping: part I. *IEEE Robotics & Automation Magazine*, 13(2), 99–110.

- Dusha, D., & Mejias, L. (2012). Error analysis and attitude observability of a monocular GPS/visual odometry integrated navigation filter. *The International Journal of Robotics Research*, 31(6), 714–737. <https://doi.org/10.1177/0278364911433777>
- El-Sheimy, N. (2013). *Inertial Surv & Ins/Gps Integrate. ENGO 623 Lecture Notes*. University of Calgary.
- FLIR Knowledge Base. (2017). Configuring Synchronized Capture with Multiple Cameras.
- Floros, G., Van Der Zander, B., & Leibe, B. (2013). OpenStreetSLAM: Global vehicle localization using OpenStreetMaps. In *Proceedings - IEEE International Conference on Robotics and Automation* (pp. 1054–1059). IEEE. <https://doi.org/10.1109/ICRA.2013.6630703>
- Forsyth, D., & Ponce, J. (2011). *Computer vision: a modern approach*. Upper Saddle River, NJ; London: Prentice Hall.
- Fraundorfer, F., & Scaramuzza, D. (2012). Visual Odometry : Part II: Matching, Robustness, Optimization, and Applications. *Robotics Automation Magazine, IEEE*, 19(2), 78–90. <https://doi.org/10.1109/MRA.2012.2182810>
- Gao Y, S. X. (2002). A new method for carrier phase based precise point positioning. *Navigation*, 49(2), 109–116. <https://doi.org/10.1002/j.2161-4296.2002.tb00260.x>
- Ge, M., Gendt, G., Rothacher, M., Shi, J., & Liu, J. (2007). Resolution of GPS carrier-phase ambiguity in precise point positioning. *Egu*, 82(7), 401–401. <https://doi.org/10.1007/s00190-007-0208-3>
- Geiger, A., Lenz, P., Stiller, C., & Urtasun, R. (2013). Vision meets robotics: The KITTI dataset [J]. *The International Journal of Robotics Research*.
- Geiger, A., Moosmann, F., Car, Ö., & Schuster, B. (2012). Automatic camera and range sensor calibration using a single shot. In *Robotics and Automation (ICRA), 2012 IEEE International Conference on* (pp. 3936–3943). IEEE.
- Geng, J., & Bock, Y. (2013). Triple-frequency GPS precise point positioning with rapidambiguity resolution. *Journal of Geodesy*, 87(5), 449–460.
- Geng, J., Teferle, F. N., Meng, X., & Dodson, A. H. (2011). Towards PPP-RTK: Ambiguity resolution in real-time precise point positioning. *Advances in Space Research*, 47(10),

1664–1673.

- Gérard, P., & Luzum, B. (2010). *IERS Conventions (2010). Bureau International Des Poids Et Mesures Sevres (France)*. DTIC Document. Retrieved from <http://www.iers.org/TN36/>
- Gopaul, N. S., Wang, J. G., & Hu, B. (2015). Multi-frame Visual Odometry in Image-Aided Inertial Navigation System. In *China Satellite Navigation Conference (CSNC) 2015 Proceedings: Volume III* (pp. 649–658). Springer.
- Greenfeld, J. S. (2002). Matching GPS Observations to Locations on a Digital Map. In *Transportation Research Board* (p. 13).
- Harris, C., & Stephens, M. (1988). A combined corner and edge detector. In *Alvey vision conference* (Vol. 15, pp. 10–5244). Manchester, UK.
- Hartley, R., & Zisserman, A. (2003). *Multiple view geometry in computer vision*. Cambridge university press.
- Heikkila, J., & Silven, O. (1997). A four-step camera calibration procedure with implicit image correction. In *Computer Vision and Pattern Recognition, 1997. Proceedings., 1997 IEEE Computer Society Conference on* (pp. 1106–1112). IEEE.
- Igs. (2010). IGS Products. Retrieved from <http://igsb.jpl.nasa.gov/components/prods.html>
- IGS RTS Monitor. (2013). Real-time Service Monitor.
- Inside GNSS. (2013). IGS Launches Real-Time Service for High-Precision GNSS. *Inside Gnss*.
- Jekeli, C. (2001). *Inertial navigation systems with geodetic applications*. Walter de Gruyter.
- Ji, P. (2016). StereoScan : Dense 3D Reconstruction in. In *Intelligent Vehicles Symposium (IV), 2011 IEEE* (pp. 1–9). IEEE.
- Kleinert, M., & Schleith, S. (2010). Inertial aided monocular SLAM for GPS-denied navigation. *IEEE International Conference on Multisensor Fusion and Integration for Intelligent Systems*, 20–25. <https://doi.org/10.1109/MFI.2010.5604453>
- Kong, X., Wu, W., Zhang, L., & Wang, Y. (2015). Tightly-coupled stereo visual-inertial navigation using point and line features. *Sensors (Switzerland)*, 15(6), 12816–12833. <https://doi.org/10.3390/s150612816>
- Konolige, K., Agrawal, M., & Sola, J. (2007). Large Scale Visual Odometry for Rough Terrain. In *IROS visual SLAM workshop* (pp. 201–212). Springer. <https://doi.org/10.1007/978-3->

- Kouba, J. (2009). A Guide to using international GNSS Service (IGS) Products. *Geodetic Survey Division Natural Resources Canada Ottawa*. Retrieved from <http://graypantherssf.igs.org/igscb/resource/pubs/UsingIGSProductsVer21.pdf>
- Kouba, J., & Héroux, P. (2001). Precise Point Positioning Using IGS Orbit and Clock Products. *GPS Solutions*, 5(2), 12–28. <https://doi.org/10.1007/PL00012883>
- Laganière, R. (2017). *OpenCV 3 Computer Vision Application Programming Cookbook*. Packt Publishing Ltd.
- Laurichesse, D., Mercier, F. (2007). Integer Ambiguity Resolution on Undifferenced GPS Phase Measurements and its Application to PPP. *Proceedings of the 20th International Technical Meeting of the Satellite Division of The Institute of Navigation (ION GNSS 2007)*, 56(September), 839–848. [https://doi.org/10.1016/S0273-1177\(02\)00277-6](https://doi.org/10.1016/S0273-1177(02)00277-6)
- Lee, H.-K., Wang, J., & Rizos, C. (2003). Effective cycle slip detection and identification for high precision GPS/INS integrated systems. *The Journal of Navigation*, 56(3), 475–486.
- Li, H., Zhou, X., Wu, B., & Wang, J. (2012). Estimation of the inter-frequency clock bias for the satellites of PRN25 and PRN01. *Science China Physics, Mechanics & Astronomy*, 55(11), 2186–2193.
- Liu, F. (2017). Kinematic PPP Ambiguity Resolution with Aid of Map Matching. In *the 30th International Technical Meeting of The Satellite Division of the Institute of Navigation (ION GNSS+ 2017)* (pp. 4176–4183).
- Liu, F., & Gao, Y. (2017). Triple-Frequency GPS Precise Point Positioning Ambiguity Resolution Using Dual-Frequency Based IGS Precise Clock Products. *International Journal of Aerospace Engineering*, 2017.
- Liu, F., Sarvrood, Y. B., & Gao, Y. (2015). Tightly Coupled Stereo Vision Aided Inertial Navigation Using Continuously Tracked Features for Land Vehicles. In *the 28th International Technical Meeting of The Satellite Division of the Institute of Navigation (ION GNSS+ 2015)* (pp. 2127–2133). Tampa.
- Liu, F., Sarvrood, Y. B., & Gao, Y. (2017). Implementation and Analysis of Tightly Integrated INS/Stereo VO for Land Vehicle Navigation. *The Journal of Navigation*, 1–17.

- Lowe, D. G. (1991). Fitting Parametrized Three-Dimensional Models to Images. *IEEE Transactions on Pattern Analysis and Machine Intelligence*, 13(5), 441–450. Retrieved from <http://www.computer.org/csdl/trans/tp/1991/05/i0441.pdf>
- Lowe, D. G. (2004). Distinctive image features from scale-invariant keypoints. *International Journal of Computer Vision*, 60(2), 91–110.
- Lucas, B. D., & Kanade, T. (1981). An iterative image registration technique with an application to stereo vision.
- Mamdani, E. H. (1974). Application of fuzzy algorithms for control of simple dynamic plant. *Proceedings of the Institution of Electrical Engineers*, 121(12), 1585. <https://doi.org/10.1049/piee.1974.0328>
- Mathworks Documentation. (2017). What Is Camera Calibration?
- Meng, Y. (2006). *Improved positioning of land vehicle in its using digital map and other accessory information*. The Hong Kong Polytechnic University. <https://doi.org/DAI-A67/11>, p. 4359, May 2007
- Montenbruck, O., & Et.al. (2014). IGS-MGEX Preparing the Ground for Multi-Constellation GNSS Science. *Inside GNSS*, 9(January/February), 42–49. Retrieved from <http://www.insidegnss.com/auto/janfeb14-MONTENBRUCK.pdf>
- Montenbruck, O., Hugentobler, U., Dach, R., Steigenberger, P., & Hauschild, A. (2012). Apparent clock variations of the Block IIF-1 (SVN62) GPS satellite. *GPS Solutions*, 16(3), 303–313.
- Moon, S. W., Hwang, D.-H., Sung, T. K., & Lee, S. J. (2000). Design and implementation of an efficient tightly-coupled GPS/INS integration scheme. In *Proceedings of the 2000 National Technical Meeting of The Institute of Navigation* (pp. 159–165).
- Navipedia. (2011). Precise Point Positioning. *GPS World*, 20(4350), 4. Retrieved from http://www.navipedia.net/index.php/Precise_Point_Positioning
- Niell, A. E. (1996). Global mapping functions for the atmosphere delay at radio wavelengths. *Journal of Geophysical Research: Solid Earth*, 101(B2), 3227–3246. <https://doi.org/10.1029/95JB03048>
- Noureldin, A., Karamat, T. B., & Georgy, J. (2013). *Fundamentals of inertial navigation*,

- satellite-based positioning and their integration. Fundamentals of Inertial Navigation, Satellite-Based Positioning and their Integration.* Springer Science & Business Media.
<https://doi.org/10.1007/978-3-642-30466-8>
- Parkinson, B. W., & Enge, P. K. (1996). *Progress In Astronautics and Aeronautics: Global Positioning System: Theory and Applications, Volume 2* (Vol. 2). Aiaa. Retrieved from
<https://books.google.com/books?hl=fr&lr=&id=t0eGFpSwN0wC&pgis=1>
- Petovello, M. G. (2003). Real-Time Integration of a Tactical-Grade IMU and GPS for High-Accuracy Positioning and Navigation. *Thesis*, (20173), 242. Retrieved from
<http://www.geomatics.ucalgary.ca/links/GradTheses.html>
- Piniés, P., Lupton, T., Sukkarieh, S., & Tardós, J. D. (2007). Inertial aiding of inverse depth SLAM using a monocular camera. *Proceedings - IEEE International Conference on Robotics and Automation*, (April), 2797–2802.
<https://doi.org/10.1109/ROBOT.2007.363895>
- Poelman, C. J., & Kanade, T. (1997). A paraperspective factorization method for shape and motion recovery. *Pattern Analysis and Machine Intelligence, IEEE Transactions on*, 19(3), 206–218. <https://doi.org/10.1109/34.584098>
- Qian, G., Chellappa, R., & Zheng, Q. (2001). Robust structure from motion estimation using inertial data. *J. Opt. Soc. Am*, 18(12), 2982–2997.
<https://doi.org/10.1364/JOSAA.18.002982>
- Quddus, M. a. (2006). High Integrity Map Matching Algorithms for Advanced Transport Telematics Applications. *Centre for Transport Studies Department of Civil and Environmental Engineering Imperial College London United Kingdom*. Citeseer.
- Rizos, C., Janssen, V., Roberts, C., & Ginter, T. (2012). GNSS: Precise Point Positioning PPP versus DGNSS. *Geomatics World*, (October), 18–20.
- Rizos, C., Montenbruck, O., Weber, R., Weber, G., Neilan, R., & Hugentobler, U. (2013). The IGS MGEX Experiment as a Milestone for a Comprehensive Multi-GNSS Service. *Proceedings of the Ion Pacific Pnt Meeting*, 8900(6), 289–295. Retrieved from
https://www.researchgate.net/publication/259897379_The_IGS_MGEX_experiment_as_a_milestone_for_a_comprehensive_multi-GNSS_service

- Rosten, E., & Drummond, T. (2006). Machine learning for high-speed corner detection. *Computer Vision–ECCV 2006*, 430–443.
- Rosyara, U. R., Vromman, D., & Duveiller, E. (2008). Canopy temperature depression as an indication of correlative measure of spot blotch resistance and heat stress tolerance in spring wheat. *Journal of Plant Pathology*, 90(1), 103–107. [https://doi.org/10.1016/S0019-9958\(65\)90241-X](https://doi.org/10.1016/S0019-9958(65)90241-X)
- Scaramuzza, D., & Fraundorfer, F. (2011). Visual odometry [tutorial]. *IEEE Robotics & Automation Magazine*, 18(4), 80–92. <https://doi.org/10.1109/MRA.2011.943233>
- Schleicher, D., Bergasa, L. M., Ocaña, M., Barea, R., & López, M. E. (2009). Real-time hierarchical outdoor slam based on stereovision and GPS fusion. *IEEE Transactions on Intelligent Transportation Systems*, 10(3), 440–452. <https://doi.org/10.1109/TITS.2009.2026317>
- Shi, J. (1994). Good features to track. In *Computer Vision and Pattern Recognition, 1994. Proceedings CVPR '94., 1994 IEEE Computer Society Conference on* (pp. 593–600). IEEE.
- Shi, J., & Gao, Y. (2014). A comparison of three PPP integer ambiguity resolution methods. *GPS Solutions*, 18(4), 519–528. <https://doi.org/10.1007/s10291-013-0348-2>
- Shin, E.-H. (2005). Estimation techniques for low-cost inertial navigation. *ProQuest Dissertations and Theses*, NR06960(20219), 206-206 . Retrieved from http://ezproxy.net.ucf.edu/login?url=http://search.proquest.com/docview/305029321?accountid=10003%5Cnhttp://sfx.fcla.edu/ucf?url_ver=Z39.88-2004&rft_val_fmt=info:ofi/fmt:kev:mtx:dissertation&genre=dissertations+&+theses&sid=ProQuest+Dissertations+&+T
- Sickle, J. Van. (2008). *GPS for Land Surveyors*. CRC Press. Retrieved from <https://books.google.com/books?hl=en&lr=&id=J0fLBQAAQBAJ&pgis=1>
- Skog, I., & Handel, P. (2009). In-car positioning and navigation technologies; A survey. *IEEE Transactions on Intelligent Transportation Systems*, 10(1), 4–21. <https://doi.org/10.1109/TITS.2008.2011712>
- Soloviev, A., & Miller, M. M. (2012). Navigation in difficult environments: Multi-sensor fusion techniques. In *Springer Optimization and Its Applications* (Vol. 61, pp. 199–229). Springer.

- https://doi.org/10.1007/978-0-387-88619-0_9
- Strelow, D., & Singh, S. (2004). Motion Estimation from Image and Inertial Measurements. *The International Journal of Robotics Research*, 23(12), 1157–1195.
<https://doi.org/10.1177/0278364904045593>
- Sugeno, M., & Takagi, T. (1983). Multi-dimensional fuzzy reasoning. *Fuzzy Sets and Systems*, 9(1–3), 313–325.
- Sukkarieh, S. (2000). Low Cost high integrity aided inertial navigation systems for autonomous land vehicles. The University of Sydney.
- Tardif, J. P., George, M., Laverne, M., Kelly, A., & Stentz, A. (2010). A new approach to vision-aided inertial navigation. In *IEEE/RSJ 2010 International Conference on Intelligent Robots and Systems, IROS 2010 - Conference Proceedings* (pp. 4161–4168). IEEE.
<https://doi.org/10.1109/IROS.2010.5651059>
- Teunissen, P. J. G. (1995). The least-squares ambiguity decorrelation adjustment: a method for fast GPS integer ambiguity estimation. *Journal of Geodesy*, 70(1–2), 65–82.
<https://doi.org/10.1007/BF00863419>
- Teunissen, P. J. G. (1997). On the sensitivity of the location, size and shape of the GPS ambiguity search space to certain changes in the stochastic model. *Journal of Geodesy*, 71(9), 541–551. <https://doi.org/10.1007/s001900050122>
- Tomasi, C., & Kanade, T. (1991). Detection and tracking of point features.
- Tomasi, C., & Kanade, T. (1993). Shape and motion from image streams: a factorization method. *Proceedings of the National Academy of Sciences*, 90(21), 9795–9802.
<https://doi.org/10.1073/pnas.90.21.9795>
- Ullman, S. (1979). The Interpretation of Structure from Motion. *Proceedings of the Royal Society of London. Series B. Biological Sciences*, 203(1153), 405 LP-426.
<https://doi.org/10.1098/rspb.1979.0006>
- Usenko, V., Engel, J., & Cremers, D. (2016). Direct Visual-Inertial Odometry with Stereo Cameras. In *2016 IEEE International Conference on Robotics and Automation* (pp. 1885–1892).
- Van Broekhoven, E., & De Baets, B. (2008). Monotone Mamdani-Assilian models under mean

- of maxima defuzzification. *Fuzzy Sets and Systems*, 159(21), 2819–2844.
<https://doi.org/10.1016/j.fss.2008.03.014>
- Veth, M., & Raquet, J. (2006). *Two-Dimensional Stochastic Projections for Tight Integration of Optical and Inertial Sensors for Navigation*. *National Technical Meeting Proceedings of the Institute of Navigation*. DTIC Document.
- Wang, J.-G., Qian, K., & Hu, B. (2015). An Unconventional Full Tightly-Coupled Multi-Sensor Integration for Kinematic Positioning and Navigation. In *China Satellite Navigation Conference (CSNC) 2015 Proceedings: Volume III* (pp. 753–765). Springer.
- Wang, M. (2008). A Controlled Experiment of Real-Time Precise Point Positioning for Deformation Monitoring. In *Proceedings of the 2008 National Technical Meeting of The Institute of Navigation* (pp. 28–30).
- Wang, M. (2014). *Ambiguity Resolution with Precise Point Positioning*. University of Calgary.
- WG, M. (1985). The case for ranging in GPS-based geodetic systems. In *Proceedings first international symposium on precise positioning with the global positioning system* (Vol. 1519, pp. 373–386).
- Wu, J. T., Wu, S. C., Hajj, G. A., Bertiger, W. I., & Lichten, S. M. (1992). Effects of antenna orientation on GPS carrier phase. In *Advances in the Astronautical Sciences* (Vol. 76, pp. 1647–1660). <https://doi.org/19920060722>
- Wübbena, G. (1985). Software developments for geodetic positioning with GPS using TI 4100 code and carrier measurements. In *Proceedings of First International Symposium on Precise Position with GPS, Rockville, Maryland* (Vol. 19, pp. 403–412). Retrieved from <http://scholar.google.com/scholar?hl=en&btnG=Search&q=intitle:Software+developments+for+geodetic+positioning+with+GPS+using+TI+4100+code+and+carrier+measurements#0>
- Xian, Z., Hu, X., & Lian, J. (2015). Fusing Stereo Camera and Low-Cost Inertial Measurement Unit for Autonomous Navigation in a Tightly-Coupled Approach. *Journal of Navigation*, 68(3), 434–452.
- Xu, G. (2003). *Gps: Theory, Algorithms and Applications*. Springer. Retrieved from <http://books.google.com/books?id=aRKPAXBt174C&pgis=1>
- Zhang, Z. (2000). A flexible new technique for camera calibration. *IEEE Transactions on*

Pattern Analysis and Machine Intelligence, 22(11), 1330–1334.

Zumberge, J. F., Heflin, M. B., Jefferson, D. C., Watkins, M. M., & Webb, F. H. (1997). Precise point positioning for the efficient and robust analysis of GPS data from large networks.

Journal of Geophysical Research: Solid Earth, 102(B3), 5005–5017.

<https://doi.org/10.1029/96JB03860>

Appendix A

The dynamic matrix of INS error propogation:

$$F^l = \begin{bmatrix} F_{rr} & F_{rV} & 0_{3 \times 3} & 0_{3 \times 3} & 0_{3 \times 3} \\ F_{Vr} & F_{VV} & F_{V\varepsilon} & R_b^l & 0_{3 \times 3} \\ F_{\varepsilon r} & F_{\varepsilon V} & F_{\varepsilon\varepsilon} & 0_{3 \times 3} & R_b^l \\ 0_{3 \times 3} & 0_{3 \times 3} & 0_{3 \times 3} & -\alpha & 0_{3 \times 3} \\ 0_{3 \times 3} & 0_{3 \times 3} & 0_{3 \times 3} & 0_{3 \times 3} & -\beta \end{bmatrix}$$

$$F_{rr} = \begin{bmatrix} 0 & 0 & \frac{-v_n}{(R_m + R_n)^2} \\ \frac{v_e \tan \varphi}{(R_n + h) \cos \varphi} & 0 & \frac{-v_e}{(R_n + h)^2 \cos \varphi} \\ 0 & 0 & 0 \end{bmatrix}$$

$$F_{rV} = \begin{bmatrix} 0 & 0 & \frac{-v_n}{(R_m + h)^2} \\ \frac{v_e \tan \varphi}{(R_n + h) \cos \varphi} & 0 & \frac{-v_e}{(R_n + h)^2 \cos \varphi} \\ 0 & 0 & 0 \end{bmatrix}$$

$$F_{Vr} = \begin{bmatrix} 2\omega_e(v_u \sin \varphi + v_n \cos \varphi) + \frac{v_n v_e}{(R_n + h) \cos^2 \varphi} & 0 & 0 \\ -2\omega_e v_e \cos \varphi - \frac{v_e^2}{(R_n + h) \cos^2 \varphi} & 0 & 0 \\ -2\omega_e v_e \sin \varphi & 0 & \frac{2g}{R} \end{bmatrix}$$

$$F_{VV} = \begin{bmatrix} \frac{-v_u}{(R_n + h)} + \frac{v_n \tan \varphi}{(R_n + h)} & (2\omega_e + \dot{\lambda}) \sin \varphi & -(2\omega_e + \dot{\lambda}) \cos \varphi \\ -\dot{\lambda} \sin \varphi - (2\omega_e + \dot{\lambda}) \sin \varphi & \frac{-v_u}{(R_m + h)} & -\frac{v_n}{(R_m + h)} \\ \dot{\lambda} \cos \varphi + (2\omega_e + \dot{\lambda}) \cos \varphi & \frac{2v_n}{(R_m + h)} & 0 \end{bmatrix}$$

$$F_{V\varepsilon} = \begin{bmatrix} 0 & f_u & -f_n \\ -f_u & 0 & f_e \\ f_n & -f_e & 0 \end{bmatrix}$$

$$F_{\varepsilon r} = \begin{bmatrix} 0 & 0 & -\frac{\dot{\varphi}}{R_m + h} \\ \omega_e \sin \varphi & 0 & -\frac{\dot{\lambda} \cos \varphi}{R_n + h} \\ -\omega_e \cos \varphi + \frac{\dot{\lambda}}{\cos \varphi} & 0 & -\frac{\dot{\lambda} \sin \varphi}{R_n + h} \end{bmatrix}$$

$$F_{\varepsilon V} = \begin{bmatrix} 0 & \frac{1}{R_m + h} & 0 \\ \frac{1}{R_n + h} & 0 & 0 \\ \frac{-\tan \varphi}{R_n + h} & 0 & 0 \end{bmatrix}$$

$$F_{\varepsilon\varepsilon} = \begin{bmatrix} 0 & (\omega_e + \dot{\lambda}) \sin \varphi & -(\omega_e + \dot{\lambda}) \cos \varphi \\ -(\omega_e + \dot{\lambda}) \sin \varphi & 0 & -\dot{\varphi} \\ (\omega_e + \dot{\lambda}) \cos \varphi & \dot{\varphi} & 0 \end{bmatrix}$$

where $\dot{\lambda} = \frac{v_e}{(R_n + h) \cos \varphi}$, $\dot{\varphi} = \frac{v_n}{(R_m + h)}$; ω_e is the earth rotation angular rate; α and β are the

reciprocal of the correlation time of accelerometers and gyros respectively.

In discrete-time system, the covariance matrix of the process noise can be formed as

$$\begin{aligned}
Q_{k-1} &= \frac{\Delta t}{1!} M_1 + \frac{\Delta t^2}{2!} M_2 + \frac{\Delta t^3}{3!} M_3 + \dots \\
M_1 &= \bar{Q} \\
M_2 &= \bar{Q} F^T + F \bar{Q} \\
M_3 &= \bar{Q} (FF)^T + FF \bar{Q} + 2F \bar{Q} F^T \\
&\vdots \\
\bar{Q} &= GqG^T \\
G &= \begin{bmatrix} 0_{3 \times 3} & 0_{3 \times 3} & 0_{3 \times 3} & 0_{3 \times 3} \\ R_b^l & 0_{3 \times 3} & 0_{3 \times 3} & 0_{3 \times 3} \\ 0_{3 \times 3} & R_b^l & 0_{3 \times 3} & 0_{3 \times 3} \\ 0_{3 \times 3} & 0_{3 \times 3} & \sqrt{2\alpha\sigma_f^2} & 0_{3 \times 3} \\ 0_{3 \times 3} & 0_{3 \times 3} & 0_{3 \times 3} & \sqrt{2\beta\sigma_\omega^2} \end{bmatrix}
\end{aligned}$$

where F is the dynamic matrix; Q_{k-1} is the covariance matrix of the process noise in Eq (3.1); σ_f^2 and σ_ω^2 are the variance of the white noise in first-order Gaussian-Markov model for accelerometer and gyro biases respectively; q is the power spectral density (PSD) of the white noise w as follows

$$w = [w_{ar} \quad w_{ab} \quad w_{gr} \quad w_{gb}]^T$$

where w_{ar} , w_{gr} are the white noise for velocity random walk and angular random walk; w_{ab} , w_{gb} are the white noise in first-order Gaussian-Markov model for accelerometer and gyro biases with Gaussian distribution $N(0, 1)$.